



A University of Sussex DPhil thesis

Available online via Sussex Research Online:

<http://sro.sussex.ac.uk/>

This thesis is protected by copyright which belongs to the author.

This thesis cannot be reproduced or quoted extensively from without first obtaining permission in writing from the Author

The content must not be changed in any way or sold commercially in any format or medium without the formal permission of the Author

When referring to this work, full bibliographic details including the author, title, awarding institution and date of the thesis must be given

Please visit Sussex Research Online for more information and further details

Electronic Structure and Mechanistic Studies of non-traditional Ziegler-Natta Catalysts

Kayla M. Keller

Submitted for the degree of Doctor of Philosophy
University of Sussex
January 2012

Declaration

I hereby declare that this thesis has not been and will not be submitted in whole or in part to another University for the award of any other degree.

Signature:

Kayla M. Keller

UNIVERSITY OF SUSSEX

KAYLA M. KELLER, DOCTOR OF PHILOSOPHY

ELECTRONIC STRUCTURE AND MECHANISTIC STUDIES OF NON-TRADITIONAL ZIEGLER-NATTA CATALYSTS

ABSTRACT

This thesis focuses on the structure and reactivity of a variety of inorganic systems through the exploration of their electronic structure by employing density functional theoretical methods. Chapter 1, the introduction, outlines the theoretical approaches and includes a historical overview of the development of quantum theory. The theoretical methods and their applications are then described and discussed. The first chapter concludes with an overview of the work undertaken.

Chapter 2 presents a historical background of the experimental and theoretical work done on traditional Group IV Ziegler-Natta catalysis including the generally accepted mechanisms believed to be employed when these systems are used to polymerise olefins. Furthermore, a description of the experimental results obtained when a non-traditional Ziegler-Natta catalyst was subjected to propylene are given as a rationale for the calculations presented in Chapter 3.

Chapter 3 presents a theoretical exploration of a novel class of olefin polymerization catalysts based on the *tris*(amido)titanium(IV) platform. Here, DFT has been used to probe the electronic structure of these compounds in order to provide a rationale for the catalytic activity that is associated with them as well as a possible new mechanism for this type of non-traditional catalyst. Furthermore, Chapter 4 takes a closer look at a large number of potential intermediates that are available for the polymerization reaction discussed in Chapter 3.

In Chapter 5, a series of simple transition metal complexes are calculated and analysed to further understand key aspects of the system. The complexes represent a basic model of the novel catalysts found in Chapter 3 and contain the essential feature of π -acid-base chemistry within the coordination sphere.

Acknowledgements

First and foremost, I would like to thank my supervisor, Dr John Turner. Thank you, not only for giving me the amazing opportunity of living in England, but also for your endless support, encouragement and occasional kick in the pants when I needed it most. Thank you for not giving up on me and for always finding a way to make things work, especially the times when I wasn't convinced it was possible. I am truly grateful to be able to call you not only my boss, but also my friend.

Thank you to all Turner group members both past and present and in particular, Tara and Laura. Thank you for being a shoulder to cry on and always willing to listen. You ladies are amazing and I couldn't have done it without you.

I would also like to thank all of those in offices 3R513-3R514 and Ar218 during my time there and all of the friends I have made here at Sussex and those in America. Special thanks to Caroline, Jens and Gemma for helping me find my feet and to Lewis, Noel and Jason, as well as Dr. Eddy Viseux, for answering my, sometimes endless, Organic questions. To Mat for the Hippos, Stefanie for the papers and to Abby, Alicia and Professors Dahl and Pesterfield for always believing in me and pushing me to do my best, I am ever thankful. Also to the many others, whom I'm sure, I have left out.

Thank you to my parents and sisters not only for their support and for believing in me but also for instilling the belief that I can achieve anything if I just put my mind to it. Thank you to the Marchant family for not only taking me into their home but also for truly treating me like part of the family; I am forever indebted to your hospitality.

Lastly, I would like to thank my loving husband, Joe, and son, Jacob. Joe, thank you for giving up a job you loved to move to England, for always doing whatever had to be done and for never once doubting my ability. There is no doubt in my mind that without you I couldn't have made it to where I am today. Jacob, watching you grow has been absolutely amazing; I believe you're the person who has been the most brave through this. I love you both.

For Will, a man of vision and determination.

Thank you for giving me the family that has shaped me into the person I am today.

May you rest in eternal peace.

Whatever you are, be a good one.

-Abraham Lincoln

Contents

List of Tables	ix
List of Figures	xiv
1 Introduction	1
1.1 Theoretical Approaches to Molecular Structure	1
1.1.1 Historical Background	1
1.2 The quantum mechanical atom	6
1.2.1 The Schrödinger equation	7
1.2.2 Many body systems	8
1.3 Modern Computational Approaches	10
1.3.1 Hartree Fock Theory	12
1.3.2 Møller-Plesset Perturbation Theory	13
1.3.3 Configurational interaction	14
1.3.4 Density Functional Theory	15
1.3.5 Basis sets	20
1.4 Overview of work	23
2 Mechanism and scope of alkene polymerization at Group (IV) metal centres	25
2.1 History of experimental Ziegler-Natta catalysis	25
2.1.1 Early beginnings - The Aufbau Reaction	25
2.1.2 A Serendipitous Experiment	26
2.1.3 Homogeneous Ziegler-Natta	28
2.2 Experimental Mechanism	29
2.2.1 Cossée-ArIman Mechanism	29

2.2.2	Green-Rooney Mechanism	30
2.3	Computational Approaches	30
2.3.1	Ziegler-Natta polymerization	30
2.4	Rationale for study	39
3	Examination of a new mechanism for alkene polymerization at <i>tris</i>(amido)titanium centres	42
3.1	Introduction	42
3.2	Computational Detail	42
3.3	Structure and reactivity of [(dpa) ₃ Ti] ⁺ (1)	43
3.3.1	Structure	43
3.3.2	Analogous species	44
3.3.3	Electronic structure	47
3.3.4	Reactivity	48
3.4	Structure of the [(dpa) ₃ Ti–C ₃ H ₆] ⁺ adduct, (2)	49
3.5	Intermediate complex	53
3.5.1	Structure of [(dpa) ₃ Ti–C ₆ H ₁₂] ⁺ (3)	55
3.6	Structure of [(dpa) ₂ Ti(C ₆ H ₁₂ N(C ₆ H ₅) ₂)–C ₃ H ₆] ⁺ (4)	57
3.7	Chain Termination	59
3.8	Structure of (dpa) ₃ TiCH ₃ (5)	59
3.8.1	Analogous system: (dsa) ₃ TiCH ₃	60
3.9	Structure of (dpa) ₃ Ti–CH ₃ –B(C ₆ F ₅) ₃ (6)	61
3.10	Conclusions	63
4	The hetero-metallocyclo intermediate	66
4.1	Introduction	66
4.1.1	Labelling scheme	67
4.2	Possible pathways involving pseudo-4 + 2 cycloaddition	68
4.2.1	Pathway A	71
4.2.2	Pathway B	74
4.2.3	Summary of intermediates involving six-membered rings	77

4.3	Pathways involving five-membered rings	78
4.3.1	Pathway C	80
4.3.2	Pathway D	84
4.3.3	Summary of intermediates involving five-membered rings	87
4.4	Pathways involving geometry rearrangement at the metal centre	88
4.4.1	Pathway E	89
4.4.2	Pathway F	90
4.5	Conclusions	90
5	Generalizations of Trigonal Group IV Metal Centres	92
5.1	Introduction	92
5.2	Importance of amido transition metal complexes	92
5.2.1	Notable compounds	93
5.2.2	Group theoretical analysis	95
5.2.3	Computational results	101
5.3	Experimental	103
5.3.1	Computational Methods	104
5.3.2	$[(dma)_3Ti]^+$ (7)	104
5.3.3	$(dma)_3TiH$ (8)	106
5.3.4	$(dma)_3TiF$ (9)	107
5.3.5	Trends	107
5.4	Conclusions	110
6	Conclusions and Suggestions for Future Work	111
6.1	Conclusions	111
6.2	Suggestions for Further Work	113
	Appendices	127
.1	Projection operators	127
.2	Normalization of SALCs	128
.3	Normalization of molecular wave functions	131

.4	Normalization including ligand-ligand overlap	132
.5	Group overlap of metal and ligand orbitals	133

List of Tables

3.1	Averaged bond lengths /Å and angles /° of (dpa) ₄ Ti and [(dpa) ₃ Ti] ⁺ , 1	45
3.2	Orbital composition (%) of [(dpa) ₃ Ti] ⁺	47
3.3	Relevant bond lengths (Å) and angles (°) of C ₃ H ₆ with absolute difference from experiment	49
3.4	Orbital composition (%) of [(dpa) ₃ Ti–C ₃ H ₆] ⁺	50
3.5	Bond distances (Å) and angles (°) of 3 and 4	58
3.6	Orbital composition (%) of (dpa) ₃ TiCH ₃	60
3.7	Average bond lengths (Å) and angles (°) of (dsa) ₃ TiCH ₃ and (dpa) ₃ TiCH ₃	61
3.8	Structural data for Cp ₂ Zr(CH ₃)–CH ₃ –B(C ₆ F ₅) ₃ derivatives and calculated 6	62
4.1	Relevant structural data for A-RR and A-SR	72
4.2	Relevant structural data for B-RR and B-SR	75
4.3	Torsional distortions in C₃-4_{uS}-5_{uS}	80
4.4	Relative Energy (/kJ mol ⁻¹) of Pathway C , five-membered ring intermediates with respect to the lowest energy six-membered intermediate	87
4.5	Relative Energy (/kJ mol ⁻¹) of Pathway D , five-membered ring intermediates with respect to the lowest energy six-membered intermediate	88
5.1	CBC classifications for [(R ₂ N) ₃ M] ⁺ , (R ₂ N) ₃ MH and (R ₂ N) ₃ MF	96
5.2	Irreducible representations for the metal-centred orbitals	97
5.3	Group table for C ₃ together with Γ(<i>p</i>) and the projection operator for the C <i>p_z</i> orbital	98
5.4	Selected structural data for complexes 7 , 8 and 9	108
5.5	Calculated Mulliken atomic charges / e 	110

List of Figures

1.1 Planck spectra at $T = 5000, 4000$ and 3000 K along with the classical or Rayleigh-Jeans spectrum for a black body	3
2.1 The Aufbau reaction	26
2.2 α -TiCl ₃	27
2.3 Examples of tacticity in polypropylene	27
2.4 Cossée or Cossée-Arlman Mechanism	30
2.5 Modified Green-Rooney Mechanism	31
2.6 Reduction in symmetry from D_{5h} to C_{2v} , adapted from [70]	32
2.7 Illustration of α , the angle between the planes created by the cyclopentadienyl rings, adapted from [70]	32
2.8 Kaminsky catalysts studied by Ziegler <i>et al.</i> ^[75]	33
2.9 Illustration of the methyl tilt angle, θ , the angle between the M–C vector, shown in blue, and the local C_3 axis of the methyl group, shown in red.	34
2.10 Front and Back Side insertion precursors ^[76]	34
2.11 Front and Back Side transition states ^[76]	35
2.12 Cationic catalyst species studied by Ziegler and co-workers ^[94]	35
2.13 Anionic co-catalyst species studied by Ziegler and co-workers. ^[94]	36
2.14 Mechanism for complexation and insertion in the presence of the counterion. ^[94]	37
2.15 Energetic landscape of the insertion of propylene into [(Cp)(NCR ₂)TiCH ₃] ⁺ [H ₃ CB(C ₆ F ₅) ₃] [–] ^[94]	38
2.16 (a) $\ln P$ vs. t for the reaction [Ti(dpa) ₃] ⁺ [B(C ₆ F ₅) ₄] [–] + C ₃ H ₆ and (b) Fit to a first order exponential	41
3.1 Calculated structure of [(dpa) ₃ Ti] ⁺ , 1	44

3.2 (a) Bisection of the trigonal plane about the nitrogen atom and (b) torsional angles in dpa_4Ti and 1	46
3.3 $((\text{C}_6\text{H}_5)\text{CH}_2)_4\text{Ti}$	47
3.4 $[(\text{dpa})_3\text{Ti}]^+$ HOMO and LUMO	47
3.5 (a) Potential energy surface of the reaction coordinate $\text{Ti}-\text{N}-\text{C}$, θ and (b) pictorial description of the $\text{Ti}-\text{N}-\text{C}$ angle, θ	48
3.6 $[(\text{dpa})_3\text{Ti}-\text{C}_3\text{H}_6]^+$ HOMO and LUMO	50
3.7 $[(\text{dpa})_3\text{Ti}-\text{C}_3\text{H}_6]^+$ HOMO -15	50
3.8 Molecular Orbital diagram for the formation of $[(\text{dpa})_3\text{Ti}-\text{C}_3\text{H}_6]^+$ from the reaction of 1 and propylene	51
3.9 Asymmetric binding in calculated α -olefin complexes. ^[75,108]	53
3.10 Facial addition	53
3.11 Illustration of the $[(\text{dpa})_2\text{Ti}-\text{C}_2\text{H}_3(\text{CH}_3)\text{C}_2\text{H}_3(\text{CH}_3)\text{dpa}]^+$ species.	54
3.12 Reaction forming the $[(\text{dpa})_2\text{Ti}-\text{C}_2\text{H}_3(\text{CH}_3)\text{C}_2\text{H}_3(\text{CH}_3)\text{dpa}]^+$ species.	54
3.13 Possible directions of approach for the incoming olefin viewed from the side, left, and down the $\text{C}-\text{Ti}$ vector, right.	55
3.14 Schematic of the lowest energy isomer for the intermediate 3	55
3.15 $[(\text{dpa})_3\text{Ti}-\text{C}_6\text{H}_{12}]^+$ HOMO and LUMO	56
3.16 $[(\text{dpa})_2\text{Ti}(\text{C}_6\text{H}_{12}\text{N}(\text{C}_6\text{H}_5)_2)-\text{C}_3\text{H}_6]^+$ 4	57
3.17 $[(\text{dpa})_2\text{Ti}(\text{C}_6\text{H}_{12}\text{N}(\text{C}_6\text{H}_5)_2)-\text{C}_3\text{H}_6]^+$ HOMO and LUMO	57
3.18 Weak α -agostic interaction of 4 , HOMO-7	58
3.19 $\text{Ti}-\alpha\text{C}_{\text{C}_3\text{H}_6}$ interaction in 4 , HOMO -21	59
3.20 $(\text{dpa})_3\text{TiCH}_3$ HOMO and LUMO	60
3.21 $(\text{dpa})_3\text{TiCH}_3$ HOMO-3	61
3.22 $(\text{dpa})_3\text{TiCH}_3-\text{CH}_3-\text{B}(\text{C}_6\text{F}_5)_3$, 6	62
3.23 Known crystal structures of $\text{Cp}_2\text{Zr}(\text{CH}_3)-\text{CH}_3-\text{B}(\text{C}_6\text{F}_5)_3$ and its derivatives	62
3.24 $(\text{dpa})_3\text{Ti}-\text{CH}_3-\text{B}(\text{C}_6\text{F}_5)_3$ HOMO-21	63
3.25 Expected mechanism for the polymerisation of propylene at 1	64
4.1 The Ivanov reaction	66

4.2 Possible directions of approach for the incoming olefin viewed from the side, left, and down the C–Ti vector, right.	67
4.3 pseudo-4 + 2 cycloaddition	69
4.4 Enantiomeric structures of the A-RR/SS sets	69
4.5 Axial vs. equatorial position	70
4.6 Pathway A	71
4.7 Possible chair conformations of A-RR and A-SR	71
4.8 Pathway for the formation of A-RR	72
4.9 Equilibrium of the two chair conformations of A-RR	72
4.10 Pathway for the formation of A-SR	73
4.11 Equilibrium of the two chair conformations of A-SR	73
4.12 Qualitative potential energy surface for the interconversion between two chair con- formations	74
4.13 Pathway B	75
4.14 Possible chair conformations of B-RR and B-SR	75
4.15 Pathway for the formation of B-RR	75
4.16 Equilibrium of the two chair conformations in B-RR	76
4.17 Pathway for the formation of B-SR	76
4.18 Equilibrium of the two chair conformations in B-SR	77
4.19 Relative energy for six-membered rings	78
4.20 pseudo 3 + 2 cycloaddition	78
4.21 Possible conformations of five-membered rings	79
4.22 Enantiomeric examples of the envelope conformations of the apex-up C-SS and apex-down C-RR	79
4.23 Pathway C	80
4.24 Pathway for the formation of C-SS	81
4.25 Possible envelope conformations of C-SS	81
4.26 Pathway for the formation of C-RS	82
4.27 Possible envelope conformations of C-RS	82

4.28 Pathway for the formation of C-RR	82
4.29 Possible envelope conformations of C-RR	83
4.30 Pathway for the formation of C-SR	83
4.31 Possible envelope conformations of C-SR	83
4.32 Pathway D	84
4.33 Pathway for the formation of D-SS	84
4.34 Possible envelope conformations of D-SS	85
4.35 Pathway for the formation of D-RS	85
4.36 Possible envelope conformations of D-RS	85
4.37 Pathway for the formation of D-RR	86
4.38 Possible envelope conformations of D-RR	86
4.39 Pathway for the formation of D-SR	86
4.40 Possible envelope conformations of D-SR	87
4.41 Pathway E	89
4.42 Pathway F	90
4.43 Lowest energy conformers and relative energies /kJ mol ⁻¹	91
5.1 Reaction of Mo complex with a 'two-sided' ligand set with N ₂ ^[133] and N ₂ O ^[134] . . .	94
5.2 Gas ^[163] vs. solid ^[164] phase Zr(NMe ₂) ₄ illustrating the terminal and bridging bonding motifs in the amido ligand.	94
5.3 Bonding motifs of the di-alkylamido ligand	95
5.4 ((CH ₃) ₂ N) ₃ Zr[μ-N(H)B ₃ (CH ₃) ₂ N ₃ (CH ₃) ₃] ₂ ^[165]	96
5.5 Ligand bases for the (R ₂ N) ₃ M fragment	97
5.6 Calculated SALCs for the radial, ϕ_X , and tangential, ϕ_L , functions in <i>C</i> ₃	100
5.7 Overlap	101
5.8 Calculated structure of [(dma) ₃ Ti] ⁺ , 7	105
5.9 (dma) ₃ Ti ⁺ in <i>C</i> ₃ symmetry	105
5.10 Calculated structure of (dma) ₃ TiH, 8	106
5.11 (dma) ₃ TiH in <i>C</i> ₃ symmetry	106
5.12 Calculated structure of (dma) ₃ TiF, 9	107

5.13 (dma) ₃ TiF in C_3 symmetry	108
5.14 Molecular Orbital diagram for (dma) ₃ TiX where X = +, H, F	109
5.15 Change in the calculated Mulliken atomic charge for (dma) ₃ TiX where X = +, H, F	110
6.1 Expected mechanism for the polymerisation of propylene at 1	112

List of Symbols and Constants

k_B	Boltzmann's constant	$1.380658 \times 10^{-23} \text{ J K}^{-1}$
T	Temperature	
λ	wavelength	
h	Planck's constant	$6.626075 \times 10^{-34} \text{ J s}$
v	velocity	
c	speed of light	$2.99792458 \times 10^8 \text{ m s}^{-1}$
m_e	mass of electron	$9.10938 \times 10^{-31} \text{ kg}$
Φ	work function	
ν	frequency	
R_H	Rydberg's constant	$109,737.31568549(83) \text{ cm}^{-1}$
V_C	Coulombic potential	
Z	Atomic number	
e	Charge on an electron	$1.602176 \times 10^{-19} \text{ C}$
ϵ_0	Permittivity of a vacuum	
r	radius	
F_C	centripetal force	

Chapter 1

Introduction

1.1 Theoretical Approaches to Molecular Structure

1.1.1 Historical Background

By the end of the 19th century, classical or Newtonian Physics was a well established field of study with only a few 'problems' left to solve. Max Planck described being discouraged from studying physics in a lecture given in 1924:

When I began my physical studies [in Munich in 1874] and sought advice from my venerable teacher Philipp von Jolly...he portrayed to me physics as a highly developed, almost fully matured science...Possibly in one or another nook there would perhaps be a dust particle or a small bubble to be examined and classified, but the system as a whole stood there fairly secured, and theoretical physics approached visibly that degree of perfection which, for example, geometry has had already for centuries.^[1]

Failures of classical physics

One subject that classical physics had failed to explain was the distribution of radiation given off by a black body. A black body is an object that absorbs all electromagnetic radiation to which it is exposed; it is also a perfect emitter.^[2-4]

Several attempts were made in order to elucidate the solution. One of the earliest attempts was in the 1890's by Wien, whose results were in agreement with the spectrum at short wavelengths

but failed when longer wavelengths were considered. Later, Lord Rayleigh, in collaboration with James Jean, used theoretical arguments to describe the electromagnetic field as oscillators of unconfined frequency, where frequency, ν , and wavelength, λ , are equated by the equation

$$\lambda = \frac{c}{\nu} \quad (1.1.1)$$

where c is the speed of light with a value of $2.99792458 \times 10^8 \text{ m s}^{-1}$. By the use of the Boltzmann distributions over energy levels of three-dimensional harmonic oscillators, which were assumed to be continuous, the Rayleigh-Jeans law^[5] was derived:

$$dE = \frac{8\pi k_B T}{\lambda^4} d\lambda \quad (1.1.2)$$

where k_B is the Boltzmann constant. However, while giving good results at long wavelengths, the Rayleigh-Jeans law fails at short wavelengths and actually predicts that at short wavelengths, such as in the ultraviolet region, the intensity diverges since as $\lambda \rightarrow 0$, intensity $\rightarrow \infty$. This is referred to as the *ultraviolet catastrophe*.^[2,4]

In 1900 Max Planck also used oscillators and the Boltzmann distribution over the density of states to develop his theory, although he made the fundamentally simple assumption that the oscillators could only have discrete frequency values, therefore limiting or 'quantizing' the energy via

$$E = nh\nu \quad (1.1.3)$$

where n is an integer value. Through his assumption, Planck was able to derive a new equation:

$$dE = \frac{8\pi hc}{\lambda^5 \left(e^{\frac{hc}{\lambda kT}} - 1 \right)} d\lambda \quad (1.1.4)$$

where h was, at the time a yet undetermined proportionality constant first shown in equation (1.1.3), and is now known as Planck's constant with the value of $6.626 \times 10^{-34} \text{ J s}$. This new function, known as the Planck distribution, gives an excellent fit to the experimental data.^[2-4] A

graph of Planck's distribution along with the Rayleigh-Jeans spectrum are shown in Figure 1.1.

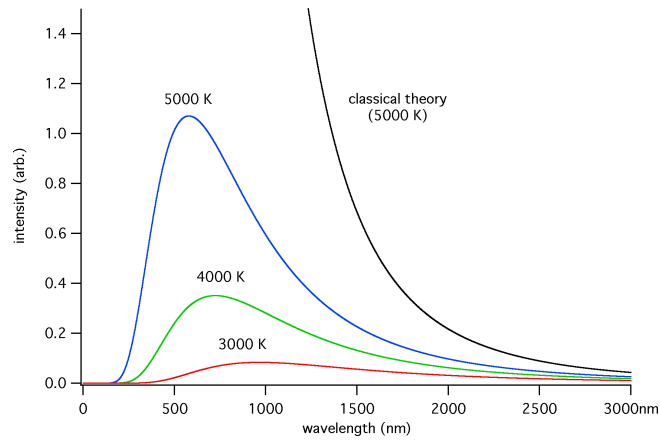


Figure 1.1: Planck spectra at $T = 5000, 4000$ and 3000 K along with the classical or Rayleigh-Jeans spectrum for a black body

The photoelectric effect also defied classical explanation. The photoelectric effect is the observation that when a light beam of a particular frequency is directed onto a clean metal surface, an electric current could be measured as electrons were ejected from the metal. Several other observations were also noted as the frequency of the incident light was altered. These included:

- (i) A minimum frequency is necessary in order for the electrons to be ejected; this frequency is referred to as the 'threshold frequency,' ν_0 .
- (ii) The 'threshold frequency' differs with the type of metal employed.
- (iii) The kinetic energy of the ejected electrons is proportional to the frequency of the incident light, not the intensity.
- (iv) The number of electrons that are ejected is dependent on the intensity of the incident light beam.

In 1905, Albert Einstein provided an explanation to the above observations by describing light as a particle, where each 'quantum' or 'photon' of light has energy of $E = h\nu$. When a photon strikes the surface of the metal, an electron is ejected, provided that the frequency of light used is larger than the 'threshold frequency' needed for the given metal. The kinetic energy of the now ejected electron is described by:

$$\frac{1}{2}m_e v^2 = h\nu - \Phi \quad (1.1.5)$$

where Φ is a work function needed in order to eject the electron, the amount of energy required to remove the electron.^[2-4,6]

Structure and stability of the atom

The inability to explain the discrete nature of the emission spectrum of gases such as atomic hydrogen is a third failure of classical physics. Although unable to explain it, scientists used the fact that each element gave a unique and discrete spectrum in order to assign compositions to unknown samples through comparison to known spectra.^[3,6,7]

In 1885, Johann Balmer, a Swiss mathematician, derived an empirical formula that accurately described the four emission lines in the visible spectrum of hydrogen as well as predicting a fifth line in the ultraviolet region. This formula is:

$$\lambda = 3.6456 \times 10^{-11} \left(\frac{n^2}{n^2 - 2^2} \right) \quad (1.1.6)$$

where λ is the wavelength of the emitted line in centimetres, 3.6456×10^{-11} is a constant with the units of centimetres and n is an integer value larger than 2.^[3]

Johannes Rydberg, a Swedish mathematician and physicist, was also working on spectral lines. He found that for each element the lines could be divided into series. In 1889, apparently unaware of Balmer's findings, he published his first paper on the subject stating that:

"In all spectra which have been investigated so far, the strongest lines form series, and these can be approximated by means of the formula

$$n = n_0 - \frac{N_0}{(m + \mu)^2} \quad (1.1.7)$$

where n is the wavenumber of the line, N_0 a constant with the value of 109,721.6 $[cm^{-1}]$ while n_0 , m and μ are constants which are specific for the series."

He later made the realization that Balmer's findings were a special case of his work.^[7]

Equation (1.1.7) can be rearranged, with some substitutions, to the more familiar form of

$$\frac{1}{\lambda} = R_H \left(\frac{1}{n_f^2} - \frac{1}{n_i^2} \right). \quad (1.1.8)$$

R_H is the Rydberg constant. The current value is $109,737.3157 \text{ cm}^{-1}$.^[8] n_f and n_i are integers that label the initial and final energy levels, where $n_i > n_f$ for emission.^[6] Unfortunately, although armed with a formula that described the spectral lines, Rydberg's formula was purely based on empirical observation, with no theoretical basis. The first partially successful attempt at a more theoretically based description came in 1913 from the Danish physicist Niels Bohr.

The general make-up of the atom had been established by the beginning of the 20th century. Joseph John Thompson had discovered the electron in 1897^[9] and in 1911 Ernest Rutherford^[10] made the discovery that the atom contained a very small positive nucleus in the centre that was surrounded by a large negative volume where the electron(s) could be found.^[3,6] In 1913 Niels Bohr^[11] published his model of the atom. Bohr's starting point was the assumption that the electrons were moving in circular orbits around the nucleus. The Coulombic potential, V_C , the potential that describes the attraction of the electron to the positive nucleus, has the form:

$$V_C = -\frac{Ze^2}{4\pi\epsilon_0 r^2} \quad (1.1.9)$$

where Z is the atomic number, e is the charge on the electron, ϵ_0 is the permittivity of a vacuum and r is the radius of the electron's orbit. The Coulombic force was then balanced by the centripetal force of the form:

$$F_C = \frac{m_e v^2}{r} \quad (1.1.10)$$

where m_e is the mass of the electron and v is its instantaneous velocity. When these two forces are equated, as the electron neither spirals into the nucleus nor flies out of the atom, the following equation is found:

$$\frac{Ze^2}{4\pi\epsilon_0 r} = m_e v^2 \quad (1.1.11)$$

The total energy of an electron consists of the sum of the kinetic and potential energy.

$$E = \frac{1}{2}m_e v^2 - \frac{Ze^2}{4\pi\epsilon_0 r} \quad (1.1.12)$$

Bohr made an extremely important assumption based on Planck's work. He only allowed the electrons to occupy particular orbits by quantizing the angular momentum.

$$m_e v r = n \frac{h}{2\pi} \quad (1.1.13)$$

where n must be an integer value, now known as the principle quantum number. If equation (1.1.13) is solved for m_e and substituted into equation (1.1.11) which is subsequently solved for v , the total energy of the electron can be found as a function of n and is given by

$$E_n = -\frac{m_e Z^2 e^4}{8h^2 \epsilon_0^2} \cdot \frac{1}{n^2} \quad (1.1.14)$$

Likewise, employing equations (1.1.11) and (1.1.13) and solving for r gives the radius of the orbit as a function of n

$$r_n = \frac{n^2 h^2 \epsilon_0}{Z \pi m_e e^2} \quad (1.1.15)$$

the value of r_1 is 0.529 Å and is known as the Bohr radius in hydrogen. When equation (1.1.14) is used to find the difference in energy between two states, the relationship shown in equation (1.1.8) is found, therefore explaining Rydberg's original result. Unfortunately, Bohr and Rydberg's expression only works for hydrogenic atoms. Also, Bohr's theory is unable to explain the formation of molecules.^[3,4,6,12]

1.2 The quantum mechanical atom

The accurate description of a hydrogenic atom begins with the wave nature of the bound electron. In his 1924 doctoral thesis, *Recherches sur la Théorie des Quanta (Researches on the quantum theory)*, Louis de Broglie was the first to suggest that any moving object, including electrons, have wave-like properties associated with them. He arrived at his relationship by using Einstein's theory of special relativity, $E = m_0 c^2$ where m_0 is relativistic mass, and Planck's 'quantized'

energy, Equation (1.1.3), to find that

$$\lambda = \frac{h}{p} \quad (1.2.1)$$

Experimental confirmation of de Broglie's relationship came from three experiments, first in 1927 by Clinton Davisson and Lester Germer,^[13] in 1928 by George Paget Thompson, and again in 1932 by Otto Stern. In the serendipitous experiment by Davisson and Germer, an electron beam was focused on a nickel crystal which resulted in a diffraction pattern. For diffraction to occur, the size of the separation of atoms in the diffraction grating (or material) must be similar to the wavelength of the incident light. Their fortuitous result was due to an accident which resulted in their polycrystalline sample unexpectedly sintering into a small number of single crystals.^[3,4,6,12,14]

Thompson's experiment involved focusing an electron beam on a thin sheet of gold foil which resulted in a similar diffraction pattern, that of concentric circles, to the pattern made by a similar experiment with X-rays. As X-rays were known to be waves and diffraction is a property of waves, it was concluded that moving electrons must also have wave-like properties. The third experiment, done by Stern, showed that helium atoms and hydrogen molecules had the same effect; as such, the de Broglie relationship is not confined to just electrons, but can be extended to other microscopic particles. The fact that electrons possess both particle and wave-like properties is termed *particle-wave duality*.^[3,4,6,12,14]

1.2.1 The Schrödinger equation

The time-independent Schrödinger equation for a particle,

$$\hat{H}\psi = E\psi \quad (1.2.2)$$

is an eigenequation where E is energy, ψ is an eigenfunction and \hat{H} is the Hamiltonian operator, which is the sum of the kinetic and potential energy operators and is defined as

$$\hat{H} = \frac{-\hbar^2}{8\pi^2\mu}\nabla^2 + V \equiv \frac{-\hbar^2}{2\mu}\nabla^2 + V \quad (1.2.3)$$

where μ is the reduced mass of the particle in question, ∇^2 is the the Laplacian operator

which is the second partial derivative with respect to each coordinate (e.g. $\frac{\partial^2}{\partial x^2} + \frac{\partial^2}{\partial y^2} + \frac{\partial^2}{\partial z^2}$ for Cartesian coordinates), and V is the potential field in which the particle is moving.

When the ‘particle’ is an atom or a molecule each electron, as well as all of the nuclei, must be considered individually; the subparticles of the nucleus, however, are treated as a whole. Therefore, in the molecular Hamiltonian, the kinetic energy term, T , must include the summation of all n particles:

$$T = -\frac{\hbar^2}{2} \sum_n \frac{1}{m_n} \left(\frac{\partial^2}{\partial x_n^2} + \frac{\partial^2}{\partial y_n^2} + \frac{\partial^2}{\partial z_n^2} \right) \quad (1.2.4)$$

The potential energy term, V , in the molecular Hamiltonian describes how each charged particle interacts with all of the other charged particles in the system. This includes electron-nuclear attraction, electron-electron repulsion and nuclear-nuclear repulsion. When i and j are electrons and k and l are nuclei the expression, in atomic units, is

$$V = -\frac{1}{4\pi\epsilon_0} \sum_i \sum_k \frac{e^2 Z_k}{r_{ik}} + \sum_i \sum_{i<j} \frac{e^2}{r_{ij}} + \sum_k \sum_{k<l} \frac{e^2 Z_k Z_l}{r_{kl}} \quad (1.2.5)$$

where e is the charge on an electron, Z is the atomic number and r_{kl} is the distance between nuclei k and l . The wave function, ψ , must be single-valued, continuous and have a probability density $|\psi|^2 = 1$ over all space.^[15,16] The Schrödinger equation is only exactly solvable for a two body system, such as the hydrogen atom which is solved in polar coordinates. It should be noted that only real, time-independent wavefunctions are assumed in this thesis.

1.2.2 Many body systems

Because the Schrödinger equation cannot be solved for many electron systems, approximations and a description of electron-electron interactions are needed. A complete description of the system requires the inclusion of the nuclear wavefunction as well as the electronic wavefunction and in a system with more than one nucleus, the two body analytical limit is automatically breached. However, the nuclear coordinates can be separated using the Born-Oppenheimer approximation.

The Born-Oppenheimer approximation

The Born-Oppenheimer approximation allows for the separation of the movements of the electrons from the movements of the nuclei. The physical basis is due to the fact that the nucleus is much more massive than the electron and its movements are therefore essentially unaffected by the movements of the electron. Likewise, due to its small size, the electron immediately reacts to movements of the nucleus. Simply stated, the electronic motion can be approximated to that within the field of fixed nuclei.

This approximation allows us to solve the electronic portion of the Hamiltonian which ignores the kinetic energy of the nuclei. This operator can then be substituted into the Schrödinger equation using the electronic wave function to find the effective nuclear potential. This energy value is the output for a single-point energy calculation.

The effective nuclear potential can then be used as the potential in the nuclear Hamiltonian which can be used in the Schrödinger equation. The results from this can be used to predict vibrational spectra.^[15,16]

Coulomb Integral

Electron-electron interactions are described by the coulomb and exchange integrals. The coulomb integral calculates the destabilizing energy due to the electrostatic interaction of two electrons in different orbitals, for example orbital i and orbital j , and is often denoted as J_{ij}

$$J_{ij} = \iint \phi_i^*(r_1)\phi_i(r_1)\left(\frac{e^2}{r_{12}}\right)\phi_j^*(r_2)\phi_j(r_2)dr_1dr_2 \quad (1.2.6)$$

where ϕ_i and ϕ_j are the one electron wavefunctions.^[4,15,17,18]

Exchange Integral

The Pauli principle states that when two identical fermions are exchanged, the sign of the total wavefunction must change or if two identical bosons are exchanged, the sign of the total wavefunction stays the same.^[19] Because electrons are fermions with a spin of $\pm\frac{1}{2}$, the wave function must therefore be anti-symmetric. The exchange integral takes into account the energetic consequences of the Pauli principle by calculating the effect of interchanging two electrons. The

exchange integral is generally denoted as K_{ij} and calculated via

$$K_{ij} = \iint \phi_i^*(r_1) \phi_j^*(r_1) \left(\frac{e^2}{r_{12}} \right) \phi_i(r_2) \phi_j(r_2) dr_1 dr_2 \quad (1.2.7)$$

K_{ij} is only relevant for electrons of parallel spins and is generally much smaller in magnitude than J_{ij} .^[4,15,17,18]

1.3 Modern Computational Approaches

Variational Principle

Arguably, the most important aspect of quantum theory is that it holds the ability to calculate physical observables of a system through the use of an appropriate operator once the molecular wave function is known. The unfortunate downfall is that while we know that the molecular wave function must obey certain rules in order to be mathematically valid, be single-valued and continuous with a probability density of one over all space, the equations within quantum theory do not inform on how such a function might be obtained.

The variational principle gives a systematic approach as to how to find the lowest energy given a normalized guess wave function for the ground state. The guess function, Φ , is dependent upon the electronic and nuclear coordinates and is made up of a linear combination of Ψ_i functions which can be expressed by

$$\Phi = \sum_i c_i \Psi_i \quad (1.3.1)$$

where each Ψ_i is weighted by the corresponding coefficient, c_i .^[15]

A further constraint is that basis functions must be both orthogonal, meaning that they are independent of one another, and normalized. This gives rise to the orthonormality requirement which is represented by the Kronecker delta, $\int \psi_i \psi_j d\mathbf{r} = \delta_{ij}$ where

$$\delta_{ij} = \begin{cases} 1 & \text{for } i = j \\ 0 & \text{for } i \neq j \end{cases}$$

As the guess function is normalized, it follows that

$$\begin{aligned}
\int \Phi^2 d\mathbf{r} = 1 &= \int \sum_i c_i \Psi_i \sum_j c_j \Psi_j d\mathbf{r} \\
&= \sum_{ij} c_i c_j \int \Psi_i \Psi_j d\mathbf{r} \\
&= \sum_{ij} c_i c_j \delta_{ij} \\
&= \sum_i c_i^2
\end{aligned} \tag{1.3.2}$$

If the Schrödinger equation is written in integral form as $\int \Psi_j H \Psi_i d\mathbf{r} = E_i \delta_{ij}$ then

$$\begin{aligned}
\int \Phi H \Phi d\mathbf{r} &= \int \left(\sum_i c_i \Psi_i \right) H \left(\sum_j c_j \Psi_j \right) d\mathbf{r} \\
&= \sum_{ij} c_i c_j \int \Psi_i H \Psi_j d\mathbf{r} \\
&= \sum_{ij} c_i c_j E_i \delta_{ij} \\
&= \sum_i c_i^2 E_i
\end{aligned} \tag{1.3.3}$$

The energy of a guess function could therefore be found from the coefficients if they were known. There must be within the set of E_i a lowest energy, E_0 . Equations (1.3.2) and (1.3.3) are combined to give

$$\int \Psi H \Psi d\mathbf{r} - E_0 \int \Phi^2 d\mathbf{r} = \sum_i c_i^2 (E_i - E_0) \tag{1.3.4}$$

Because all c_i^2 and $(E_i - E_0)$ both must be greater than zero equation (1.3.4) can be rewritten as

$$\int \Psi H \Psi d\mathbf{r} - E_0 \int \Phi^2 d\mathbf{r} \geq 0 \tag{1.3.5}$$

and rearranged to

$$\frac{\int \Psi H \Psi d\mathbf{r}}{\int \Phi^2 d\mathbf{r}} \geq E_0 \tag{1.3.6}$$

yielding

$$\int \Psi H \Psi d\mathbf{r} \geq E_0 \tag{1.3.7}$$

since Φ is normalized. The variational principle thus states that for a system in the ground state with a normalized wave function, the calculated energy is an upper limit to the actual energy

of the system.^[4,15-17] Therefore, for a method that is variational, one could continue to make improvements to the basis set, as far as practical, until a lower limit is reached. For the Hartree-Fock method discussed below this is called the Hartree-Fock limit, commonly denoted as E_{HF} .

1.3.1 Hartree Fock Theory

In Hartree-Fock Theory each electron is approximated to be travelling in an average field created by the other N-1 electrons.

Hartree-Fock Theory employs the iterative, self-consistent-field method to solve the eigenvalue Hartree-Fock equations of the form

$$\hat{F}_i \psi_i = \varepsilon_i \psi_i \quad (1.3.8)$$

where \hat{F} is the Fock operator, a one-electron operator that operates on spatial orbitals:

$$\hat{F}_i = -\frac{1}{2} \nabla_i^2 - \sum_k^N \frac{Z_k}{r_{ik}} + \nu_i^{HF}(i) \quad (1.3.9)$$

where $\nu_i^{HF}(i)$ is the field surrounding the electron and is defined by

$$\nu_i^{HF}(i) = 2\hat{J}_i + \hat{K}_i \quad (1.3.10)$$

when \hat{J}_i and \hat{K}_i are the Coulomb and Exchange operators respectively.^[4,15,17]

The Coulomb operator is a local operator and describes the average potential exerted on electron i due to the other N-1 electrons. The Exchange operator, a non-local operator, described the exchange of two different electrons and is dependent on the value of the spin orbital throughout all space.^[4,15,17]

Size Consistency

A desired property for a quantum mechanical method to possess is size consistency. Within a method that is size consistent the energy as well as the error in energy is proportional to the size of the molecule being calculated. This is very important, for example, when calculating dissociation or addition reactions where the separate species are considerably different in size. A

special case of size consistency is that for infinitely separated systems, meaning that the method gives the same energy for two species calculated separately as if they are calculated together at a distance large enough that no interaction would occur.^[4]

1.3.2 Møller-Plesset Perturbation Theory

Møller-Plesset Perturbation Theory is one way to account for electron correlation. This theory, first described by Møller and Plesset in 1934^[23] but not applied to molecules until 1975^[4], uses the Many Body Perturbation Theory by dividing the Hamiltonian into two parts: a part that is exactly solvable (H_0^*) and the perturbation to it (λV_{MP}^\dagger).^[4,15-17]

$$\hat{H} = H_0 + \lambda V_{MP} \quad (1.3.11)$$

If we assume that the perturbation is small it can be expressed as a power series in V and the Schrödinger equation becomes:

$$(H_0 + \lambda V_{MP})(\psi^{(0)} + \lambda \psi^{(1)} + \lambda^2 \psi^{(2)} + \dots) = (E^{(0)} + \lambda E^{(1)} + \lambda^2 E^{(2)} + \dots)(\psi^{(0)} + \lambda \psi^{(1)} + \lambda^2 \psi^{(2)} + \dots) \quad (1.3.12)$$

One can then equate the coefficients for the same power of λ from one side of the equation with the coefficients from the other side in order to solve for the various values of E :

$$\begin{aligned} (H_0 - E^{(0)})\psi^{(0)} &= 0 \\ (H_0 - E^{(0)})\psi^{(1)} &= (E^{(1)} - V_{MP})\psi^{(0)} \\ (H_0 - E^{(0)})\psi^{(2)} &= (E^{(1)} - V_{MP})\psi^{(1)} + E^{(2)}\psi^{(0)} \end{aligned} \quad (1.3.13)$$

$E^{(0)}$ is simply the sum of orbital energies. MP1, using the first perturbation (i.e. $E^{(0)} + E^{(1)}$), is equivalent to using the Hartree-Fock method. MP2 includes the second perturbation ($E^{(0)} + E^{(1)} + E^{(2)}$), MP3 the third and so on.^[4,15-17]

* H_0 , in this case, is the sum of the one-electron Fock operators (i.e. $H_0 = \sum_i F^i$)

† N.B. V_{MP} is not the same as the potential energy (V) term in the molecular Hamiltonian

Møller-Plesset Perturbation Theory is size-consistent but not variational.^[4,15–17]

1.3.3 Configurational interaction

The Configuration Interaction method, as first described by Nesbet,^[20] is another way to include electron correlation. In this method, the total wavefunction is composed of the Hartree-Fock wavefunction along with a series of excited wavefunctions, Ψ_i :

$$\Psi_{CI} = C_0\Psi_{HF} + C_1\Psi_1 + C_2\Psi_2 + \dots + C_n\Psi_n \quad (1.3.14)$$

Each Ψ_i , known as a configuration state function (CSF), represents a different idealized electron configuration where one or more occupied orbitals are replaced with virtual orbitals; this allows electrons to occupy orbitals other than those of the ground state and potentially decreasing electron-electron repulsion. The inclusion of these CSFs represent many possible configurations of the system. Each wavefunction's contribution is noted by the corresponding C_i with C_0 , the contribution from the Hartree-Fock wavefunction, expected to be the largest when the ground state of a system is being calculated.^[4,15–17,21]

The use of a full CI wavefunction is very appealing in theory as it replaces the wavefunction with a linear combinations of all possible excitations. It is also size-consistent, variational and if combined with an infinite basis set would solve the time-independent, non-relativistic Schrödinger Equation exactly. However, in reality, full CI is very expensive and is only practical for very small systems. For larger systems limited or truncated CI is a less expensive solution as it only takes into account particular excitation. Some examples of this are single (CIS), double (CID), single and double (CISD) or single, double and triple (CISDT) excitations. CISD obeys the variational principle; however, it is not size-consistent, meaning that the energy calculated when there is a large separation between two molecules is not the same as the sum of the energies calculated when the molecules are considered individually.^[4,15–17,21]

1.3.4 Density Functional Theory

Another approach is Density Functional Theory (DFT). DFT models electron correlation and exchange through functionals of the electron density of the system and does not attempt to solve the Schrödinger equation.

The Thomas-Fermi Model

DFT was first alluded to in 1927 by Thomas and Fermi using a uniform electron gas, a gas in which there are an infinite number of electrons in an infinite volume with a uniform positive charge throughout. The Thomas-Fermi model uses a quantum statistical model for the kinetic energy of electrons and classical mechanics to describe the nuclear-electron and electron-electron contributions while completely ignoring effects associated with exchange and correlation. The Thomas-Fermi equation for the energy of an atom is:

$$E_{TF}[\rho(r)] = \frac{3}{10}(3\pi^2)^{\frac{2}{3}} \int \rho^{\frac{5}{3}}(r)dr - Z \int \frac{\rho(r)}{r}dr + \frac{1}{2} \iint \frac{\rho(r_1)\rho(r_2)}{r_{12}}dr_1dr_2 \quad (1.3.15)$$

where $\rho(r)$ is the electronic density. Unfortunately, the Thomas-Fermi model is insufficient as it has been shown that, in this model, molecules are less stable than their atomic counterparts.^[24] However, it was an important first step in the development of density functional theory as it was the first model to define the energy of a chemical system exclusively as a function of the electronic density.^[15,25]

The Slater Approximation

Although not initially developed for DFT, Slater's 1951 approximation to Hartree-Fock exchange^[26] had an impact on the development of density functional theory. Slater suggested that instead of solving for the exact exchange energy and approximating the correlation energy in the Hartree-Fock method, one could ignore the correlation energy and approximate the exchange hole as a sphere with a constant potential centred on the reference electron. The exchange energy then becomes:

$$E_x[\rho(r)] = -\frac{9}{8} \left(\frac{3}{\pi} \right)^{\frac{1}{3}} \alpha \int \rho(r)^{\frac{4}{3}} dr \quad (1.3.16)$$

where Slater assigned α to a value of 1. A similar expression had been derived earlier by Bloch and Dirac where $\alpha = \frac{2}{3}$. Further empirical analysis has shown that a more realistic value is $\alpha = \frac{3}{4}$. This method has largely been abandoned in favour of more modern DFT functionals; however, when used, these computations are typically referred to as the X_α or Hartree-Fock-Slater calculations.^[15,25]

The Hohenberg-Kohn Theorems

In 1964 Hohenberg and Kohn published a paper^[27] including two particularly important theorems. The first of which stated that there exists a universal functional that relates electron density to total energy; although, the form of this functional is unknown. The second theorem shows that the density is variational.^[15,25]

The Existence Theorem

Hohenberg and Kohn's existence theorem is a simple proof that follows from "*reductio ad absurdum*." For simplicity they chose to deal only with non-degenerate ground states. For the Hamiltonian where the potential, V , is defined by

$$V \equiv \int V_{Ext}(r) \psi^*(r) \psi(r) dr. \quad (1.3.17)$$

They assumed that for a particular ground state, Ψ , the electronic density is given by

$$\rho(r) \equiv (\Psi, \psi^*(r) \psi(r) \Psi) \quad (1.3.18)$$

which is a functional of $V_{Ext}(r)$. They then assume that a second potential, $V'_{Ext}(r)$, has an associated ground state, Ψ' , and realizes the same electronic density, $\rho(r)$. Therefore $\Psi' \neq$

Ψ as they correspond to two distinct and different Schrödinger equations. It follows that the Hamiltonians, H and H' , and ground-state energies, E and E' , of Ψ and Ψ' will have the property

$$E' = (\Psi', H'\Psi) < (\Psi, H'\Psi) = (\Psi, (H + V' - V)\Psi) \quad (1.3.19)$$

giving

$$E' < E + \int [V'_{Ext}(r) - V_{Ext}(r)]\rho(r)dr \quad (1.3.20)$$

The same process with the exchange of primed quantities with unprimed ones gives

$$E < E' + \int [V_{Ext}(r) - V'_{Ext}(r)]\rho(r)dr \quad (1.3.21)$$

However, it then follows that

$$E + E' < E + E' \quad (1.3.22)$$

which is, of course, absurd. Hence they find that:

" $V_{Ext}(r)$ is (to within a constant) a functional of $\rho(r)$; since, in turn, $V_{Ext}(r)$ fixes \hat{H} we see that the full many-particle ground state is a unique functional of $\rho(r)$."^[27]

Variational Theorem

A second noteworthy theorem that came out of the 1964 paper shows that the above functional is variational and progresses as follows:

Given the energy functional

$$E_V[\rho] = \int V_{Ext}(r)\rho(r)dr + F[\rho] \quad (1.3.23)$$

where $V_{Ext}(r)$ is a particular external potential and $F[\rho]$ is an all-inclusive functional defined by

$$F[\rho(r)] \equiv (\Psi, (T + U)\Psi) \quad (1.3.24)$$

$E_V[\rho]$ will give the ground state energy, E , when the correct $\rho(r)$ is used which must meet the following requirement

$$N[\rho] \equiv \int \rho(r) dr = N \quad (1.3.25)$$

The energy functional of Ψ' for a system with N particles is

$$E_V[\Psi'] \equiv (\Psi', V\Psi') + (\Psi', (T + U)\Psi') \quad (1.3.26)$$

and has a ground-state, Ψ , with respect to any change in Ψ' as long as N remains a constant.

If Ψ' is the ground-state of a second external potential, $V'(r)$, then

$$E_V[\Psi'] = \int V_{Ext}(r)\rho'(r)dr + F[\rho'] > E_V[\Psi] = \int V_{Ext}(r)\rho(r)dr + F[\rho] \quad (1.3.27)$$

can be deduced from (1.3.24) and (1.3.26), corroborating the minimal character of (1.3.23) in relation to any other external potentials, $V'_{Ext}(r)$. If $F[\rho]$ was known, the ground-state energy could then be easily solved by the minimizing the three-dimensional function for the density.^[27] However, the form of $F[\rho]$ remains unknown.

The Kohn-Sham Approach

In 1965 Kohn and Sham^[28] improved on Hohenberg and Kohn's work. They suggested that the starting point should be a fictitious system in which the electrons do not interact, but having the same overall ground-state density as a real system of interest, one in which the electrons obviously do interact.^[15] Next, they divided the electronic energy into several parts via:

$$E = E^T + E^V + E^J + E^{XC} \quad (1.3.28)$$

where E^T is the kinetic energy, in this case the sum of the kinetic energies of the electrons; E^V is the potential of nuclei-electron attraction and nuclei-nuclei repulsion; E^J is classical electron-electron repulsion and E^{XC} is exchange correlation.^[15,16] As only a system of non-interacting particles is being considered equation (1.3.28) can be expanded to

$$\begin{aligned}
E[\rho(r)] = & \sum_i^N \left(\langle \chi_i | -\frac{1}{2} \nabla_i^2 | \chi_i \rangle - \langle \chi_i | \sum_k^{nuclei} \frac{Z_k}{|r_i - r_k|} | \chi_i \rangle \right) \\
& + \sum_i^N \langle \chi_i | \frac{1}{2} \int \frac{\rho(r')}{|r_i - r'|} dr' | \chi_i \rangle + E^{XC}[\rho(r)]
\end{aligned} \tag{1.3.29}$$

The E^{XC} term is, in itself, composed of two terms: the correction to the kinetic energy to account for the transition from a non-interacting to an interacting system, and all non-classical corrections to electron-electron repulsion.[‡] The exact form of E^{XC} is unknown and so approximations are made in order to solve the equations that make up density functional theory.^[15]

The Kohn-Sham Approach uses the iterative self-consistent field method in order to find the wave functions χ_i that minimize the numerical value of E in equation (1.3.29) through

$$h_i^{KS} \chi_i = \varepsilon_i \chi_i \tag{1.3.30}$$

where χ_i are the wave functions that must provide the exact density \S and h_i^{KS} is the Kohn-Sham one-electron operator which is defined by

$$h_i^{KS} = -\frac{1}{2} \nabla_i^2 - \sum_k^{nuclei} \frac{Z_k}{|r_i - r_k|} + \int \frac{\rho(r')}{|r_i - r'|} dr' + \frac{\delta E^{XC}}{\delta \rho} \tag{1.3.31}$$

which closely resembles the Fock operator.

Although DFT is size-consistent, it is no longer variational once an approximation for E^{XC} has been made. This means that the energy predicted for a system can be lower than the exact energy. One specific example for this is when a single hydrogen atom is calculated. As it is a two body problem it can be solved exactly and gives an energy of -0.5 Hartree. When the BPW91 functional is used however a result of -0.5042 Hartree is found. In this case, the error is due to an over estimation of the $\sum_i^N \langle \chi_i | \frac{1}{2} \int \frac{\rho(r')}{|r_i - r'|} dr' | \chi_i \rangle$ term in equation (1.3.29) which is approximated to be larger than the classical self-interaction energy.^[15]

Because of the approximations made, DFT is, in general, much less computationally expensive than Hartree-Fock based approaches and has found wide use.

[‡]Equation 1.3.29 is given in bra-ket notation. Several notations for a definite integral over all space for two distinct functions can be given by: $\int f_i^* f_j d\tau \equiv \langle f_i | f_j \rangle \equiv (f_i, f_j) \equiv \langle i | j \rangle$ ^[4,17]

[§]this is because E in equation (1.3.29) is exact

Hybrid functionals

B3LYP, a commonly used functional and one used in the following work, is an example of a hybrid functional. Hybrid functionals utilize a mixture of wave function based Hartree-Fock exchange as well as the approximated DFT exchange further expanding the E^{XC} term in equation (1.3.28) to

$$E_{hybrid}^{XC} = c_{HF} E_{HF}^X + c_{DFT} E_{DFT}^X \quad (1.3.32)$$

where the values for the two c s are constants. More specifically the B3LYP functional uses the following

$$E_{B3LYP}^{XC} = E_{LDA}^X + c_0(E_{HF}^X - E_{DFT}^X) + c_X \Delta E_{B88}^X + E_{VWN3}^C + c_C(E_{LYP}^C - E_{VWN}^C) \quad (1.3.33)$$

where $c_0 = 0.20$, $c_X = 0.72$ and $c_C = 0.81$ and were determined by Becke through fitting to known atomization energies, ionization potentials, proton affinities and first-row atomic energies to a set of molecules known as the G1 set.^[16] E_{LDA}^X and E_{B88}^X are the exchange functionals according to the local density approximation and the Becke88 functional, respectively while E_{VWN}^C and E_{LYP}^C are the correlation included in the VWN, Vosko, Wilk, and Nusair 1980 functional,^[29] and the LYP, Lee, Yang, and Parr,^[30] correlation functionals.

1.3.5 Basis sets

The wave function in the Schrödinger equation is constructed by the basis set chosen for the calculation. Basis sets are mathematical descriptions of orbitals and are often comprised of linear combinations of Gaussian functions that approximate Slater-type orbitals.^[15,16]

A Gaussian function in Cartesian coordinates has the form

$$\phi(x, y, z; \alpha, i, j, k) = \left(\frac{2\alpha}{\pi}\right)^{\frac{3}{4}} \sqrt{\frac{(8\alpha)^{i+j+k} i! j! k!}{(2i)! (2j)! (2k)!}} x^i y^j z^k e^{-\alpha(x^2+y^2+z^2)} \quad (1.3.34)$$

where α determines how large the orbital is and i , j and k , which are non-negative integers, give the orbital its shape. When $i + j + k = 0$ the orbital is totally symmetric (i.e. an s orbital) when

$i + j + k = 1$ the function has symmetry about one axis (i.e. p_x , p_y or p_z depending on which $[i, j$ or $k]$ is equal to one).^[15]

There are six combinations that give rise to $i + j + k = 2$ they are x^2 , y^2 , z^2 , xy , xz and yz . The xy , xz and yz are of course the corresponding d orbitals that we all know. Linear combinations of the remaining three give us the $d_{x^2-y^2}$ and d_{z^2} (really $d_{3z^2-r^2}$) orbitals plus a totally symmetric $x^2 + y^2 + z^2$ orbital*. Some basis sets employ all six of the Cartesian combinations while others choose to use only the five made up from the linear combinations, dropping the s type orbital.^[15]

A similar situation exists when $i + j + k > 2$. There are 10 possible combinations when $i + j + k = 3$ which can be used to make up the seven f type orbitals. While when $i + j + k = 4$ there are 15 possible combinations which can be combined as the 10 g type orbitals.^[15]

As stated earlier, basis sets are often comprised of linear combinations of Gaussian functions that approximate Slater-type orbitals. The Slater-type orbitals then have the form

$$\varphi(x, y, z; \{\alpha\}, i, j, k) = \sum_{a=1}^n c_a \phi(x, y, z; \alpha_a, i, j, k) \quad (1.3.35)$$

where there are n Gaussians being considered and c_a is a coefficient used to optimize shape and insure that normalization is met.^[15]

The accuracy of the calculation is only as good as the basis set that is used. True accuracy can only be achieved via an infinite basis set which, for obvious reasons, is not a possibility. The progression of basis sets follows.

Minimal Basis Sets

A minimal basis set uses only the minimum number of orbitals needed to describe the atom (i.e. $1s$ for hydrogen or $1s$, $2s$, $2p_x$, $2p_y$, and $2p_z$ for carbon or oxygen). The $2p$ orbitals are also included in the description of Li and Be, the $3p$ orbitals for Na and Mg and so on. This type of basis set does not produce quantitatively accurate results; however, it may be used as a qualitative tool.^[4,15-17]

One of the most widely used minimal basis sets is STO-3G, a 'Slater Type Orbital' which is approximated by three contracted 'Gaussian-Type Orbitals' and has been defined for H-Xe.^[4,15-17,21]

*The totally symmetric orbital is smaller than the s orbital created with the same α value.

Split Valence

The first step in improving a minimal basis set is to make it split valence. A split valence set uses more than one size of function for each valence orbital. Therefore hydrogen would have two functions, a $1s$ and a $1s'$, which would be different sizes and carbon and oxygen would have a total of nine functions, namely $1s$, $2s$, $2s'$, $2p_x$, $2p'_x$, $2p_y$, $2p'_y$, $2p_z$ and $2p'_z$, where each unprimed function is slightly smaller than, and each primed function is slightly more diffuse than its counterpart in the minimal basis. It is possible to continue in this manner further (i.e. for hydrogen $1s$, $1s'$ and $1s''$, etc.) . The atomic orbital is then described by linear combinations of the orbitals which are scaled with coefficients that are determined through the minimization of the atomic SCF.^[4,15–17]

This type of set is commonly known as a double (or triple or quadruple) zeta set, although this is a bit of a misnomer as a *true* double (or triple or quadruple) zeta set splits the core orbitals as well. Although the lack of splitting in the core does have some effect on the value calculated for the total energy of the system, there is little effect to other values of interest.^[4,15–17]

An example of this type is 6-311G (available for H-Kr). This is a "Triple Zeta" basis set that uses six Gaussian functions to describe the core orbitals, three Gaussians for the inner-most valence orbital, one for the middle, and one for the outer-most valence orbital^[21,31,32] .

Polarized and Diffuse functions

The next step in improving the basis set is to add polarized and diffuse functions to it. The first set of polarized functions, d-type orbitals to the first row, is often denoted by placing an "*" at the end of the basis set. Alternatively, this can be denoted (d) in the same place. A second "*" represents the addition of p-type orbitals to hydrogen atoms; the alternative notation for this is adding (d,p) at the end of the basis set. Adding polarized functions to hydrogen has been shown to be much less important than their addition to heavier elements.

It is also possible to add f-type orbitals to heavier elements and d-type orbitals to hydrogen to further improve the basis set.^[4,15–17]

Diffuse functions are noted via the "+" symbol. Adding a second "+" contributes diffuse functions to hydrogen atoms as well.^[4,15,16] Diffuse functions are needed to accurately calculate anions.^[33–36] Some examples of polarized and diffuse basis sets are below.

- 6-311+G* or 6-311+G(d) - the 6-311G basis set with d-type orbitals and diffuse functions added to heavy atoms.
- 6-311++G** or 6-311++G(d,p) - the 6-311+G* basis set with p-type orbitals and diffuse functions added to hydrogen.
- 6-311+G(3df,2p) - the 6-311+G** basis with two additional sets of d-type functions (for a total of three) and one set of f-type functions added to heavy atoms along with a second set of p-type functions added to hydrogen.
- LanL2DZdp - the LanL2DZ basis set (discussed below) with polarization and diffuse functions added to the p-block elements.^[37,38]

Effective Core Potentials (ECP)

Effective Core Potential or Pseudopotential are commonly used for heavy atoms (mostly third row and beyond). An ECP approximates the repulsive effects of the inner (core) electrons on valence electrons of a heavy atom and may include some relativistic effects. This makes calculating heavy atoms much less computationally expensive. The ECP may approximate all but the valence electrons or may include the outer-most closed shell as part of the 'valence' orbitals.^[4,15,21]

An example is LanL2DZ, which is available for H-Bi excluding He. LanL stands for Los Alamos National Laboratory. One of the most common ECP which, for main group elements, includes a double-zeta polarization set for the valence orbitals only (e.g. 5s and 5p for Sb) with the exception of Tl which includes the 5d orbitals. Relativistic effects are also included from Rb -Bi.^[15,21,38–40]

1.4 Overview of work

Chapter 2 presents a historical background of the experimental and theoretical work done on traditional Group IV Ziegler-Natta catalysis including the generally accepted mechanisms believed to be employed when these systems are used to polymerise olefins. Furthermore, a description of the experimental results obtained when a non-traditional Ziegler-Natta catalyst was subjected to propylene are given as a rationale for the calculations presented in Chapter 3.

Chapter 3 presents a theoretical exploration of a novel class of olefin polymerization catalysts based on the *tris*(amido)titanium(IV) platform. Here, DFT has been used to probe the electronic structure of these compounds in order to provide a rationale for the catalytic activity that is associated with them as well as a possible new mechanism for this type of non-traditional catalyst. Furthermore, Chapter 4 takes a closer look at a large number of potential intermediates that are available for the polymerization reaction discussed in Chapter 3.

In Chapter 5, a series of simple transition metal complexes are calculated and analysed to further understand key aspects of the system. The complexes represent a basic model of the novel catalysts found in Chapter 3 and contain the essential feature of π -acid-base chemistry within the coordination sphere.

Chapter 2

Mechanism and scope of alkene polymerization at Group (IV) metal centres

2.1 History of experimental Ziegler-Natta catalysis

2.1.1 Early beginnings - The Aufbau Reaction

Ziegler-Natta catalysis has proven to be of extreme importance in industry for the production of polyethylene and polypropylene. Although the inadvertent, yet seminal experiment did not occur until 1953, Ziegler-Natta catalysis owes its origins to Karl Ziegler's interest in the experiments of Friedrich and Marvel which took place in 1930. Friedrich and Marvel had polymerised ethylene to low molecular weight polymers through the use of alkyl lithium.^[41]

After the end of World War II, Ziegler took interest in this reaction as well as the reactions of other alkali metal alkyls in search of the mechanism, hoping to optimise the reaction leading to the production of high molecular weight polymers. In their study, they found that alkyl lithium was not a suitable catalyst for this purpose as termination of the polymerisation reaction occurred with the precipitation of lithium hydride. They next turned to lithium aluminium hydride, which was found to react with ethylene to form $\text{LiAl}(\text{Et})_4$. Triethylaluminium turned out to be a better catalyst

than ethyl lithium but still did not produce high molecular weight polymers.^[42] Ziegler dubbed the resulting reaction the "Aufbau reaction" which can be seen in Figure 2.1

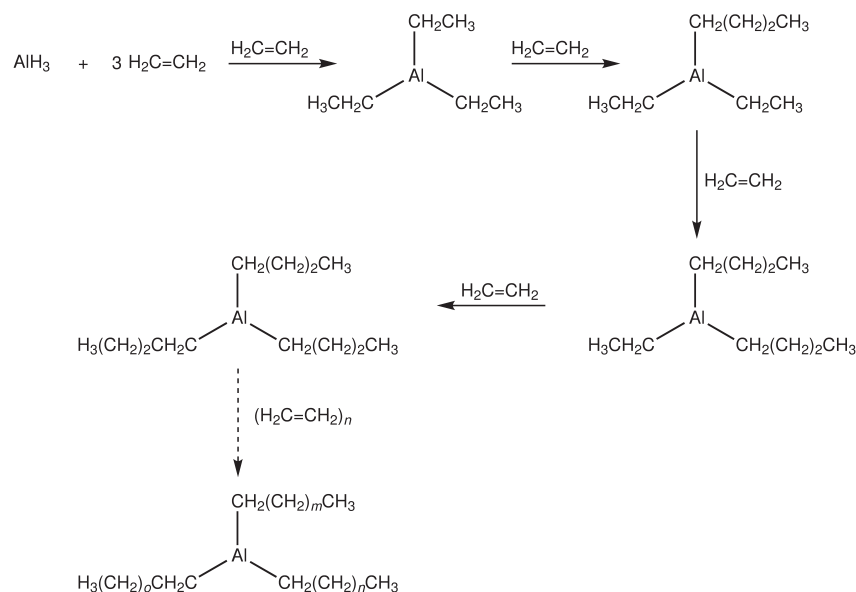


Figure 2.1: The Aufbau reaction

2.1.2 A Serendipitous Experiment

One fortuitous reaction undertaken by Ziegler and Holzkamp while further studying the Aufbau reaction yielded 1-butene as the majority product. As expected the premature termination of the anticipated reaction was caused by an impurity, in this case left over colloidal nickel from an earlier experiment. This 'failed' experiment shed light on a way to optimise the polymerisation reaction. The heterogeneous titanium tetrachloride - triethylaluminium system was found to be the most advantageous of the systems investigated and was used to produce high molecular weight polyethylene. Ziegler named the new reaction the "Mülheim Atmospheric Polyethylene Process."^[42]

Before publishing his work, Ziegler divulged his findings to the Montecatini Company in Italy and the Goodrich-Gulf Chemical Company in the United States. Giulio Natta was consulting for the Montecatini Company at the time and decided to engage in further research of the new catalyst. Natta expanded the scope of the original set of Ziegler catalysts to include titanium trichloride.

Four polymorphs of TiCl_3 are known. The β -form is called brown- TiCl_3 due to the brown colour

of crystalline needles which have a fibre-like structure while the α , δ and γ forms are all violet in colour and vary in the packing structure of the chloride anions. The α -form contains hexagonal close-packed chloride anions and the γ , cubic close-packed, while the δ -form is a mixture of the two. The coordination about the Ti atom is octahedral in all forms. The α polymorph, shown in Figure 2.2, was investigated and was found to produce crystalline polymers of propylene, 1-butene and styrene. Upon inspection, Natta found that the monomeric units within the polymer all had the same configuration and dubbed these types of polymers 'isotactic'.^[42–44]

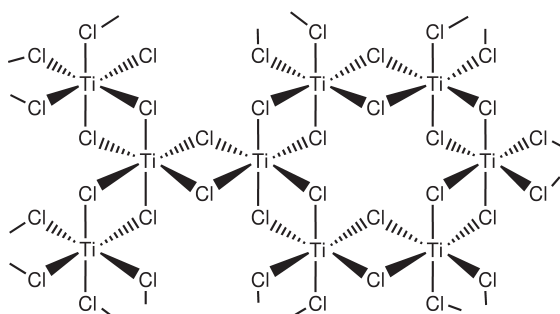


Figure 2.2: α -TiCl₃

The tacticity or orderliness^[18] of the resultant polymer is of particular interest as it determines properties such as hardness and tensile strength that are important for industrial applications.^[45] Isotactic or 'same order' polymers consist of a polymer chain where all substituents are pointed in the same direction. Syndiotactic polymers alter stereocentres at every other carbon along the chain; while atactic polymers do not contain a stereoselective pattern. Examples of the tacticity in polypropylene can be seen in Figure 2.3. Many Ziegler-Natta catalysts give stereoselective/stereoregular polymers. Tacticity has been suggested to be determined by the insertion process arising from two different factors, namely catalyst chirality, known as enantiomorphic site control,^[46] or control attributed to the configuration of the last inserted monomeric unit, known as chain end control.^[47]

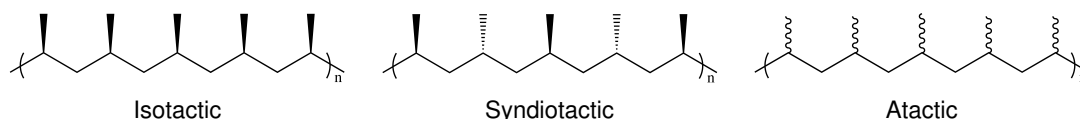


Figure 2.3: Examples of tacticity in polypropylene

Ziegler and Natta were awarded the Nobel Prize in Chemistry in 1963 "for their discoveries in the field of the chemistry and technology of high polymers."^[48]

2.1.3 Homogeneous Ziegler-Natta

In 1985 Kaminsky developed the first homogeneous Ziegler-Natta catalyst that produced isotactic polypropylene;^[49] all previous studies of soluble catalysts had produced atactic material. The novel catalyst was ethylenebis(4,5,6,7-tetrahydro-1-indenyl)zirconium dichloride with methylaluminoxane as a co-catalyst. This and similar homogeneous metallocene catalysts are often referred to as Kaminsky type catalysts.

Activation catalysts

Kaminsky catalysts are often accompanied by a co-catalyst such as methylaluminoxane (MAO), *tris*-(pentafluorophenyl)borane ($\text{B}(\text{C}_6\text{F}_5)_3$) or *tetrakis*-(pentafluorophenyl)borates (exemplified by $(\text{H}_5\text{C}_6)_3\text{C}^+\text{B}(\text{C}_6\text{F}_5)_4^-$ or $\text{K}^+\text{B}(\text{C}_6\text{F}_5)_4^-$). These co-catalysts are expected to serve two functions.

The first function is as an abstraction agent, abstracting either a methide or chloride from the transition metal precursor creating the active species. The second function is to support the cationic active species. The choice of co-catalyst is of particular importance as the ionic pair formed has been suggested to have significant influence over the properties of the resultant polymer as well as the activity and stability of the active species.^[50]

Methylaluminoxane is an industry standard co-catalyst, even though the solid state structure, which has the general formula $[\text{--Al}(\text{CH}_3)\text{--O--}]_n$, has proven elusive.^[50] However, through experimental studies by Barron^[51,52] and theoretical work by Ziegler and others, see for example [53], a three-dimensional cage or cluster type structure is expected. In order for polymerisation to take place, MAO must be used in a large excess; therefore inhibiting full characterization of the active species and a true understanding of MAO's exact role in the activation and polymerisation process. One further drawback is that polymerisation activity of the total system can be dependent on the hydrated salt used as the source of H_2O in the controlled hydrolysis reaction of $\text{Al}(\text{CH}_3)_3$ used to synthesise MAO.^[50]

Due, in part, to the lack of characterisability afforded by activation with MAO, more structurally distinct Lewis acidic initiators were investigated and by the early 1990's Marks^[54,55] and Ewen^[56,57] had developed crystallographically characterisable single-site cationic metallocene catalysts through the use of $\text{B}(\text{C}_6\text{F}_5)_3$. Further experimental studies have shown that $\text{B}(\text{C}_6\text{F}_5)_3$

and its derivatives are strongly coordinating^[55,58–60] and a search for non-coordinating supporting ions followed.

tetrakis-(pentafluorophenyl)borate anions were found to be excellent counter ions that only weakly coordinate to the cationic active species. In particular, some of the highest polymerisation activities reported include $\text{B}(\text{C}_6\text{F}_5)_4^-$ as the supporting anion.^[61]

All work in this chapter is focused on homogeneous catalysts that can be activated by the structurally distinct co-catalysts $\text{B}(\text{C}_6\text{F}_5)_3$ or $\text{B}(\text{C}_6\text{F}_5)_4^-$. While experimental studies have shown that MAO also successfully activates these catalysts,^[62,63] theoretical investigations that include the mechanism of this activation have not been undertaken.

2.2 Experimental Mechanism

Although a number of models for the mechanism of Ziegler-Natta catalysis have been put forth, the two most widely accepted models are the Cossée-Arlman and the modified Green-Rooney mechanisms, which are presented here.

2.2.1 Cossée-Arlman Mechanism

In 1964, the year after Ziegler and Natta won the Nobel Prize, the first widely accepted mechanism for heterogeneous Ziegler-Natta polymerisation was published by Cossée and Arlman.^[64–66] They used molecular orbital theory to devise this mechanism which can be found in Figure 2.4.

The active species in the mechanism contains both a metal-alkyl bond as well as an available vacant site. In the first step the olefin coordinates to the metal centre forming a π complex. The insertion of the olefin then progresses through a four membered transition state where a new metal-carbon bond as well as a new carbon-carbon bond are formed. The original metal-alkyl bond breaks providing a new vacant site for further olefin coordination and the alkyl group has now grown by a C_2 unit.

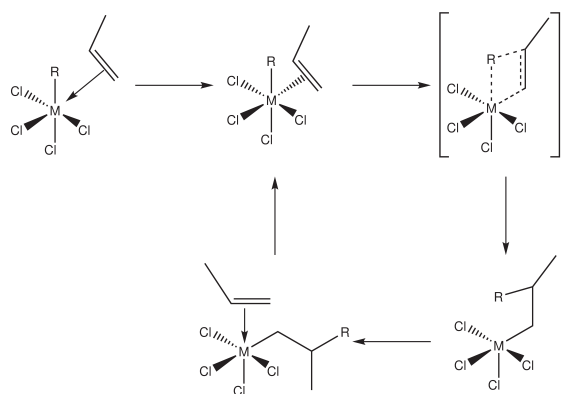


Figure 2.4: Cossée or Cossée-Arlman Mechanism

2.2.2 Green-Rooney Mechanism

In 1978, Green, Rooney and co-workers^[67] proposed a second mechanism for stereospecific polymerisation which was later modified by Brookhart and Green^[68] and by Piers and Bercaw.^[69] The modified Green-Rooney mechanism, which takes agostic interactions into consideration, can be seen in Figure 2.5.

In this mechanism the active species again contains a vacant site as well as a metal-alkyl bond, although the alkyl group is tilted so that one of the α -hydrogen atoms lies closer to the metal, forming an α -agostic bond.^[68] The tilting of the alkyl group allows less steric hindrance at the vacant site for olefin coordination^[70] as well as increasing the electron density to an electron deficient metal centre^[71] such as $[\text{Cp}_2\text{ZrCH}_3]^+$, which will be discussed further in Section 2.3.1.

The insertion progresses through the previously mentioned four membered transition state while maintaining the α -agostic bond. As the original metal-alkyl bond breaks, the now γ -agostic hydrogen bond is replaced with a new α -agostic interaction. The agostic interaction and resultant decreased sterics around the vacant coordination site have been suggested as an explanation for the observed stereoselectivity of many catalysts.^[68,70,72,73,76]

2.3 Calculational Approaches

2.3.1 Ziegler-Natta polymerization

In general, homogeneous Group IV olefin polymerisation catalysts typically begin as pre-catalysts of the form $\text{L}(\text{L}')\text{MR}_2$ where L and L' are electron donating ancillary ligands such as cyclopentadi-

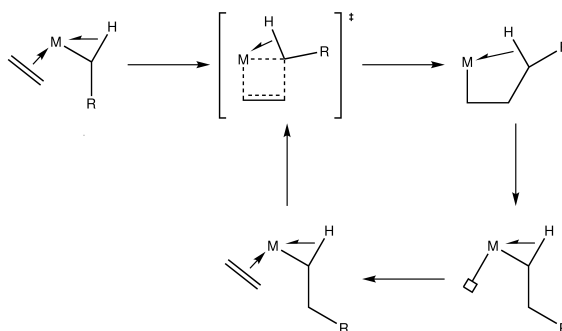


Figure 2.5: Modified Green-Rooney Mechanism

enyl, Cp, or amido groups and R represents an alkyl group.

These pre-catalysts are then activated by a Lewis acidic co-catalyst such as MAO or $B(Ar^F)_3$, where Ar^F is a fluorinated aryl group such as C_6F_5 . As mentioned in Section 2.1.3, the co-catalyst serves two purposes. Firstly, to abstract one of the alkyl groups, typically a methyl group; and secondly to support the newly formed cationic framework. The active species responsible for polymerisation is then thought to be the cationic $L(L')MR^+$ species^[74] with the archetype being $Cp_2ZrCH_3^+$.

A study by Green^[70] has shown the available orbitals in bent metallocene complexes available for bonding by lowering the symmetry of ferrocene through the use of ligand field theory. The symmetry of ferrocene is taken as the highly symmetric eclipsed D_{5h} structure as opposed to the staggered D_{5d} symmetry and subsequently lowered to C_{2v} , a subgroup of D_{5h} and the highest available symmetry for a bent metallocene system.

Figure 2.6 shows a qualitative molecular orbital diagram illustrating the orbital splitting as the symmetry is lowered by increasing the value of α , the angle between the planes of the Cp rings (Figure 2.7). In D_{5h} the metal d orbitals transform as $a'_1 + e'_2 + e'_1$ where the a'_1 and e'_2 sets are formally non-bonding with the ligand set and the ligand based e'_1 set is also non-bonding.

As the symmetry is lowered, the a'_1 and one of the e'_2 orbitals transform as a_1 and mix. The original functions were the $d_{z^2}^*$ and $d_{x^2-y^2}$ although after mixing transform into d_{x^2} and $d_{y^2-z^2}$ in the new coordinate system. The new $d_{y^2-z^2}$ orbital is destabilised due to increasing destructive (anti-bonding) overlap with the ligand π orbitals causing the probability density to lie mostly along the z axis in the direction of the open side of the now bent system.

The other a_1 orbital is only slightly stabilized and lies along the x axis. The other orbital of the

* $d_{z^2} \equiv d_{3z^2-r^2} = d_{2z^2-x^2-y^2}$

original e'_2 set, the d_{xz} becomes b_1 with the probability density pushed into the open side of the molecule. This places the majority of the probability density of the three available orbitals in d^0 metals along the xz plane.^[70]

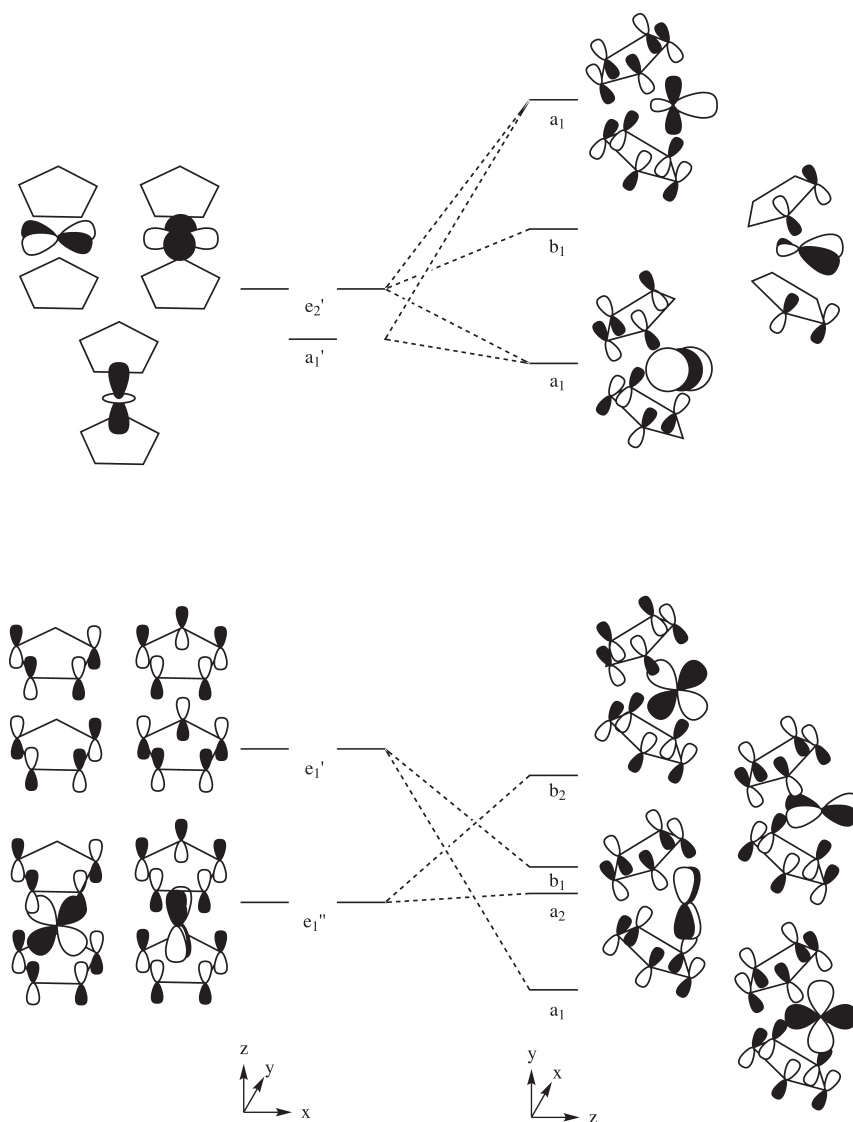


Figure 2.6: Reduction in symmetry from D_{5h} to C_{2v} , adapted from [70]

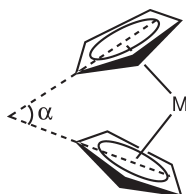


Figure 2.7: Illustration of α , the angle between the planes created by the cyclopentadienyl rings, adapted from [70]

A wealth of theoretical studies of known stereo-specific catalysts and their less computationally expensive derivatives show that, throughout the insertion process, the metal centre, the olefinic

carbons as well as the αC and accompanying stabilising agostic interactions remain planar or near-planar. See, for example, references [72,73,75,76]

A large number of studies^[72,75–92] have examined the reactivity of bare cationic species. Although the anionic counter-ion has been shown to play an important role in the polymerisation process,^[55,61] and calculations of the enthalpy of ion pair separation have shown that total dissociation is unlikely,^[93–95] fewer investigations^[93–102] have included the anion in theoretical mechanistic studies due to the size of the anionic species and resultant computational cost. QM/MM studies are often used to negate some of this computational expense.^[94,100–102]

The first DFT study of Kaminsky catalysts was undertaken by T. Ziegler in 1994.^[75] This report was also the first theoretical study of a Constrained Geometry Catalysts (CGC), in this case the half-sandwich zirconium species, **Z-4**, shown in Figure 2.8. Other catalysts studied were two zirconocene cations, one containing an *ansa*-H₂Si bridge, and a neutral scandocene complex.

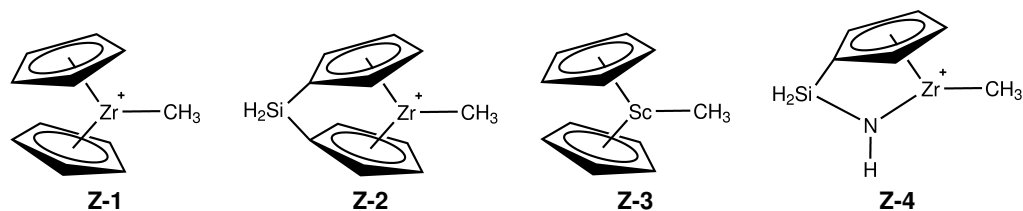


Figure 2.8: Kaminsky catalysts studied by Ziegler *et al.*^[75]

The structures of **Z-1**, **Z-2** and **Z-3** in Figure 2.8 were optimized with C_s symmetry while **Z-4** had no symmetry constraint. The two zirconocene structures exhibit a bent sandwich configuration where the methyl tilt angle is greater than zero showing the possibility of an agostic interaction which is in agreement with experimental evidence of a similar species by Marks.^[54] The methyl tilt angle, θ , is the angle between the M–C vector and the local C_3 axis of the methyl group as seen in Figure 2.9 where the blue line represents the extension of the M–C vector and the red line is the C_3 axis of the methyl group. The energy of the straight configurations, where $\theta = 0$, only varied slightly for each of the systems studied, confirming the findings of an earlier *ab initio* report by Morokuma^[79] stating that the potential energy surface is very flat.

While exploring the insertion of ethylene into **Z-1**, the π complex was found to have a strong agostic interaction between the Zr centre and one of the hydrogen atoms on the methyl resulting in a methyl tilt angle of 40.4° . The ethylene molecule was also found to bind asymmetrically. Due

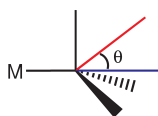


Figure 2.9: Illustration of the methyl tilt angle, θ , the angle between the M–C vector, shown in blue, and the local C_3 axis of the methyl group, shown in red.

to a rather flat potential surface, a true transition state could not be found although an approximate transition state displayed significant agostic interactions. The final product of the insertion was comprised of a strong β -agostic interaction with the newly formed alkyl chain in a staggered conformation. Similar reaction profiles were found for the other catalysts studied with the exception that no stabilization due to agostic interactions was observed in the Constrained Geometry Catalyst, **Z-4**.^[75]

A later review from Ziegler and co-workers^[76] investigated general aspects of both d^0 and $d^0 f^n$ catalysts where the set that was investigated included 11 different ligands and 10 different metals, including Sc^{III} , Y^{III} , La^{III} , Lu^{III} , Ti^{IV} , Zr^{IV} , Hf^{IV} , Ce^{IV} , Th^{IV} and V^{V} . Two types of precursors to olefin uptake were studied, through front-side or back-side attack intermediates, and can be seen in Figure 2.10. Trigonal planar complexes tended to favour the back-side π -complex while trigonal pyramidal complexes typically progressed through the front side π -complex.

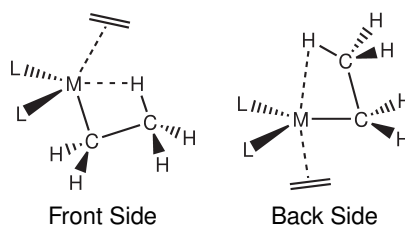
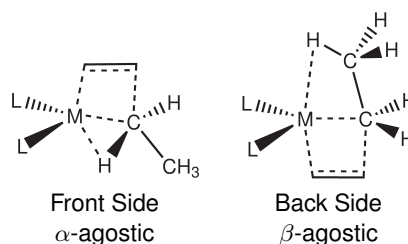


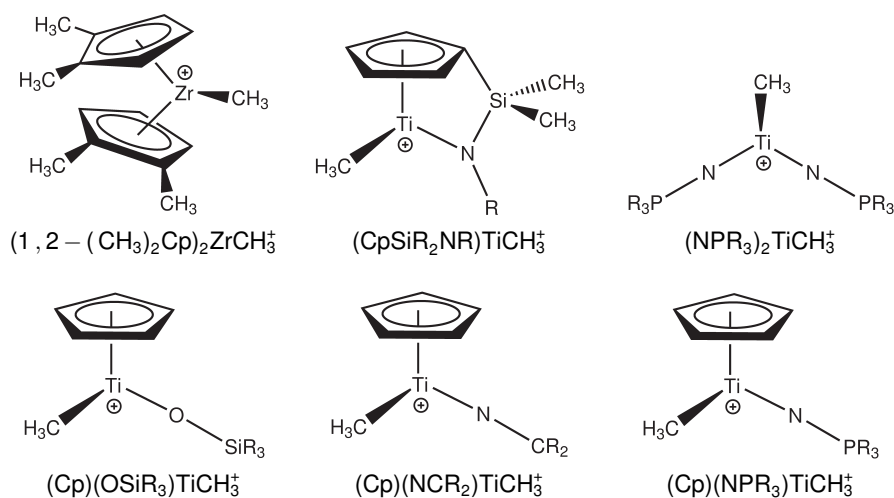
Figure 2.10: Front and Back Side insertion precursors^[76]

Agostic interactions have proven to be an integral aspect of polymerization and have, on numerous accounts, been shown to aid in the stabilization of the carbon network throughout the bond making and breaking process as previously illustrated by Ziegler and co-workers.^[72,73] The π -complexes are one example of the importance of agostic bonds. The transition state that is preceded by the front side π -complex had previously been shown to be stabilised by an α -agostic bond while those starting from the back side π -complex proceeded via a β -agostic transition state during the insertion and propagation process.^[72,73] These transition states can be seen in Figure 2.11.

Figure 2.11: Front and Back Side transition states^[76]

Insertion barriers were found to be low for all complexes, but were dependent on both the ligand set as well as the metal used. Those having a stronger propensity for a trigonal planar precursor were generally smallest. Tendency towards a trigonal planar geometry at the metal centre, decreases as you go down a group as well as moving from group 3 to group 4. Ligands that are good π donors are also more likely to adopt a trigonal planar structure. Complexes made of small metals and good π donor ligands were observed to have the smallest insertion barriers. However, this leads to the potential loss of stereospecific control for the polymerisation of higher α -olefins since the stability of the trigonal planar geometry of the transition state will only lead to a small energetic gain for the “swinging” motion necessary to produce stereoregular polymers.^[76,90,91]

In another survey,^[94] Ziegler took a closer look at the importance of the counter-ion through a study of the enthalpy of several different processes for a subset of six different catalysts along with four co-catalysts. The catalysts and co-catalysts can be seen in Figures 2.12 and 2.13, respectively.

Figure 2.12: Cationic catalyst species studied by Ziegler and co-workers^[94]

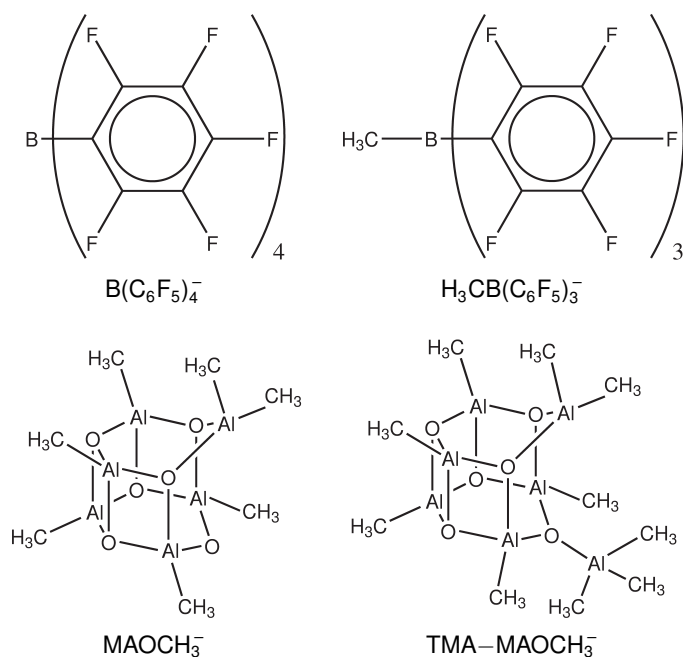


Figure 2.13: Anionic co-catalyst species studied by Ziegler and co-workers.^[94]

The values discussed include, (i) enthalpy of ion pair formation, ΔH_{IPF} , the energy change observed in formation of a contact ion pair from the neutral species. All reactions were exothermic, (ii) enthalpy of ion pair separation, ΔH_{IPS} , the energy change observed due to the separation from a contact ion pair to separate ions, (iii) enthalpy of complexation, ΔH_c , energy gained or lost due to the formation of the cation-olefin adduct, (iv) internal barrier to insertion, ΔH_{ib} , the energy needed to form the four-centred transition state and (v) total barrier to insertion, ΔH_{tot} , the total insertion barrier, $\Delta H_c + \Delta H_{ib}$,

Ziegler proposed a modification to the mechanism to include the interaction with the anion. In this mechanism, shown in Figure 2.14, the local pseudo-tetrahedral coordination around the metal centre distorts to a pseudo-trigonal bipyramidal geometry with the loosely coordinated anion in one of the axial positions. The ancillary ligands lie in the trigonal plane and the incoming olefin can coordinate either in the plane, *cis*, or in the other axial position, *trans*, with the alkyl group filling the other position.

For each of the cations studied, the $\text{B}(\text{C}_6\text{F}_5)_4^-$ anion was found to have the lowest ΔH_{IPS} and, therefore, the weakest interactions. Bridging $\text{H}_3\text{CB}(\text{C}_6\text{F}_5)_3^-$ was considerably higher followed by TMA-MAOCH_3^- just slightly higher and MAOCH_3^- had the highest values. Within the same anion, the ΔH_{IPS} for the series of cations followed a clear trend which reflected the ability of the

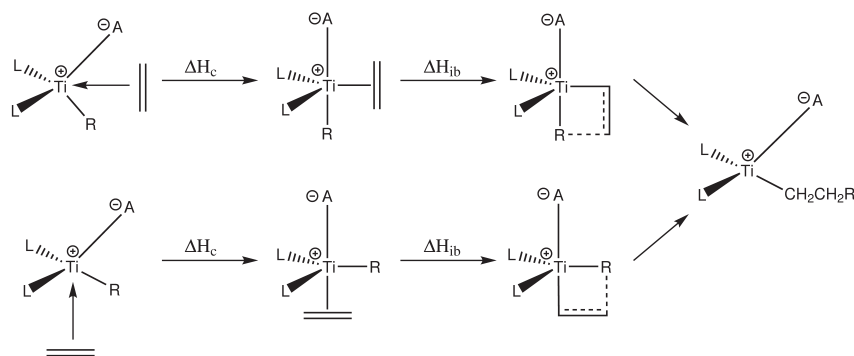


Figure 2.14: Mechanism for complexation and insertion in the presence of the counterion. [94]

ancillary ligands to donate electron density to the metal and therefore better able to stabilize the electron poor metal centre. The ancillary ligands that were the most stabilising were $(\text{CH}_3)_2\text{Cp}$ and $(\text{CH}_3)_3\text{PN}$. Increasing the bulkiness of the R groups of the ancillary ligands was investigated and resulted in a lowering of the ΔH_{IPS} and was attributed to both the greater electron donating power of, for example $\text{C}(\text{CH}_3)_3$ vs. CH_3 , as well as the destabilisation of the contact ion pair due to increased steric bulk. [94]

The enthalpy of ion pair formation, ΔH_{IPF} which exhibits the relative stability of the contact ion pair formed from the neutral species, was investigated for systems containing anions $\text{H}_3\text{CB}(\text{C}_6\text{F}_5)_3^-$, $\text{TMA}-\text{MAOCH}_3^-$ and MAOCH_3^- . All of the ion pair formations were found to be exothermic and the same trend that was seen in the ΔH_{IPS} was found. The trends seen in the energy required to separate the contact ion pair, ΔH_{IPS} , and the energy gained by the formation of the ion pair from its neutral components, $-\Delta H_{IPF}$, are therefore opposite indicating that the cation serves as an acid giving up a base in both cases and suggests that for a series of cations with the same anion the more acidic the cation, the larger the energy requirement for ion pair separation and the smaller the energy gain from the ion pair formation. [94]

The energy change for the complexation to form the adduct with ethylene, ΔH_c , and the internal barrier to insertion, ΔH_{ib} , via the mechanism shown in Figure 2.14 was investigated for both the *cis* and *trans* isomers where $\text{H}_3\text{CB}(\text{C}_6\text{F}_5)_3^-$ was the counterion and hydrogen used as the R group in the ancillary ligands. It was seen that the displacement of the anion was only 1-1.5 Å from the cation at the time of insertion and that while the total barriers of insertion, ΔH_{tot} , for the *cis* and the *trans* forms were similar the most important factor in the height of the barrier was the displacement of the anion. A correlation can also be seen between ΔH_{IPS} and ΔH_{tot} sug-

gesting that catalysts with smaller ion pair separation energies will be more active polymerisation catalysts than those with a higher ion pair separation energy.

Effects due to the nature of the metal were studied by changing the metal centre to zirconium. The total barriers for the zirconium systems were smaller than those for titanium and the *cis* forms were particularly stable due to a negative complexation energy. Steric effects were examined by changing the R groups from hydrogen to $C(CH_3)_3$ in the titanium systems. Overall, this gave higher insertions barriers but again the *cis* forms were more favourable due to a smaller complexation energy.

In $[(Cp)(NCR_2)TiCH_3]^+[H_3CB(C_6F_5)_3]^-$, where $R=C(CH_3)_3$, the reaction coordinate was taken as the distance between the midpoint of the ethylene molecule and the carbon atom of the bridging methyl group. In the initial coordination complex of the *cis* form, the ethylene moiety lies in the trigonal plane, perpendicular to the axial methyl and counterion and the $Ti-\mu-C$ distance increases from 2.19 Å to 2.39 Å and is 26.8 kJ mol⁻¹ higher in energy than the separated species. This was followed by the rotation of the ethylene to the in plane π complex with a barrier of 10.9 kJ mol⁻¹. In the transition state of the insertion, which lies 16.7 kJ mol⁻¹ above the in plane complex, the $Ti-\mu-C$ distance elongated to 2.50 Å but then returned to a value of 2.17 Å after insertion was complete. The total barrier for the insertion was found to be 54.4 kJ mol⁻¹ with the rate determining step being the barrier to insertion. A graph showing this energetic landscape can be found in Figure 2.15.

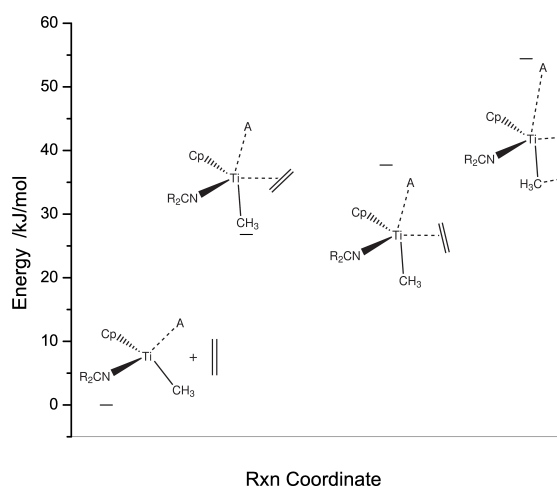


Figure 2.15: Energetic landscape of the insertion of propylene into $[(Cp)(NCR_2)TiCH_3]^+[H_3CB(C_6F_5)_3]^-$ [94]

In the second insertion, the *cis* pathway was again found to be the lowest in energy; however,

the barrier to the formation of the π complex, which was associated with a much larger Ti— μ —C elongation of $> 4 \text{ \AA}$, was the rate determining step. Both the π complex and the transition state to insertion exhibited an α -agostic bond.

2.4 Rationale for study

$[\text{Cp}_2\text{ZrCH}_3]^+$ is the archetype for Group IV single-site olefin polymerisation catalysts. In experimental studies, the catalyst typically starts as the $\text{Cp}_2\text{Zr}(\text{CH}_3)_2$ precursor before a methide ion is abstracted by use of a co-catalyst such as methylalumoxane (MAO) or *tris*-pentafluorophenyl borane ($\text{B}(\text{C}_6\text{F}_5)_3$) to form an ion pair including the $[\text{Cp}_2\text{ZrCH}_3]^+$ active species. Along with being cationic, the active species contains two structural features that are needed for conventional Ziegler-Natta catalysis, namely (i) a vacant site for coordination of the incoming α -olefin and (ii) a metal-alkyl bond where the monomer is inserted during the reaction. The counter-ion is usually weakly bound to the metal centre. A further important feature is the inclusion of a d^0 metal centre with a covalent bond classification^[71] (CBC) of ML_4X_3^+ with the neutral class being ML_3X_4 providing a 14-electron, Lewis acidic, system.

A set of systems of type $[(\text{R}_2\text{N})_3\text{Ti}]^+$, have a CBC classification of ML_3X_3^+ or ML_2X_4 neutral class giving d^0 , 12-electron species that contain both the necessary positive charge as well as a vacant site. Systems of type $(\text{R}_2\text{N})_3\text{TiCH}_3$ are also d^0 , with a CBC classification of ML_3X_4 and are 14-electron systems, which contain a metal-alkyl bond. While a positively charged species and both of the structural features needed for conventional Ziegler-Natta catalysis are present within the total *tris*amido titanium platform, they occur in two separate species.

Experimental studies by Dr. T. N. Williams (University of Sussex 2010)^[62] have shown that systems of type $[(\text{R}_2\text{N})_3\text{Ti}]^+[\text{B}(\text{C}_6\text{F}_5)_4]^-$, as well as $(\text{R}_2\text{N})_3\text{TiCl}$ or $(\text{R}_2\text{N})_3\text{TiCH}_3$ when aided by a co-catalyst polymerise propylene *via* a pseudo-first order reaction. When the $(\text{R}_2\text{N})_3\text{TiCH}_3$ system is used without an activation catalyst, no reaction occurs.

Polymerisation studies undertaken by Dr. Williams were conducted at sub-ambient temperatures and pressures with a low concentration of catalyst used, making the characterisation of the reaction rate possible and catalyst deactivation easily detectable. For each reaction a known mass of the solid catalyst, and activator where applicable, were added to a volume calibrated am-

poule in a glove box with an argon atmosphere. The ampoule was then evacuated and a known volume of pre-dried toluene added *via* vacuum transfer on a high-vacuum line. The toluene solution was then cooled to 0.0°C in an ice bath, dry propylene monomer was expanded into the volume-calibrated line and a pressure reading taken. Once the solution was suitably cooled, the ampoule was opened to monomer feed and pressure readings were taken in 30 second intervals starting from the first exposure of monomer until all the monomer was consumed. Polymerisation reactions were complete after approximately 20 minutes.^[62]

For the $(R_2N)_3TiCl$ systems, investigations were made on both the pre-made catalysts, where the chlorine atom of the $(R_2N)_3TiCl$ precursor had previously been abstracted by $K^+[B(C_6F_5)_4]^-$ and KCl removed providing $[(R_2N)_3Ti]^+[B(C_6F_5)_4]^-$, as well as *in situ*, where $(R_2N)_3TiCl$ was activated by one equivalent of $K^+[B(C_6F_5)_4]^-$ or an excess of MAO within the reaction flask. The $(R_2N)_3TiCH_3$ systems were activated by $B(C_6F_5)_3$ to form $(R_2N)_3TiCH_3B(C_6F_5)_3$ and both *in situ* as well as pre-made catalysts were investigated.

The experimental rate law for these reactions is given by

$$\nu = k[C_3H_6][TiP_n] \quad (2.4.1)$$

where $[TiP_n]$ is the concentration of the catalysts attached to the polymer chain made up of n monomers. If the reaction is first order then $[TiP_n]$ would remain approximately constant, thereby making the rate law

$$\nu = k[C_3H_6][TiP_n] \approx k'[C_3H_6] \quad (2.4.2)$$

where $k' = k[TiP_n]$ and the graph $\ln P_{C_3H_6}$ vs. t would realise a linear plot. The slope of the best fit line can then be found and is proportional to k and k' . If, however, the concentration of the catalyst is not constant, the plot will deviate from linearity, reflecting the change in concentration of the catalyst.

A linear plot was not found, but instead a graph indicative of first order decay. One of the experimental plots, that of $\ln P_{C_3H_6}$ vs. t for $[Ti(dpa)_3]^+[B(C_6F_5)_4]^- + C_3H_6$ where dpa is the diphenylamido ligand, can be seen in Figure 2.16(a), and is typical of the other reactions investigated.

Making the assumption that the reaction between propylene and the titanium catalyst is in fact first order, then one explanation for the departure from linearity seen in Figure 2.16(a) would be the decay of the original catalyst. Figure 2.16(b) shows the fit of the data to a single exponential suggesting that the deviation from linearity is due to a first order decay of the catalyst.

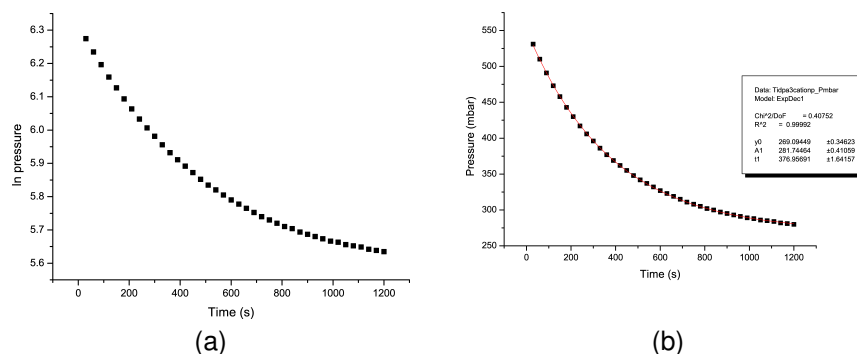


Figure 2.16: (a) $\ln P$ vs. t for the reaction $[\text{Ti}(\text{dpa})_3]^+[\text{B}(\text{C}_6\text{F}_5)_4]^- + \text{C}_3\text{H}_6$ and (b) Fit to a first order exponential

Several possible routes of decomposition including unintentional exposure to oxygen or water were ruled out as the compounds are extremely sensitive and are accompanied by a characteristic colour change of the catalysts when reacted with oxygen which was not observed. The ability to restart the polymerisation reaction with the addition of a further aliquot of propylene when the $[(\text{R}_2\text{N})_3\text{Ti}]^+[\text{B}(\text{C}_6\text{F}_5)_4]^-$ systems were being used also suggests that this type of decomposition is not taking place.

β -hydride elimination, a typical method of termination, was also excluded due to experimental evidence that the hydride complexes are very unstable as well as the fact that resulting predicted species of such a reaction, namely $[(\text{R}_2\text{N})_3\text{TiH}]^+[\text{B}(\text{C}_6\text{F}_5)_4]^-$, is formally ML_3X_4^+ or ML_2X_5 giving an un-physical Ti^{V} species. It is hypothesised that some other structural change is taking place. This assumed structural change along with the catalyst's continued ability to polymerise propylene and lack of structural elements possessed by traditional Ziegler-Natta catalysts suggests that a mechanism different from the currently accepted Cossée-Arlman or modified Green-Rooney mechanisms is taking place. Calculated structures of key points along a purposed mechanism have been investigated and are presented in Chapter 3.

Chapter 3

Examination of a new mechanism for alkene polymerization at *tris*(amido)titanium centres

3.1 Introduction

In light of the experimental evidence found in Section 2.4, a new mechanism for the polymerisation of propylene at a *tris*(amido)titanium centre is needed. To this purpose, calculations of potential species along the reaction coordinate including the initiation and propagation steps of the polymerization were undertaken and are presented below.

3.2 Computational Detail

Density Functional Theory calculations were undertaken in the gas phase using the B3LYP^[30,103] functional as implemented within the G03^[104] and G09^[105] suites. Due to the large size of the systems and associated computational expense, the LanL2DZ^[38,40] pseudopotential was employed for all atoms and the experimental counter-ion, $\text{B}(\text{C}_6\text{F}_5)_4^-$, has been ignored as it has previously shown to be only weakly coordinating.^[61,94] Each structure was confirmed as a local minimum *via*

a frequency calculation which yielded no negative eigenvalues.

Orbital composition data were acquired through the use of GaussSum 2.2.^[106] For each orbital composition calculation, the molecule was divided into groups consisting of the ligand, metal and other substituents where appropriate. The covalent bond classification (CBC) electron counting method as developed by Green^[71] has been employed in this chapter to aid in the description of the novel compounds that follow.

3.3 Structure and reactivity of [(dpa)₃Ti]⁺ (**1**)

3.3.1 Structure

The amido ligand is most often assigned the CBC classification of LX, reflecting the π -basic function on N as well as the σ -symmetry, single electron interaction. As such, the charged class for the *tris*(diphenylamido)titanium(IV) cation ([(dpa)₃Ti]⁺, **1**) is ML₃X₃⁺ with the neutral class represented by ML₂X₄. This gives rise to a formal oxidation state of four making Ti a d^0 metal centre and the complex a 12-electron system. This class makes up only 7% of known Ti complexes while the most abundant class (49%) is ML₄X₄, which is comprised of d^0 16-electron systems.^[107] Due to the electron-poor nature of **1**, it is highly Lewis acidic.^[62,63]

All calculations on the cationic species, **1**, show that the titanium metal centre lies above the N₃ plane. Therefore, if the three diphenylamido ligands are symmetrically arranged around a trigonal rotation, the most symmetrical point group available for the molecule is C_{3v} . Calculations were undertaken without symmetry restrictions culminating in a minimum on the potential energy surface with C_1 symmetry due to small variations in bond lengths and angles.

Through examination of the energies and visualizations of the calculated molecular orbitals it is apparent that, although not formally calculated as such, the molecule is pseudo- C_3 symmetric. For the purpose of this discussion, sets of orbitals that have similar compositions as well as nearly identical energies will be considered as E states. Calculations on selected systems with C_3 symmetry imposed gave negligible energy differences of order 0.1 kJ mol⁻¹.

The calculated structure of **1** as viewed down the pseudo- C_3 axis and from the side can be seen in Figure 3.1. The three nitrogen atoms lie in a plane 1.10 Å below the titanium metal

centre while the phenyl rings are arranged in a paddle-wheel type arrangement above and below the plane. The phenyl rings situated above the plane are tilted in toward the metal centre in a stabilising interaction involving the *ipso*-carbons.

A similar interaction is found in the structures of tetrabenzyl titanium,^[109] tetrabenzyl zirconium and tetrabenzyl hafnium.^[110] This feature has been previously attributed to a presumed overlap between a filled π orbital on the benzyl group with an empty d orbital on the metal centre^[109,110] and will be discussed further in Section 3.3.2

The average calculated Ti—*ipso*C distance for the interacting carbons is 2.503 Å while the average Ti—N—C angle is 96.60°. For the non-interacting rings, the average Ti—*ipso*C distance is 3.125 Å and the average Ti—N—C angle is 141.50°.

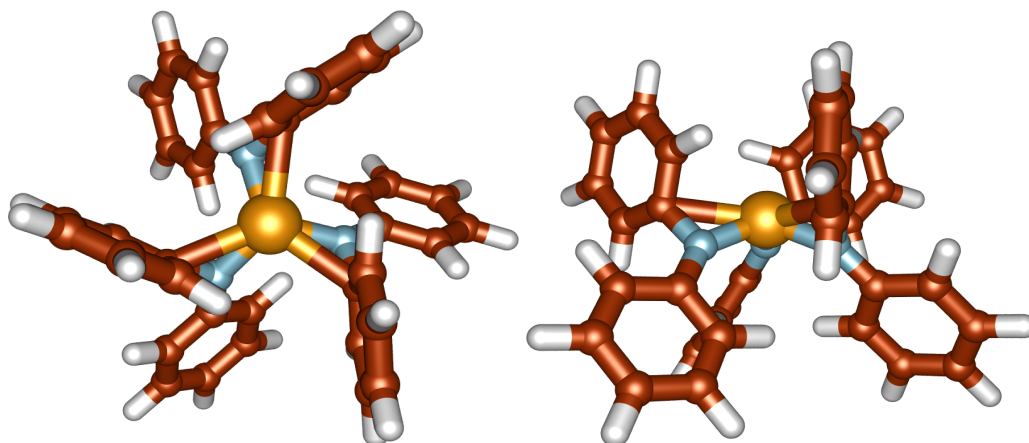


Figure 3.1: Calculated structure of [(dpa)₃Ti]⁺, **1**

3.3.2 Analogous species

tetrakis(diphenylamido)titanium (IV), (dpa)₄Ti

The structure of (dpa)₄Ti has been calculated at the B3LYP/LanL2DZ level without symmetry restraints for comparison. The starting point for the optimisation was taken from the crystallographic coordinates found on the CSD.^[111,112] The crystal structure was solved in 1998 by Dehnicke.^[113] The calculation converged to a C_1 symmetric structure with local tetrahedral symmetry about the Ti atom. Key bond lengths and angles for the experimental and calculated structures of (dpa)₄Ti as well as the corresponding information of the calculated structure of **1** can be seen in Table 3.1.

Calculated bond lengths for (dpa)₄Ti are slightly longer than in the crystal structure, although

	(dpa) ₄ Ti Experimental ^[113]	(dpa) ₄ Ti Calculated	Δ^a	[(dpa) ₃ Ti] ⁺ , 1 Calculated
Ti–N	1.938	1.945	0.007	1.880
N–C	1.433	1.444 ^b	0.011	1.426 ^b
	1.437	1.446 ^c	0.009	1.450 ^c
Ti–C	3.037	3.031 ^b	-0.006	3.125 ^b
	2.910	2.927 ^c	0.017	2.503 ^c
N–Ti–N	109.56	109.52	-0.04	109.05
C–N–C	113.40	114.97	1.57	121.87
Ti–N–C	127.66	126.25 ^b	-4.41	141.50 ^b
	118.59	118.62 ^c	0.03	96.60 ^c
N–Ti–N–C	15.19	15.08 ^b	-0.11	19.23 ^b
	85.23	83.47 ^c	-1.76	79.36 ^c
	36.68	38.27	1.59	41.14 ^{c,d}

^a Calculated - Experimental

^b non-interacting carbons (*vide infra*)

^c interacting carbons (*vide infra*)

^d torsion from the pseudo-C₃ axis

Table 3.1: Averaged bond lengths /Å and angles /° of (dpa)₄Ti and [(dpa)₃Ti]⁺, **1**

the elongation is less than 1% of the solid state structure as revealed by the Δ values seen in Table 3.1. When the calculated structures of (dpa)₄Ti and **1** are compared Ti–N bond lengths contract as is expected due to the formation of a formal cationic species. The average N–Ti–N angle also decreases and the titanium centre, previously close to the centroid of the N₄ tetrahedron located 1.16 Å from the tetrahedral face, relaxes to a position 1.10 Å above the N₃ plane on removal of the fourth ligand.

The symmetry about the nitrogen atoms in the dpa ligand exhibits the most significant change. In all species listed in Table 3.1 the sum of the angles around the nitrogen atom is 360° giving the expected trigonal planar symmetry for an amido ligand, although the bisection of this angle is not even as can be seen in Figure 3.2(a).

A consequence of this unequal bisection is that the two phenyl groups of the amido ligand are not equivalent. When viewed down one of the N–Ti bonds, as in Figure 3.2(b), the phenyl group associated with the larger Ti–N–C angle has a torsional distortion of only 15° from the Ti–N bond of another ligand. The *ipso*C of the second phenyl ring in turn lies closer to the titanium centre by more than 0.1 Å. The *ipso*C of the second phenyl ring, which lies closer to the metal centre, is denoted in Table 3.1 as the “interacting carbon.”

Without the constraint of a fourth ligand, this torsion is increased to 19° in **1**, allowing the

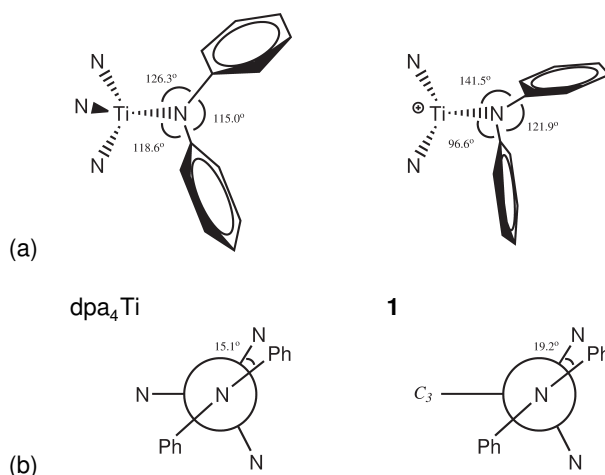


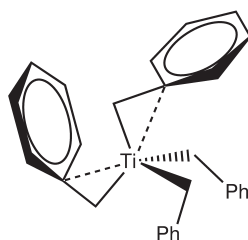
Figure 3.2: (a) Bisection of the trigonal plane about the nitrogen atom and (b) torsional angles in dpa_4Ti and **1**

stronger interaction from the *ipso*C of the second phenyl ring which lies closer to the titanium centre by more than 0.6 Å compared the the $\text{Ti}-\text{ipsoC}$ distance for the non-interacting carbon atom.

Tetrabenzyl titanium, Bz_4Ti

Tetrabenzyl titanium has a CBC classification of MX_4 and is an exceptionally electron poor, 8-electron system; the MX_4 classification makes up only 6% of known Ti complexes.^[107] A schematic structure of tetrabenzyl titanium can be seen in Figure 3.3. Although crystallographic coordinates were not available, the crystal structure at room temperature solved by Bassi *et al.*^[109] has been stated to exhibit a slightly distorted tetrahedral environment around the titanium centre with the *ipso*-carbons of two of the benzyl rings much closer to the metal centre with $\text{Ti}-\text{ipsoC}$ distances of 2.61 Å and 2.81 Å and $\text{Ti}-\alpha\text{C}-\text{ipsoC}$ angles of 88° and 98° , respectively. The $\text{Ti}-\text{ipsoC}$ distances for the other two rings are 3.16 Å and 2.95 Å with corresponding $\text{Ti}-\alpha\text{C}-\text{ipsoC}$ angles of 116° and 108° .^[109] A further structure of tetrabenzyl titanium was determined at 233K by Davies and co-workers.^[110] Although crystallographic coordinates were not available and few details of the geometry were given for the low temperature structure, it was stated to be in good agreement with the structure found by Bassi *et al.*^[110]

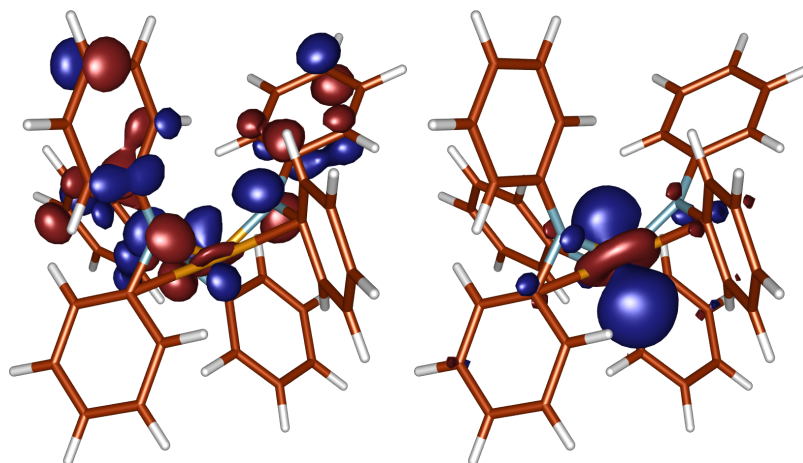
The interaction of the benzyl rings has been attributed to a presumed overlap between a filled π orbital on the benzyl group with an empty d orbital on the metal centre,^[109,110] although, there has been a surprising lack of theoretical investigations of the system. One study using the ex-

Figure 3.3: $((\text{C}_6\text{H}_5)\text{CH}_2)_4\text{Ti}$

tended Hückel method to investigate the benzyl containing zirconium cation $[(\text{CH}_3)_5\text{Cp}]\text{Zr}(\text{Bz})_2]^+$ found a bonding interaction between the π system of one of the benzyl groups and the zirconium centre.^[114]

3.3.3 Electronic structure

The HOMO and LUMO of **1** can be seen in Figure 3.4. It is clear to see that the majority (over 72%) of probability density of the LUMO is based along the pseudo C_3 axis on the metal centre. This orbital, which is 2.81 eV higher in energy relative to the HOMO, is therefore available for bonding with a fourth substituent and is consistent with its noted Lewis acidity.^[62,63]

Figure 3.4: $[(\text{dpa})_3\text{Ti}]^+$ HOMO and LUMO

Group	HOMO	LUMO
Ti	8.18	72.24
dpa-1	30.46	9.25
dpa-2	30.29	9.28
dpa-3	31.05	9.22

Table 3.2: Orbital composition (%) of $[(\text{dpa})_3\text{Ti}]^+$

Through further inspection of the calculated molecular orbitals of **1**, an interaction between one

of the π orbitals on each of the interacting phenyl rings and the d_{xy} and $d_{x^2-y^2}$ orbitals on Ti can be found within the HOMO-5 E set which lies 1.67 eV lower in energy than the HOMO. To further inspect the stabilising effects of this interaction the potential energy surface was investigated where the Ti–N–C angle was taken as the reaction coordinate. For each point the Ti–N–C angles were frozen while the remainder of the molecule was allowed to relax. The energy surface diagram can be seen in Figure 3.5 and indicates a steady rise in energy as the dpa ligands are pulled back causing the exposure of the ‘naked’ cationic metal centre.

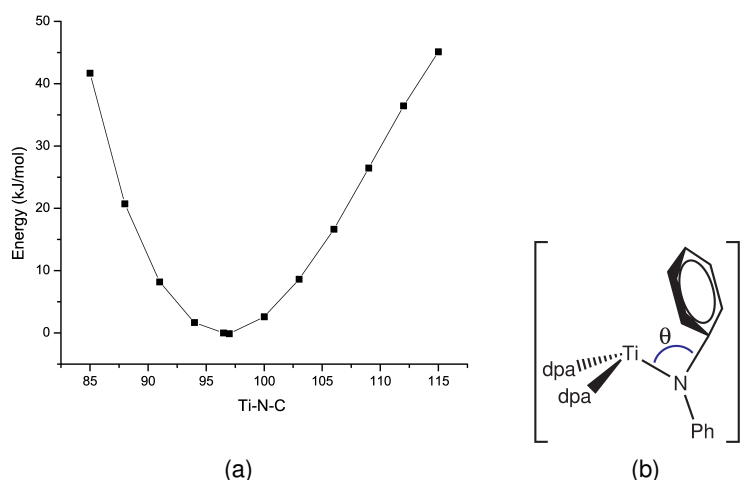
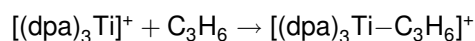


Figure 3.5: (a) Potential energy surface of the reaction coordinate Ti–N–C, θ and (b) pictorial description of the Ti–N–C angle, θ

The nitrogen π , L-type function, lies lower in energy at the HOMO-9 level and is 2.85 eV lower than the HOMO.

3.3.4 Reactivity

The $[(\text{dpa})_3\text{Ti}]^+$ system has been shown experimentally to polymerise propylene.^[62,63] Considering the requirements of traditional Ziegler-Natta catalysis this would not be expected as no metal-alkyl bond is present for the insertion of monomer. Therefore, polymerisation must take place through a different mechanism. The elucidation of this new mechanism began with a calculation of the structures of propylene as well as a possible product of the reaction



Possible methods for the addition of a second propylene moiety to the $[(\text{dpa})_3\text{Ti}-\text{C}_3\text{H}_6]^+$ adduct, **2**, were then investigated. The first placed the incoming propylene above the bound

propylene moiety of the adduct and proved unsuccessful. The second route tried placed the incoming propylene in a position to donate electron density into the Ti–N π^* orbital and resulted in an intermediate containing a pseudo-six-membered ring consisting of the previous alkene carbons of both propylene moieties as well as the titanium centre and the nitrogen atom of one of the ligands.

Structure of propylene

The structure of propylene was calculated at both the B3LYP/LanL2DZ and the MP2(Full)/6-31G(d) levels of theory. The optimised structures from both of the calculations were in good agreement with the experimental structure by Lide and Christensen.^[115] Relevant bond lengths and angles can be found in Table 3.3. While the bond lengths calculated with the B3LYP functional are slightly longer than experimental data, this is a known systematic error.^[15]

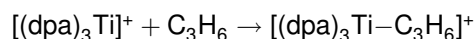
	Experimental ^[115]	B3LYP/LanL2DZ	Δ	MP2(Full)/6-31G(d)	Δ
C–C	1.501 ± 0.004	1.5123	0.011	1.4976	0.003
C=C	1.336 ± 0.004	1.3495	0.014	1.3366	0.001
C–C–C	124.3 ± 0.312	125.2819	1.0	124.5594	0.3

Table 3.3: Relevant bond lengths (Å) and angles (°) of C₃H₆ with absolute difference from experiment

The HOMO comprises a π orbital spanning the carbon-carbon double bond. This π orbital is often the basis of the Lewis basic, η^2 or L bonding moiety often used to discuss the initial binding step when propylene is bound to a Ziegler-Natta catalyst.

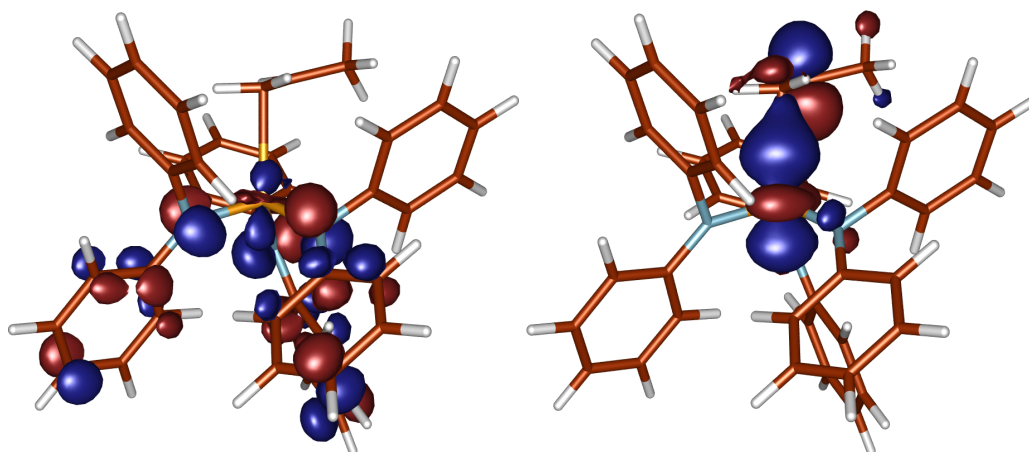
3.4 Structure of the [(dpa)₃Ti–C₃H₆]⁺ adduct, (2)

The calculated HOMO and LUMO for the product of the reaction

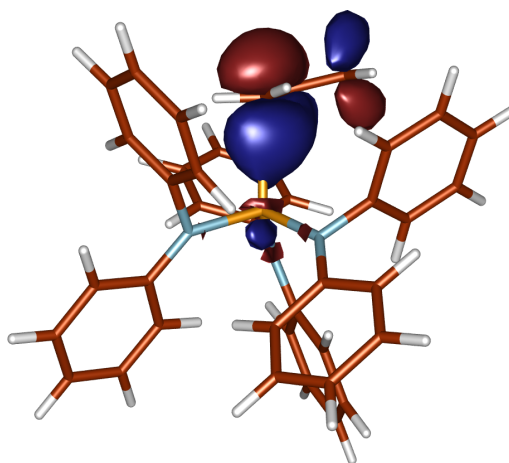


can be seen in Figure 3.6.

The bonding interaction between the propylene molecule and [(dpa)₃Ti]⁺ is found at HOMO-15, 3.14 eV below the HOMO, and is composed of the interaction between the d_{z^2} orbital on Ti and the π orbital on propylene. This interaction can be seen in Figure 3.7 and a portion of the molecular orbital diagram is found in Figure 3.8.

Figure 3.6: $[(\text{dpa})_3\text{Ti}-\text{C}_3\text{H}_6]^+$ HOMO and LUMO

Group	HOMO	LUMO
Ti	6.08	52.34
dpa-1	29.16	5.20
dpa-2	33.74	6.84
dpa-3	30.33	2.12
C_3H_6	0.69	33.50

Table 3.4: Orbital composition (%) of $[(\text{dpa})_3\text{Ti}-\text{C}_3\text{H}_6]^+$ Figure 3.7: $[(\text{dpa})_3\text{Ti}-\text{C}_3\text{H}_6]^+$ HOMO -15

Although an attempt was made to isolate a structure containing a true η^2 configuration or an agostic hydrogen, the structures quickly optimised to the asymmetric isomer shown in Figure 3.6. Furthermore, the $\text{Ti}-\alpha\text{C}-\text{H}$ angles are quite small, 88.24° and 93.70° , although due to the long $\text{Ti}-\alpha\text{C}$ bond the $\text{Ti}-\alpha\text{H}$ distances are quite long at 2.71 and 2.81 Å and upon inspection of the molecular orbitals no interaction was found.

The distance between the titanium centre and the previously interacting *ipso*-carbons of the ligands has elongated from 2.503 Å to an averaged value of 2.678 Å upon the coordination of the

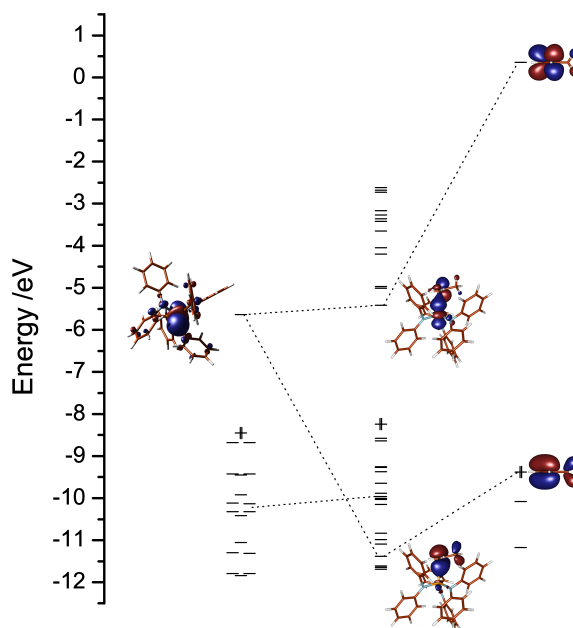


Figure 3.8: Molecular Orbital diagram for the formation of $[(\text{dpa})_3\text{Ti}-\text{C}_3\text{H}_6]^+$ from the reaction of **1** and propylene

propylene, while the previously non-interacting Ti–C distance contracted slightly from 3.125 Å in the cation to 3.117 Å in the bound species. This is due to the widening of the smaller Ti–N–*ipso*C angle from 96.62 ° in **1** to 104.94 ° in **2**. The set of E states previously seen to contain the Ti–*ipso*C interactions mix with a slightly energetically lower E set and are collectively destabilised with the addition of propylene.

Only small structural changes are observed in the propylene moiety upon binding. The $\alpha\text{C}-\beta\text{C}$ bond is elongated slightly to 1.367 Å in the bound species from 1.350 Å in free propylene while the $\beta\text{C}-\gamma\text{C}$ bond has contracted slightly from 1.512 Å in free propylene to 1.499 Å in the bound species. The $\beta\text{C}-\alpha\text{C}-\text{H}$ angles remain close to 120°. The calculated Ti– αC bond length is 2.52 Å while the Ti– βC distance is, 3.15 Å, approximately 20% longer, suggesting a decreased interaction.

Although the propylene binds asymmetrically the binding mode is through the populated π orbital where the majority of the electron density lies with a smaller contribution from the Ti d_{z^2} orbital. Therefore the molecular orbital retains its π -type symmetry suggesting a two electron, L type, donor. An analysis of the Mulliken charges shows a positive charge in **1** of 0.8912 |e| on the Ti metal centre, while in **2** the charge increases to 0.9755 |e|.

The average charge on each of the ligands decreases from 0.0363 |e| in **1** to -0.0960 |e| in **2**. The $^{\alpha}\text{C}$ shows a charge of -0.6224 |e| while the $^{\beta}\text{C}$ atom shows a charge of 0.1028 |e| suggesting Coulombic attraction between the titanium and $^{\alpha}\text{C}$ and Coulombic repulsion between titanium and $^{\beta}\text{C}$.

This observation, along with the existence of the low-lying LUMO which represents a further Ti– $^{\alpha}\text{C}$ interaction consisting of the overlap between the Ti d_{z^2} orbital and the π^* orbital of the olefin and the elongation of the $^{\alpha}\text{C}$ – $^{\beta}\text{C}$ bond, suggests some degree of back donation from the catalyst to the olefin. In the CBC method a back donation interaction is given the classification of Z and often when the degree of back donation is ambiguous, Z'.^[107]

In a 1994 study, Ahlrichs and co-workers^[89] were unable to locate a $[\text{Cp}_2\text{TiCH}_3\text{--C}_2\text{H}_4]^+$ π -complex at the MP2 or LDF levels of theory. Calculations at the SCF level found a minimum energy structure for the expected cation active species, the π -complex and the γ -agostic product as well as a transition state consisting of an asymmetrically bound ethylene moiety. However, when single point energies of the SCF optimised structures were calculated at the MP2 level, the π -complex was found to be higher in energy than the asymmetric transition state and upon optimisation at the MP2 and LDF levels a minimum on the potential energy surface could not be found.

Instead, a nearly flat potential energy surface followed by a dramatic drop in energy as the γ -agostic product is formed was observed when the insertion reaction was modelled by a series of selected points along a reaction coordinate composed of the distance between the methyl carbon of the original $[\text{Cp}_2\text{TiCH}_3]^+$ complex and one of the carbons of the incoming ethylene molecule which form a new bond during the insertion. At each fixed C–C distance the remainder of the molecule was allowed to relax.

Neither a true transition state nor a local minimum were located along this reaction coordinate, although the possibility of a local minimum at a higher level of theory or correlation was not ruled out.^[89]

Later studies by Ziegler have shown local minima structures with a similar elongated interaction to the one observed in **2**. For example, the calculated structures of $[\text{Cp}_2\text{ZrCH}_3\text{--C}_2\text{H}_4]^+$ ^[75] as well as $[\text{Cp}_2\text{Zr}(\text{CH}_3)(\text{CH}_2=\text{C}(\text{CH}_3)\text{CH}_2\text{CH}(\text{CH}_3)_2)]^+$ ^[108] seen in Figure 3.9

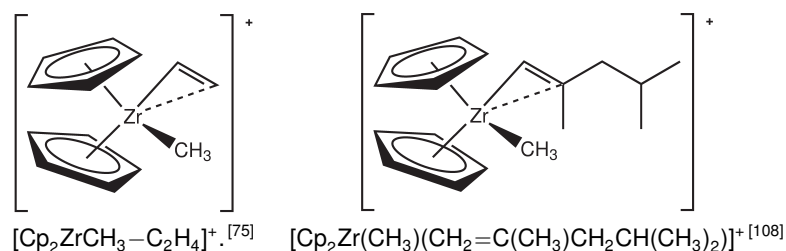


Figure 3.9: Asymmetric binding in calculated α -olefin complexes.^[75,108]

Each dpa ligand remains an LX ligand, retaining a trigonal planar geometry about the nitrogen atom, and the π interactions are only slightly destabilised from **1**. If the back donation is initially ignored, the CBC classification of **2** is ML_4X_3^+ .

The two formalisms for the transformation of a positively charged class to its equivalent neutral class are $\text{L}^+ \rightarrow \text{X}$ and $\text{X}^+ \rightarrow \text{Z}$.^[107] In this case, the $\text{X}^+ \rightarrow \text{Z}$ transformation is expected due to the apparent back donation to the olefin and therefore giving a neutral class of $\text{ML}_4\text{X}_2\text{Z}$. A further transformation of $\text{LZ} \rightarrow \text{X}_2$ is also made when a classification contains both an L and Z function.^[107] This reduces the equivalent neutral class to ML_3X_4 , a 14-electron species. The enthalpy of complexation was calculated as $\Delta H_c = -15.13 \text{ kJ mol}^{-1}$.

3.5 Intermediate complex

Several attempts were made to model the addition of the second propylene group. These initial attempts added the second propylene in a facial orientation above the $\alpha\text{C}-\beta\text{C}$ bond which can be seen in Figure 3.10. The HOMO of the newly added propylene is expected to overlap with the LUMO of **2** and therefore formally breaking the $\alpha\text{C}-\beta\text{C}$ double bond through donation into the π^* orbital as well as strengthening the $\text{Ti}-\alpha\text{C}$ bond. However, this was not seen and the distance between the two groups immediately increased.

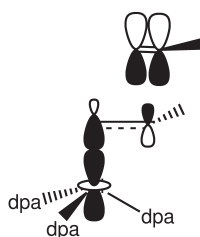


Figure 3.10: Facial addition

A further calculation was done that placed a formal C—C bond between α C of the new propylene molecule to the β C of **2** with an initial bond length of 1.5 Å. However, upon optimisation, the second propylene group detached within the first 10 iterations of the calculation. Obviously a new configuration was needed to model the reaction.

A new configuration, which placed the second propylene group in a position to donate electron density into the Ti—N π^* orbital from one of the ligand groups, was attempted.

This calculation optimised to a pseudo-six member ring analogous to the Zimmerman-Traxler transition state^[116] of the Ivanov and Reformatsky reactions. The ring is made up of the Ti metal centre as well as the nitrogen atom of one of the ligands, which was linked by the newly added propylene to the originally coordinated propylene. The structure of this complex can be seen in Figure 3.11. Carbon atoms shown in black make up the previously bound propyl group while those shown in blue belong to the added propylene molecule through the reaction seen in Figure 3.12.

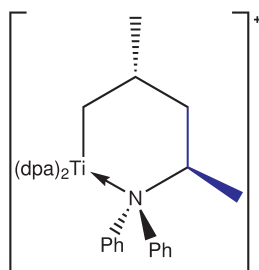


Figure 3.11: Illustration of the $[(dpa)_2Ti-C_2H_3(CH_3)C_2H_3(CH_3)dpa]^+$ species.

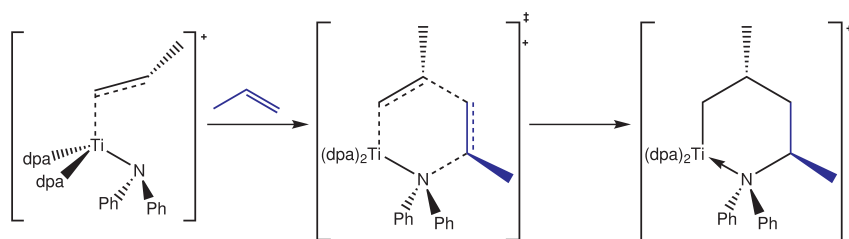


Figure 3.12: Reaction forming the $[(dpa)_2Ti-C_2H_3(CH_3)C_2H_3(CH_3)dpa]^+$ species.

After examination of this structure it became apparent that it was not the only possible form and was most likely not the lowest possible isomer available as the methyl group of the incoming propylene might be expected to add next to the methyl group of the originally coordinated propylene as opposed to next to the bulky ligand. A range of stereo and structural isomers of the cyclic intermediate are possible and the exact form of each isomer is dependent upon from which direction the incoming olefin approaches, as seen in Figure 3.13, the orientation of the incoming

propylene as well as the potential for re-arrangement of the adduct, **2**. These factors, culminating in several potential pathways, each giving rise to several possible isomers, are explicitly discussed in Chapter 4.

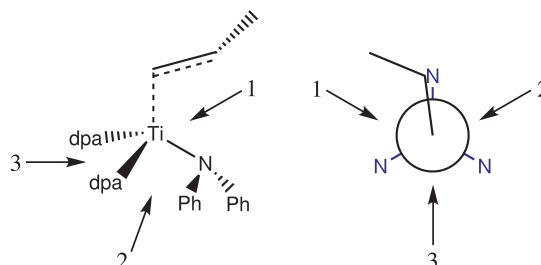


Figure 3.13: Possible directions of approach for the incoming olefin viewed from the side, left, and down the C–Ti vector, right.

3.5.1 Structure of $[(\text{dpa})_3\text{Ti}-\text{C}_6\text{H}_{12}]^+$ (**3**)

The lowest energy isomer, $[(\text{dpa})_2\text{Ti}-\text{CH}_2\text{CH}(\text{CH}_3)\text{CH}(\text{CH}_3)\text{CH}_2\text{N}(\text{C}_6\text{H}_5)_2]^+$ **3**, seen in Figure 3.14, was chosen as the model for the intermediate. It is very similar in structure to the one that was initially obtained but is nearly 30 kJ mol^{-1} lower in energy. The energy difference is attributed to the lack of 1,3 diaxial interactions, other than those with hydrogen, which can easily be seen when viewed in the chair conformation shown in Figure 3.14(b) where the red substituents represent diphenylamido ligands and the blue substituents are phenyl rings. The chair conformation originally obtained for the intermediate in Figure 3.11 contains a 1,3 diaxial interaction between a diphenylamido ligand and one of the methyl substituents as will be discussed in Chapter 4.

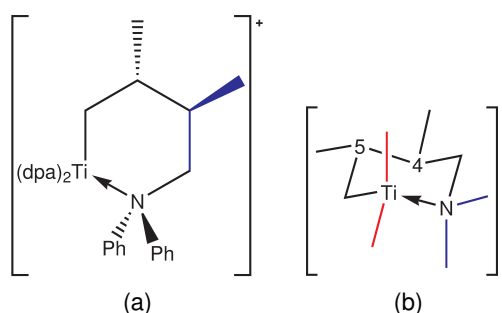


Figure 3.14: Schematic of the lowest energy isomer for the intermediate **3**

The calculated HOMO and LUMO of this intermediate complex **3** are shown in Figure 3.15.

The molecular orbital containing the bonding interaction between the titanium metal centre and the carbon atom of the ring is found at the HOMO-9 level, 1.32 eV lower than the HOMO with

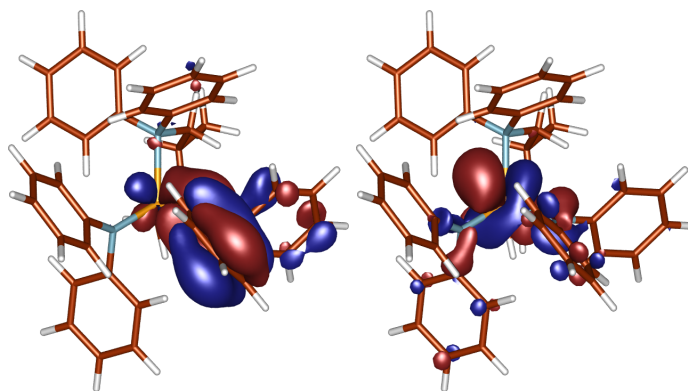


Figure 3.15: $[(\text{dpa})_3\text{Ti}-\text{C}_6\text{H}_{12}]^+$ HOMO and LUMO

an energy of -9.78 eV. This interaction is destabilised by 1.6 eV from the interaction in the adduct and is considerably shorter with the distance between the two atoms being 2.209 Å in **3** versus 2.519 Å in the adduct.

The higher energy metal *d* orbitals contribute a larger percentage to the molecular orbital containing the bonding interaction in **3** than in the adduct providing a possible explanation for the rise in energy. The overall contribution from the metal centre to the molecular orbital containing the interaction with the propylene moiety in the adduct **2** is only 10% with the propyl group contributing 78% of the total composition. In **3** the contribution from the metal increases to 22% with the same propyl group contributing 54% to the total molecular orbital.

The HOMO-12 orbital contains a dative N–Ti interaction and is -1.63 eV relative to the HOMO. It should be noted, however, that the electron density of the molecular orbital is spread out over the entirety of the dpa ligand and the close proximity of the nitrogen atom to the titanium centre may be enhanced due to an electrostatic or Coulombic attraction.^[117]

An analysis of the Mulliken charges reveal a positive 0.9311 |e| charge on the titanium while a charge of -0.5379 |e| is found on the nitrogen in question. The relative distance between the two atoms sees an increase of over 0.3 Å increasing from 1.900 Å in **2** to 2.209 Å in **3**. The remaining two Ti–N bonds show little change, although the distance to the axial nitrogen when the chair conformation is considered is slightly elongated, presumably due to the sterically unfavourable position.

The newly formed C–C bond is found at HOMO-15, 2.69 eV below the HOMO, while the new C–N bond lies lower in energy at the HOMO-18 level, 3.24 eV lower than the HOMO.

The intermediate complex has a CBC classification of ML_3X_3^+ or ML_2X_4 neutral class, the same

as the initial cation **1**; however, it now contains the classically necessary requirement of a metal-alkyl bond for insertion during polymerisation. The removal of the N–Ti interaction would afford an even more Lewis acidic ML_2X_3^+ or MLX_4 naked cation and would allow for a vacant site for the addition of another monomer.

3.6 Structure of $[(\text{dpa})_2\text{Ti}(\text{C}_6\text{H}_{12}\text{N}(\text{C}_6\text{H}_5)_2)-\text{C}_3\text{H}_6]^+$ (**4**)

A transition state or high energy intermediate consisting of the broken N–Ti interaction was not isolated; however, the resulting adduct, $[(\text{dpa})_2\text{Ti}(\text{C}_6\text{H}_{12}\text{N}(\text{C}_6\text{H}_5)_2)-\text{C}_3\text{H}_6]^+$ (**4**), for the addition of a third propylene moiety was examined and is shown in Figure 3.16. The HOMO and LUMO can be found in Figure 3.17 with the LUMO strongly resembling that of the originally obtained adduct, **2**.

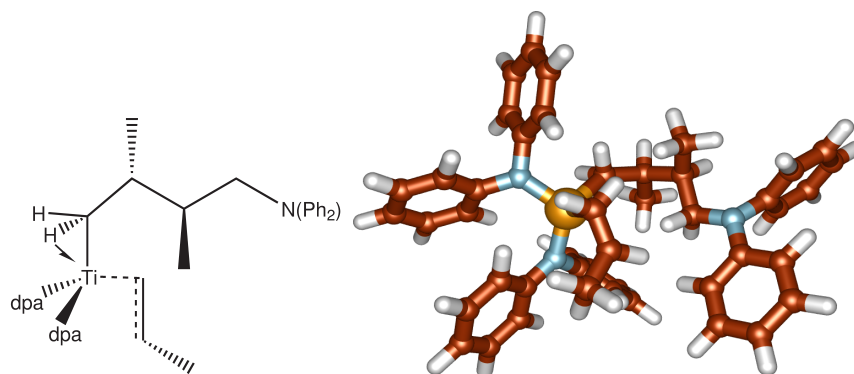


Figure 3.16: $[(\text{dpa})_2\text{Ti}(\text{C}_6\text{H}_{12}\text{N}(\text{C}_6\text{H}_5)_2)-\text{C}_3\text{H}_6]^+$ **4**

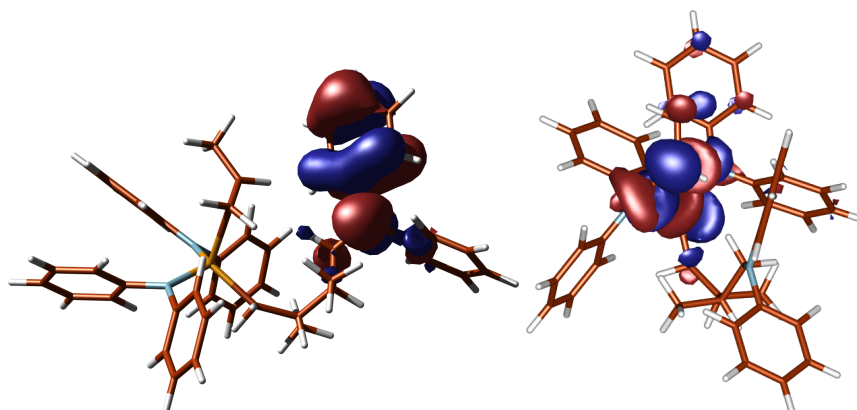


Figure 3.17: $[(\text{dpa})_2\text{Ti}(\text{C}_6\text{H}_{12}\text{N}(\text{C}_6\text{H}_5)_2)-\text{C}_3\text{H}_6]^+$ HOMO and LUMO

The observed $\text{Ti}-\text{C}_R-\text{C}$ bond angle, where C_R represents the αC of the alkyl group, is considerably large having a value of 144.86° , while the corresponding $\text{Ti}-\text{C}_R-\text{H}$ angles are quite acute

(90.24° and 94.89°) which is consistent with the α -agostic hydrogen assisted Green-Rooney mechanism. The relevant bond lengths and angles with a comparison to those found in **3** can be found in Table 3.5.

While the $\text{Ti}-\alpha\text{H}$ distance is longer than might be expected for an agostic interaction, a portion of the electron density of the HOMO-7 orbital, shown in Figure 3.18, presents as a p orbital on C_R forming a σ bond with one of its hydrogen atoms and donating to an available titanium d orbital thus forming a weak α -agostic interaction. The molecular orbital containing the $\text{Ti}-\text{C}_R$ bond is 0.09 eV lower in energy and is found within the HOMO-9 orbital.

	3	4	Δ (4 - 3)
$\text{Ti}-\text{C}_R-\text{C}$	121.41	144.86	23.45
$\text{Ti}-\text{C}_R-\text{H}_{(1)}$	102.63	90.24	-12.39
$\text{Ti}-\text{C}_R-\text{H}_{(2)}$	105.49	94.89	-11.25
$\text{Ti}-\text{C}_R$	2.063	2.050	-0.013
$\text{Ti}-\text{H}_{(1)}$	2.545	2.340	-0.205
$\text{Ti}-\text{H}_{(2)}$	2.586	2.412	-0.171

Table 3.5: Bond distances (Å) and angles (°) of **3** and **4**

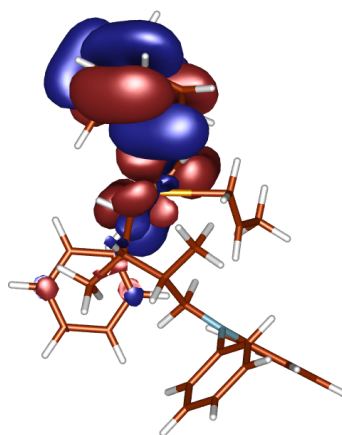


Figure 3.18: Weak α -agostic interaction of **4**, HOMO-7

Bonding interaction between the metal centre and the bound propylene is very similar to that found in the initial adduct, **2**, consisting of the d_{z^2} orbital on titanium and the π orbital on propylene and lies at the HOMO-21 level, 4.20 eV lower than the HOMO and is shown in Figure 3.19. The $\text{Ti}-\alpha\text{C}_{\text{C}_3\text{H}_6}$ bond is shorter in **4** than in **2** by 0.109 Å with values of 2.410 Å and 2.519 Å, respectively. The $\alpha\text{C}-\beta\text{C}$ bond of the propylene moiety is again elongated relative to that found for free propylene.

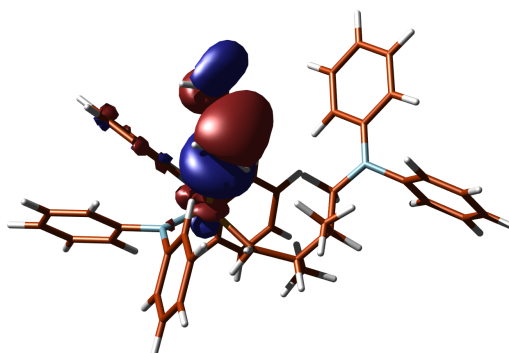


Figure 3.19: Ti– α C₃H₅ interaction in **4**, HOMO -21

3.7 Chain Termination

Although chain termination reactions were not specifically calculated, two of the most common chain termination processes are β -hydride elimination and chain transfer. β -hydride elimination seems unlikely due to the extreme electron deficiency of the species involved as well as the experimentally observed instability of the (dpa)₃TiH complex.^[62] Chain transfer might be more likely; however, the experimental results in Section 2.4 and Figure 2.16 are most likely due to the depletion of monomer as some reactions were able to be restarted with the addition of a further aliquot of propylene.^[62]

3.8 Structure of (dpa)₃TiCH₃ (**5**)

The electronic structure of the (dpa)₃TiCH₃ precursor, **5**, was also investigated. Even though the (dpa)₃TiCH₃ complex contains a d^0 metal centre, the conventionally necessary metal-alkyl bond and has the same ML₃X₄ CBC classification as the [Cp₂ZrCH₃]⁺ archetype for polymerisation, it does not upon first inspection appear to have an available vacant site for the addition of monomer. While a mechanism where the geometry about the titanium centre changes from pseudo-tetrahedral to trigonal bipyramidal can be envisioned, it has been shown that in experimental studies **5** does not polymerise propylene upon its own accord. Polymerisation does however occur when in the presence of the Lewis acidic co-catalyst *tris*-pentafluorophenyl borane, B(C₆F₅)₃.^[62]

The symmetry is similar to the [(dpa)₃Ti]⁺ system with the highest available point group being C_{3v} . Again, no symmetry constraints were imposed in the calculation and the minimum energy

structure found in Figure 3.20 is of C_1 symmetry.

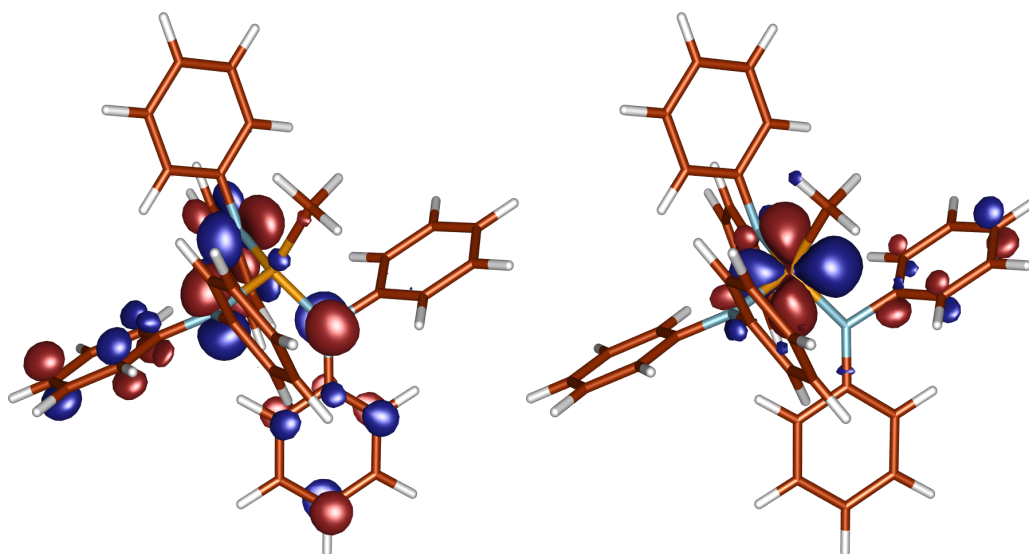


Figure 3.20: $(\text{dpa})_3\text{TiCH}_3$ HOMO and LUMO

Group	HOMO	LUMO
Ti	1.67	66.16
dpa-1	32.64	8.97
dpa-2	31.28	10.15
dpa-3	32.30	13.27
CH ₃	2.10	1.46

Table 3.6: Orbital composition (%) of $(\text{dpa})_3\text{TiCH}_3$

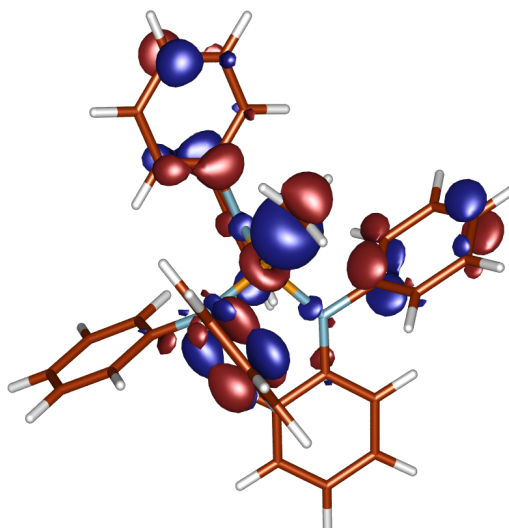
The orbital containing the bonding interaction of the methyl group is composed mostly of a metal d_{z^2} and a p_z orbital based on the carbon atom of the methyl group. The molecular orbital containing this interaction also consists of electron density on the three phenyl rings that lie on the same side of the molecule as the methyl group.

The interaction is found at the HOMO-3 level and has an energy value -6.69 eV which is considerably less stabilised than the titanium-propyl interaction found in **2** which lies at -11.79 eV; however, this energy difference is in part due to the positive charge on **2** as the contact ion pair was not calculated. A visualization of the orbital can be found in Figure 3.21.

3.8.1 Analogous system: $(\text{dsa})_3\text{TiCH}_3$

The crystal structure of *tris(bis[(trimethyl-silyl)]amido)titanium methyl* ($(\text{dsa})_3\text{TiCH}_3$) is known.^[118]

The structure has been calculated at the B3LYP/LanL2DZ level for comparison. The starting point

Figure 3.21: (dpa)₃TiCH₃ HOMO-3

for the optimisation was taken from the crystallographic coordinates found on the CSD.^[111,112] Key bond lengths and angles for the experimental and calculated structures of (dsa)₃TiCH₃ as well as the corresponding information of the calculated structure of **5** can be seen in Table 3.7.

	(dsa) ₃ TiCH ₃ Experimental ^[118]	(dsa) ₃ TiCH ₃ Calculated	Δ^a	(dpa) ₃ TiCH ₃ Calculated
Ti–C	2.127	2.106	-0.021	2.078
Ti–N	1.935	1.942	0.007	1.933
C–Ti–N	102.30	101.74	-0.56	108.67
Ti–N–R ^{b,c}	118.06	117.76	-0.30	107.74
Ti–N–R ^{b,d}	126.60	126.11	-0.49	134.75
N–Ti–N	115.59	115.97	0.38	110.26

^a Calculated - Experimental

^b R = Si, C

^c R above N₃ plane

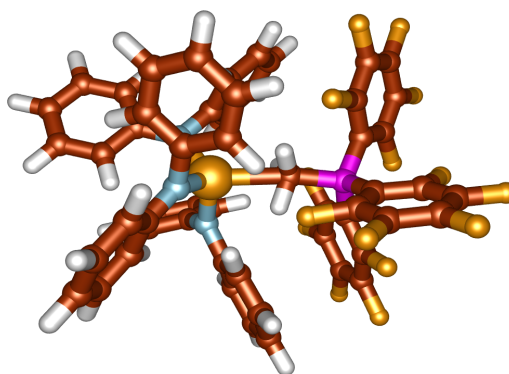
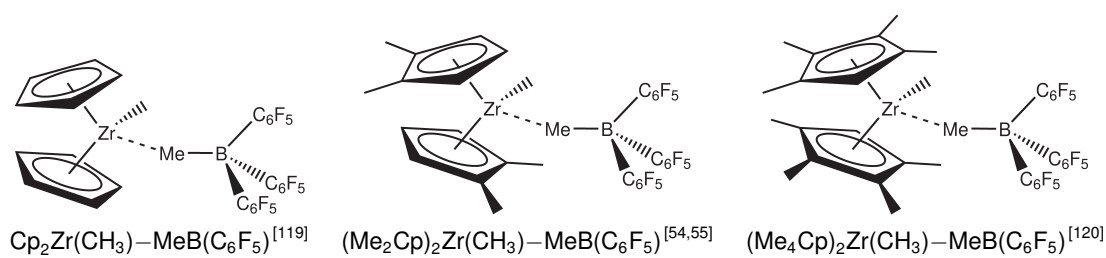
^d R below N₃ plane

Table 3.7: Average bond lengths (Å) and angles (°) of (dsa)₃TiCH₃ and (dpa)₃TiCH₃

3.9 Structure of (dpa)₃Ti–CH₃–B(C₆F₅)₃ (**6**)

The calculated structure of (dpa)₃Ti–CH₃–B(C₆F₅)₃, **6**, is shown in Figure 3.22. The structure is in good agreement with known crystal structures of Cp₂Zr(CH₃)–CH₃–B(C₆F₅)₃ and its derivatives shown in Figure 3.23.

Each of the Cp₂Zr(CH₃)–CH₃–B(C₆F₅)₃ type structures displays a non-linear Zr–C–B bridging angle and typical C–B bond lengths, the values of which can be seen in Table 3.8 along with

Figure 3.22: $(\text{dpa})_3\text{TiCH}_3\text{--CH}_3\text{--B}(\text{C}_6\text{F}_5)_3$, **6**Figure 3.23: Known crystal structures of $\text{Cp}_2\text{Zr}(\text{CH}_3)\text{--CH}_3\text{--B}(\text{C}_6\text{F}_5)_3$ and its derivatives

those calculated for **6**.

	M–C–B / °	C–B / Å	M–CH ₃ / Å	M–μ–CH ₃ / Å	ΔM–C ^a / Å
$\text{Cp}_2\text{Zr}(\text{CH}_3)\text{--MeB}(\text{C}_6\text{F}_5)_3^{[119]}$	169.10	1.667	2.251	2.556	0.305
$(\text{Me}_2\text{Cp})_2\text{Zr}(\text{CH}_3)\text{--MeB}(\text{C}_6\text{F}_5)_3^{[54,55]}$	161.838	1.663	2.252	2.549	0.297
$(\text{Me}_4\text{Cp})_2\text{Zr}(\text{CH}_3)\text{--MeB}(\text{C}_6\text{F}_5)_3^{[120]}$	174.02	1.667	2.242	2.601	0.359
6 (Calculated)	170.60	1.699	2.078 ^b	2.444	0.366

^a Difference in the bond lengths for bridging and terminal methyl groups

^b Calculated bond distance from complex **5**

Table 3.8: Structural data for $\text{Cp}_2\text{Zr}(\text{CH}_3)\text{--CH}_3\text{--B}(\text{C}_6\text{F}_5)_3$ derivatives and calculated **6**

The Ti–C distance is 2.444 Å, which is longer than those seen for known crystal structures^[111,112] containing a $\text{Ti--}\mu\text{--CH}_3\text{--B}(\text{C}_6\text{F}_5)_3$ entity, the median being 2.37 Å with the longest being 2.42 Å;^[121] however, the elongation is in reasonable agreement with those found for the $\text{Cp}_2\text{Zr}(\text{CH}_3)\text{--CH}_3\text{--B}(\text{C}_6\text{F}_5)_3$ type structures illustrated in Table 3.8. The bridging methyl is close to a trigonal-bipyramidal geometry with the carbon atom being only 0.519 Å out of the H_3 plane and closer to the $\text{B}(\text{C}_6\text{F}_5)_3$ moiety.

The structure of **6** is expected to contain a 3-centre-2-electron bond encompassing the boron and methyl carbon atoms as well as the titanium centre. This type of interaction is found at HOMO-21, 2.86 eV below the HOMO, and can be seen in Figure 3.24.

In agreement with the elongated Ti–C distance, the calculated enthalpy of ion pair separa-

tion for **6** was found to be 221.05 kJ mol⁻¹, which is lower than the gas phase calculations by Ziegler^[94] of [(NPR₃)₂TiCH₃]⁺[B(C₆F₅)₄]⁻, 245.77 kJ mol⁻¹, and considerably less than those found for systems where H₃CB(C₆F₅)₃⁻ was the anion, for example 305.64 kJ mol⁻¹ for the bridging [(NPR₃)₂TiCH₃]⁺[H₃CB(C₆F₅)₃]⁻ complex where R=CH₃. The enthalpy of ion pair formation was also notably small. Both of these suggest that the H₃CB(C₆F₅)₃⁻ anion should be easily removed to form the cationic species **1** which is consistent with the experimental observation of polymerisation.

While not meeting the expected structural requirement of containing a metal-alkyl bond and having a more electron deficient metal centre than the $[\text{Cp}_2\text{ZrCH}_3]^+$ type catalysts used for conventional Ziegler-Natta catalysis, $[(\text{dpa})_3\text{Ti}]^+$ (**1**) has been shown experimentally to polymerise propylene.

The calculated structure of the expected methyl bridging complex, $(\text{dpa})_3\text{Ti}-\text{CH}_3-\text{B}(\text{C}_6\text{F}_5)_3$ (**6**), shows an appreciable increase in the Ti–C bond distance over that found in **5** consistent with

a weakly coordinated contact ion pair and suggests the formation of the cationic species **1**.

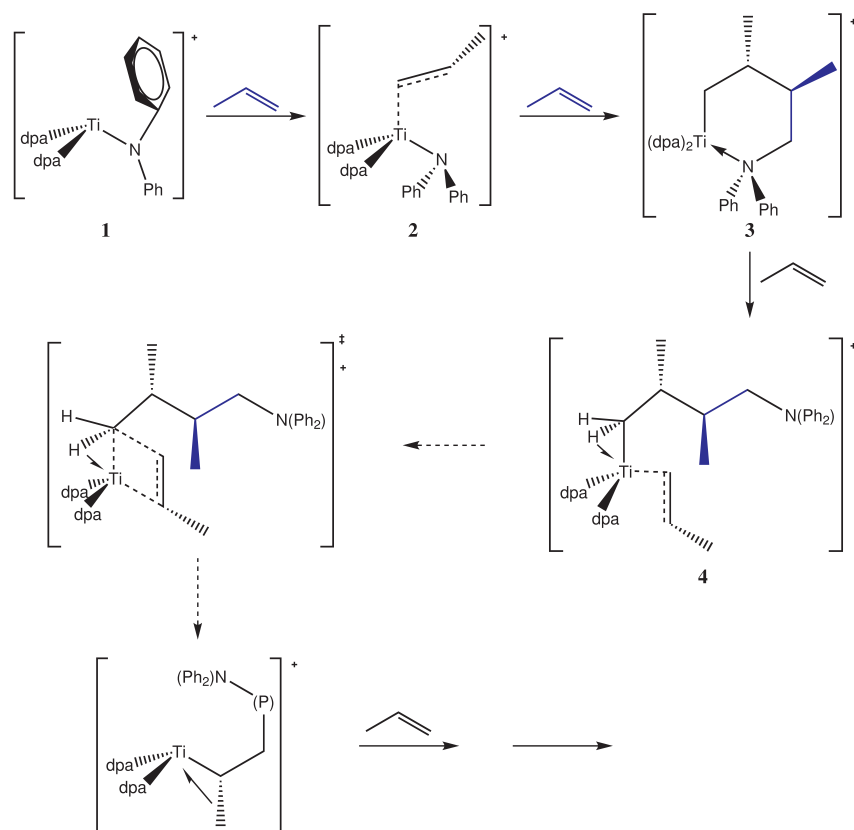


Figure 3.25: Expected mechanism for the polymerisation of propylene at **1**

The adduct of propylene with **1**, $[(dppe)_3Ti-C_3H_6]^+$ (**2**), and other selected species were calculated to elucidate the mechanism of this unconventional, yet catalytically active complex. An unusual intermediate, **3**, was found to form when a second propylene group was calculated with the adduct forming a pseudo six-membered ring containing both the titanium centre and the nitrogen of one of the ligands formally breaking the Ti–N covalent bond and replacing it with a dative bond from the nitrogen lone pair to the electron deficient metal centre.

When a third propylene was added to model the continued propagation of the polymerisation reaction, a similar adduct to that found for the first addition was found although one of the amido ligands has now been replaced with an alkyl group thus giving the expected structural requirements of conventional Ziegler-Natta catalysis although with an unconventional, more Lewis acidic metal centre. The continued insertion and propagation steps are expected to conform to the generally accepted modified Green-Rooney mechanism as outlined above where (P) in the last structure denotes the growing polymer chain.

An experimental check of this mechanism could be done through the use of Nuclear Magnetic

Resonance Spectroscopy, Mass Spectrometry and Gel Permeation Chromatography to identify the group at the end of the polymer chain, tacticity as well as other physical properties of the resultant polymer.

Chapter 4

The hetero-metallo cyclo intermediate

4.1 Introduction

A variety of reactions throughout organometallic chemistry are generally accepted to progress through metallocycle intermediates or transition states. One example is the Zimmerman-Traxler transition state model^[116] for the Ivanov and Reformatski reactions within organic synthesis where the metallocycle is used to explain the stereo-selectivity of the reaction. One example of the Ivanov reaction including the proposed hetero-metallo cyclo transition state as suggested by Zimmerman and Traxler^[116] is shown in Figure 4.1.

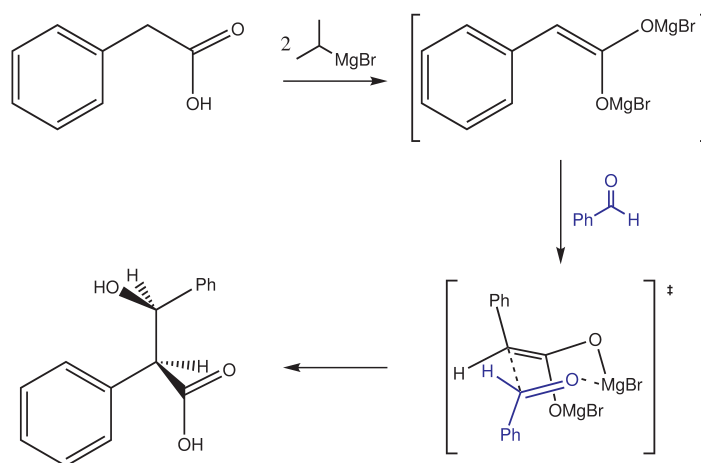


Figure 4.1: The Ivanov reaction

As explored in Chapter 3, the mechanism for the polymerisation of propylene by *tris*-amido titanium catalysts is also expected to progress through a hetero-metallo-cyclic intermediate as a pathway for facial addition, seen in Figure 3.10, of a second propylene group to the adduct was not found.

A large number of stereo and structural isomers of the intermediate are available and include both five and six-membered rings. The exact form of each isomer will depend upon the direction in which the incoming propylene approaches the catalyst as well as the orientation of the incoming propylene.

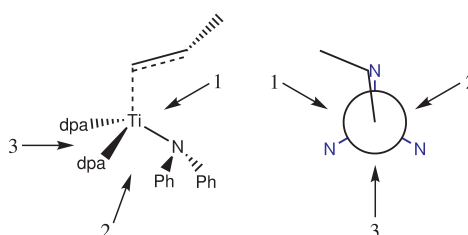


Figure 4.2: Possible directions of approach for the incoming olefin viewed from the side, left, and down the C—Ti vector, right.

If the propylene molecule approaches from directions 1 or 2 as seen in Figure 4.2 a six-membered ring is expected, while if the propylene approaches from the direction labelled 3 a five-membered ring would result. Several potential forms of the possible intermediates and their thermodynamic likelihood will be considered here.

4.1.1 Labelling scheme

Due to the considerable complexity exhibited by the fact that the structures presented in this chapter are so closely related, the following labelling system has been used. Each structure containing a six-membered ring has been given a label of the form **X**-Y_{pC}-Z_{pC} where **X** corresponds to the particular pathway, for example **A**, **B**, etc. Y and Z refer to the atom positions in which the first and second methyl substituents can be found according to the numbering system shown, for example, in Figure 4.3.

In all cases atom 1 is the titanium centre, atom 2 is nitrogen and so on. *p* denotes the position, either *a* for axial or *e* for equatorial of the substituent within the specific chair conformation and *C* is the chirality of the stereocentre, either *R* (*Rectus*) or *S* (*Sinister*) in accordance with Cahn-

Ingold-Prelog priority rules.^[122,123]

Structures containing five-membered rings are considered in Pathways **C** and **D** and the labelling system is necessarily altered. Labels of the form $\mathbf{X}_W\text{-Y}_{pC}\text{-Z}_{pC}$ are used. Where the subscript W denotes the number of the apex atom which lies above the plane in the pseudo-envelope conformation. Also, the notation for p is changed to u for substituents above the plane and d for those below. In each case Z is C_5 and has an ethyl substituent.

Labels of the form $\mathbf{X}\text{-}CC$ have been used when referring to a set of conformers belonging to the same isomer or their associated equilibrium. In each case \mathbf{X} is the pathway for the formation and CC denotes the chirality of atoms Y and Z , respectively.

Diagrams of the relevant structures along with their labels are given at the beginning of each pathway. However, only the skeleton of the pseudo-chair and envelope conformations are shown as labels of the substituents on titanium and nitrogen have been excluded, exhibiting only their relative positions. In order to easily distinguish the substituents a colour scheme has been employed where substituents shown in black are methyls, or ethyl on C_5 for Pathways **C** and **D**, while those in red signify the two remaining diphenylamido ligands on titanium and those in blue are the phenyl rings associated with the diphenylamido ligand which has been incorporated into the ring. In the cases where equilibria between two chair conformations are shown, 1,3 diaxial interactions are outlined in green by hashed lines.

4.2 Possible pathways involving pseudo-4 + 2 cycloaddition

When the initial calculation converged to a pseudo six-membered ring, it was apparent that the isomer found ($\mathbf{B}\text{-}3_{eR}\text{-}5_{aR}$) was not the only possible one, nor was it likely to be the lowest energy isomer available as other isomers can be drawn that do not contain 1,3 diaxial interactions between the substituents. This prompted an investigation of further isomers.

The intermediate was formed through a pseudo 4 + 2 cycloaddition and is dependent on the position of the incoming propylene molecule. A generalised reaction can be seen in Figure 4.3 where only the alkene portion of the incoming monomer is shown in the expected intermediate. Carbon atoms shown in black make up the previously bound propyl group while those shown in blue belong to the incoming group. The second methyl substituent, changing the incoming

fragment from ethylene to propylene, can be on either carbon 3 (C_3) or carbon 4 (C_4) and will depend on its relative position when approaching the catalyst.

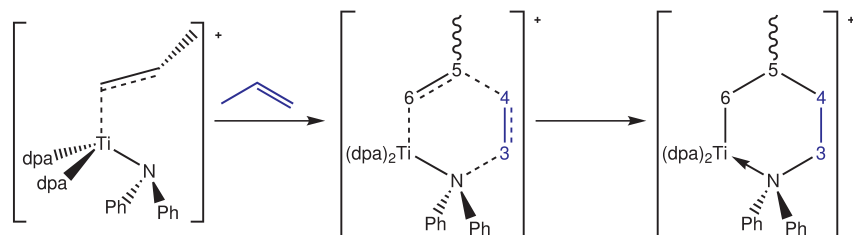


Figure 4.3: pseudo-4 + 2 cycloaddition

The methyl groups on C_5 , as well as the one on C_3/C_4 are stereospecific giving two chiral centres and therefore four possible stereo-isomers, namely *RR*, *RS*, *SS* and *SR*. In addition, each stereo-isomer has two possible chair conformations which are expected to differ in energy. This leads to a total of 16 possible structures. Fortunately, the problem is greatly simplified due to the fact that a large number of enantiomeric sets are included within these potential conformations making several of the structures energetically degenerate, *vide infra*.

For each case, the *RR* and *SS* configurations make up a set of enantiomers. This is also true for the *RS/SR* sets, and results in a total of eight energetically distinct sets out of the possible 16 structures. Figure 4.4 shows an example enantiomeric set where the second methyl group is on C_4 . The set is comprised of the **A-*RR*** and **A-*SS*** stereo-isomers. The horizontal line represents a mirror plane that is parallel to the plane formed by Ti, N, C_4 and C_5 which is outlined by dashed lines.

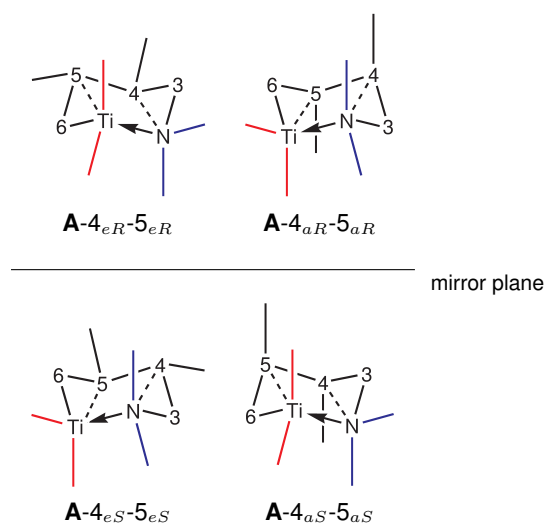


Figure 4.4: Enantiomeric structures of the **A-*RR***/**A-*SS*** sets

All sixteen possible structures were calculated and, as expected, the enantiomeric pairs were indeed found to be energetically degenerate. The eight enantiomeric sets are discussed below where the RR and SR stereo-isomers have been considered. Although the titanium, nitrogen, and carbon atoms C₄ and C₅ do not sit in a perfect plane, the torsional distortion of the plane is less than 6° in each case.

For monosubstituted cyclohexanes, the energy is lower if the substituent is in the equatorial position rather than in the axial position. This is because, if the substituent is on C₁, it is then gauche to C₃ as well as C₅ with a torsional angle of approximately 60° when in the axial position. If the substituent is in the equatorial position, it is anti-periplanar to both C₃ and C₅ with a torsional angle of approximately 180°. This is illustrated in Figure 4.5 where the point of view for the Newman projection is the C₁–C₂ vector and the relative position to C₃ is shown. The Newman projection for the C₁–C₆ vector will show the relationship between the substituent and C₅.

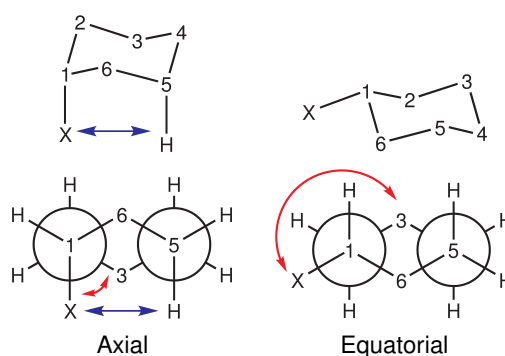


Figure 4.5: Axial vs. equatorial position

For monosubstituted cyclohexane, the energetic difference between the axial and equatorial positions for a methyl substituent has been experimentally shown to be 7.3 kJ mol⁻¹,^[124] while for a phenyl ring the difference is 11.3 kJ mol⁻¹^[125] and for aminocyclohexane where the substituent is NH₂, 5.9 kJ mol⁻¹.^[126]

For multi-substituted cyclohexanes, 1,3 diaxial interactions often further expand the energy difference of the two chair conformers. 1,3 diaxial interactions are the result of steric interference between two or more axial substituents. Although they are present for monosubstituted species as illustrated by the blue arrows in Figure 4.5, the greater energetic difference in multi-substituted species is due to increased steric hindrance when a hydrogen substituent is replaced with a bulkier group.^[127,128]

For most of the chair equilibria in this chapter, 1,3 diaxial interactions can be used to distinguish which conformation is expected to be lower in energy. Both the titanium and nitrogen atoms have two substituents meaning that each will have both an equatorial as well as an axial substituent and the placement of the methyl groups will therefore dictate energetics of the isomer.

4.2.1 Pathway A

A generalised representation of Pathway **A** is seen in Figure 4.6 and is used to depict the formation of **A-RR** and **A-SR**, where the two methyl substituents are located on C₄ and C₅.

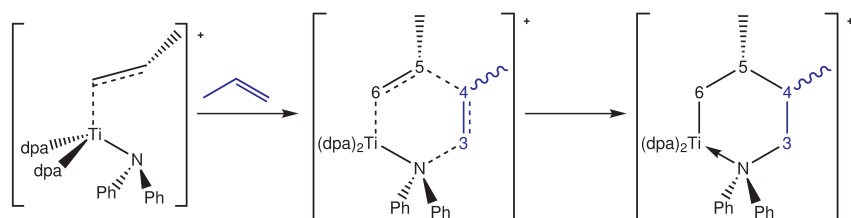


Figure 4.6: Pathway **A**

The four chair conformations available for **A-RR** and **A-SR**, along with their labels are given in Figure 4.7. Table 4.1 lists relevant bond lengths and angles as well as distances between non-bonded atoms having substituents with the potential of engaging in 1,3-diaxial interactions, i.e. Ti—C₅ and N—C₄.

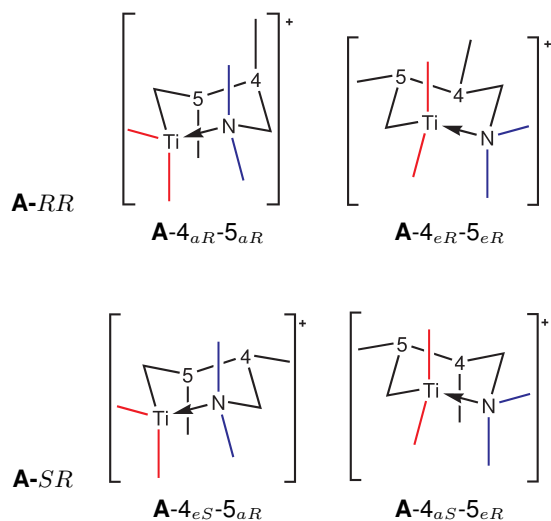
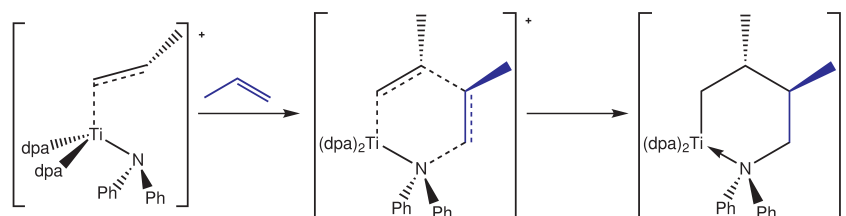
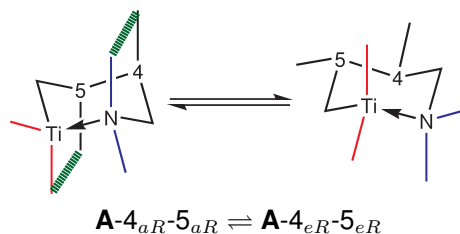


Figure 4.7: Possible chair conformations of **A-RR** and **A-SR**

A-RR			A-SR		
	A-4_{aR}-5_{aR}	A-4_{eR}-5_{eR}		A-4_{eS}-5_{aR}	A-4_{aS}-5_{eR}
Ti—N / Å	2.233	2.209	Ti—N / Å	2.230	2.230
C ₆ —Ti / Å	2.061	2.063	C ₆ —Ti / Å	2.066	2.066
Ti—C ₅ / Å	3.223	3.161	Ti—C ₅ / Å	3.214	3.125
N—C ₄ / Å	2.690	2.624	N—C ₄ / Å	2.613	2.681
Ti—N—C ₄ —C ₅ / °	0.854	2.261	Ti—N—C ₄ —C ₅ / °	-5.772	4.713

Table 4.1: Relevant structural data for **A-RR** and **A-SR****A-RR**

The reaction for the formation of the **A-RR** intermediate is shown in Figure 4.8. Two chair conformations are available for the pseudo six-membered ring and the associated equilibrium of the two conformers can be seen in Figure 4.9

Figure 4.8: Pathway for the formation of **A-RR**Figure 4.9: Equilibrium of the two chair conformations of **A-RR**

The equilibrium shown in Figure 4.9 lies far to the right due to the steric strain caused by 1,3 di-axial interactions, which force the equilibrium toward the less strained conformation. Substituent-substituent di-axial interactions within complex **A-4_{aR}-5_{aR}** exist between the axial phenyl ring on the nitrogen and the methyl group on C₄ as well as the axial diphenylamido ligand on titanium and the methyl found on C₅. Due to these interactions, Ti—C₅ distance in **A-4_{aR}-5_{aR}** is larger than that found in **A-4_{eR}-5_{eR}** by 0.062 Å and the N—C₄ distance is longer by 0.066 Å. In the interaction between the methyl on C₅ and the diphenylamido ligand, the methyl group interacts with one of the phenyl rings of the bulky ligand, not the nitrogen atom. This interaction is similar to that seen between the methyl group on C₄ and the axial phenyl ring of the nitrogen within the

ring.

The equilibrium constant is calculated to be 3.53×10^8 and $\Delta H_{eq} = -47.28 \text{ kJ mol}^{-1}$. Complex **A-4_{eR}-5_{eR}** is lower on the potential energy surface than **A-4_{aR}-5_{aR}** by $47.75 \text{ kJ mol}^{-1}$ and is the lowest energy isomer of all those calculated for any pathway in this chapter. It was therefore chosen as the model for the intermediate in Chapter 2.

A-SR

The reaction for the formation of the **A-SR** isomer of the intermediate is shown in Figure 4.10. The two chair conformations that are available for the pseudo six-membered ring and the associated equilibrium of the two conformers can be seen in Figure 4.11

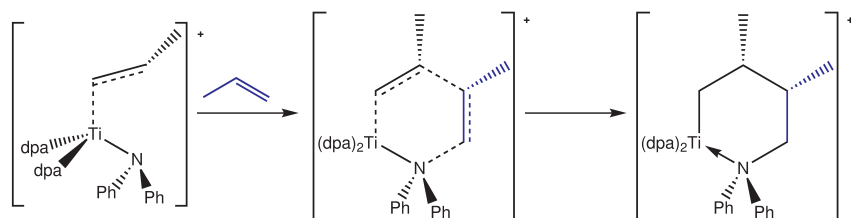


Figure 4.10: Pathway for the formation of **A-SR**

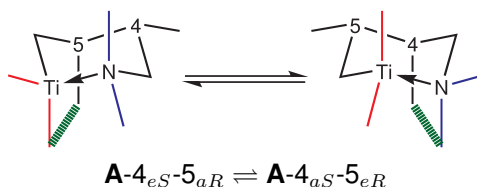


Figure 4.11: Equilibrium of the two chair conformations of **A-SR**

Both conformations were calculated and are found to have nearly equivalent energies with $\Delta E < 1 \text{ kJ mol}^{-1}$. As in complex **A-4_{aR}-5_{aR}** discussed above, the interaction between the methyl on C₅ and one of the phenyl rings on the axial diphenylamido ligand in **A-4_{eS}-5_{aR}** is essentially the same as the interaction between the methyl on C₄ and the axial phenyl ring of the nitrogen included in the ring of **A-4_{aS}-5_{eR}** thus explaining the negligible energy difference. As expected, the equilibrium constant is close to zero with a value of 3.12×10^{-1} . The **A-SR** set sits approximately 23 kJ mol^{-1} higher on the potential energy surface than **A-4_{eR}-5_{eR}**.

The mechanism for the interconversion between two chair conformations goes through a half-chair transition state, a twist-boat reactive intermediate and a boat transition state before pro-

gressing through a second twist-boat reactive intermediate and half-chair transition state to give the second chair conformation.^[127,128] The qualitative potential energy surface for this interconversion between two unsubstituted cyclohexane chairs can be seen in Figure 4.12. Both of the twist-boat conformations for the **A-SR** set were found and are approximately 4 kJ mol⁻¹ higher in energy than the chair conformations; however the half-chair and boat transition states were unable to be located in order to determine the rate of conversion.

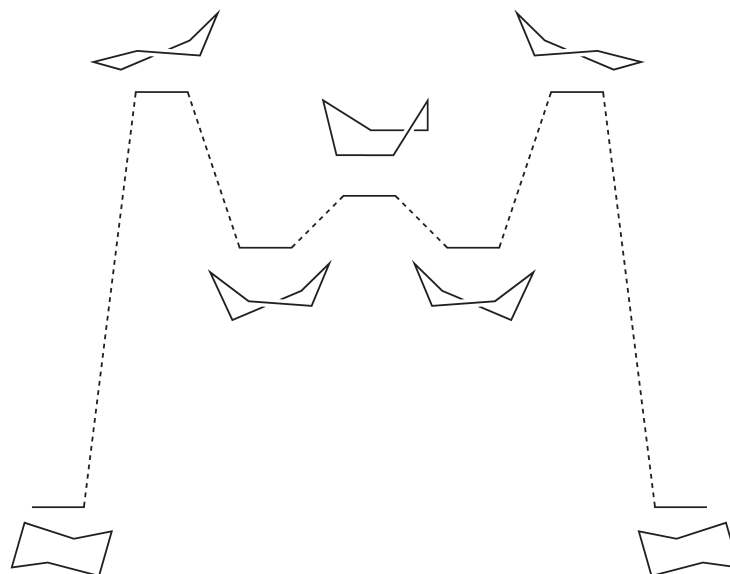


Figure 4.12: Qualitative potential energy surface for the interconversion between two chair conformations

4.2.2 Pathway B

In Pathway **B** the methyl substituent belonging to the incoming propylene is on C₃, *meta* to the titanium and *ortho* to the nitrogen atom. As the two methyl substituents lie on C₃ and C₅ both have the potential for 1,3 diaxial interactions with the diphenylamido ligands of the titanium metal centre as well as with each other while no such interaction is possible with the phenyl ring substituents of the nitrogen atom. A generalised reaction can be found in Figure 4.13 and the four conformations discussed in this section are shown in Figure 4.14 followed by relevant structural data in Table 4.2.

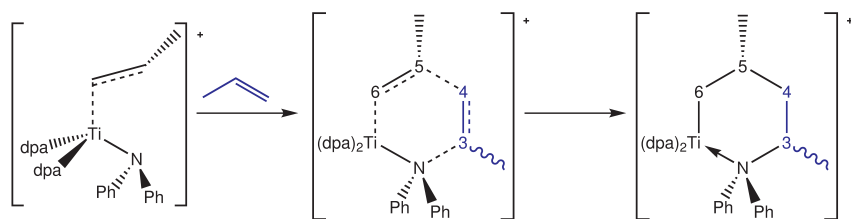
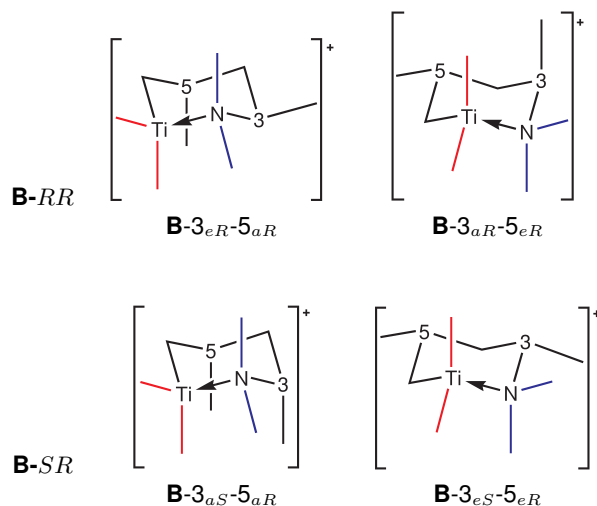


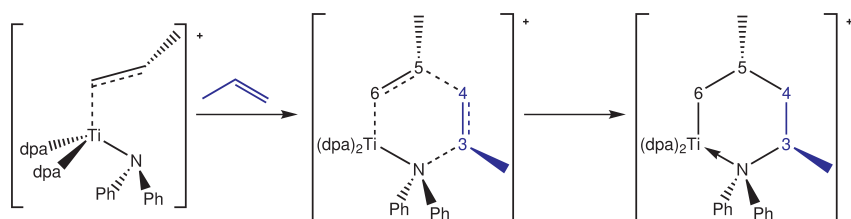
Figure 4.13: Pathway B

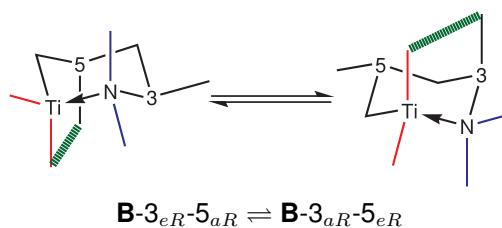
Figure 4.14: Possible chair conformations of **B-RR** and **B-SR**

	B-RR			B-SR	
	B-3_{eR}-5_{aR}	B-3_{aR}-5_{eR}		B-3_{aS}-5_{aR}	B-3_{eS}-5_{eR}
Ti—N	2.254	2.292	Ti—N	2.272	2.242
C ₆ —Ti	2.071	2.061	C ₆ —Ti	2.068	2.066
Ti—C ₃	3.088	3.198	Ti—C ₃	3.087	3.101
Ti—C ₅	3.137	3.155	Ti—C ₅	3.247	3.114
Ti—N—C ₄ —C ₅	-4.605	5.245	Ti—N—C ₄ —C ₅	4.032	5.515

Table 4.2: Relevant structural data for **B-RR** and **B-SR****B-RR**

The two methyl substituents of the **B-RR** isomer lie on C₃ and C₅ and are *trans* to one another. The general reaction for their formation is shown in Figure 4.15 followed by the equilibrium between the conformers in Figure 4.16.

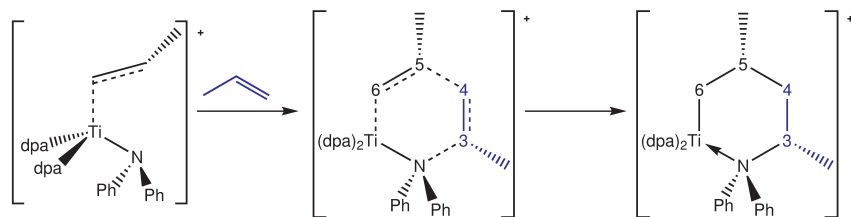
Figure 4.15: Pathway for the formation of **B-RR**

Figure 4.16: Equilibrium of the two chair conformations in **B-RR**

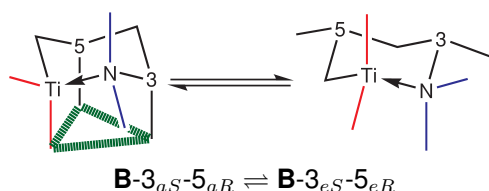
The **B-3_{eR}-5_{aR}** complex was the first pseudo-cyclic structure found and is the lower energy chair conformation of the **B-RR** set, lying 12.49 kJ mol⁻¹ lower in energy than **B-3_{aR}-5_{eR}** conformer but 29.94 kJ mol⁻¹ above that of the lowest energy **A-4_{eR}-5_{eR}** conformer. The equilibrium constant for the reaction shown in Figure 4.16 is 7.95×10^{-3} , while the equilibrium constant for the reverse reaction is 1.26×10^2 . As with the **A-SR** set the methyl-diphenylamido interactions are similar and are between the methyl group and one of the phenyl rings of the axial diphenylamido ligand. Even though the titanium-nitrogen distance is slightly elongated in the higher energy conformer, **B-3_{aR}-5_{eR}**, the methyl group on C₃ is tilted inward toward the ring. This results in the closest interaction, which is between one of the hydrogen atoms of the methyl group and the *ipso*-carbon of the phenyl ring, being substantially shorter than the same interaction in the lower energy structure, 2.422 Å and 2.884 Å, respectively explaining the energetic difference. The same tilting effect is noted for the axial ligand on C₃ in all of the six-membered rings and is a result of the asymmetrical distortion in the ring due to the inclusion of the hetero-atoms.

B-SR

The two chair conformers of the **B-SR** isomer make up the highest and lowest energy structures of those in the **B** pathway and the **B-3_{aS}-5_{aR}** complex is the highest energy structure for all of the six-membered rings investigated.

Figure 4.17: Pathway for the formation of **B-SR**

The **B-3_{aS}-5_{aR}** complex has considerable 1,3 diaxial interactions. Both of the methyl sub-

Figure 4.18: Equilibrium of the two chair conformations in **B-SR**

stituents will interact with the axial diphenylamido group on titanium as well as each other. As with the two conformations of the **B-RR** isomer, the methyl on C₃ is tilted toward the ring and lies closer to the phenyl with a hydrogen-*ipso*-carbon distance of 2.470 Å. The methyl on C₅ is tilted away from the ring with the closest distance being between a hydrogen on the methyl group and an *ortho*-carbon separated by 2.958 Å. The two hydrogens that lie closest to the phenyl ring are also the two closest points between the methyl groups with a distance of 2.071 Å.

Due to these interactions the equilibrium lies far to the right. The equilibrium constant is 6.55×10^{10} and complex **B-3_{eS}-5_{eR}** is lower on the potential energy surface than **B-3_{aS}-5_{aR}** by 62.33 kJ mol⁻¹. The **B-3_{eS}-5_{eR}** conformer is 5.95 kJ mol⁻¹ higher on the potential energy surface than the **A-4_{eR}-5_{eR}** conformer which also exhibits no substituent-substituent diaxial interactions.

4.2.3 Summary of intermediates involving six-membered rings

Of the eight pseudo-six-membered ring structures shown here the **A-4_{eR}-5_{eR}** complex is the lowest in energy. The next lowest energy conformation is **B-3_{eS}-5_{eR}** which also contains no 1,3 diaxial interactions but is nearly 6 kJ mol higher in energy showing the preference for the orientation of the incoming olefin to that shown in Pathway **A** over that of Pathway **B**. This energetic difference is also exhibited between conformations **A-4_{eS}-5_{aR}** and **B-3_{eR}-5_{aR}** where the diaxial interaction is between the diphenylamido ligand and the methyl on C₅. Again when the second methyl substituent of the incoming propylene is on C₄, away from the bulky diphenylamido ligand, the complex is lower in energy, in this case by 6.68 kJ mol⁻¹. A graph showing the energy for all of the six-membered chair conformations relative to **A-4_{eR}-5_{eR}** is shown in Figure 4.19.

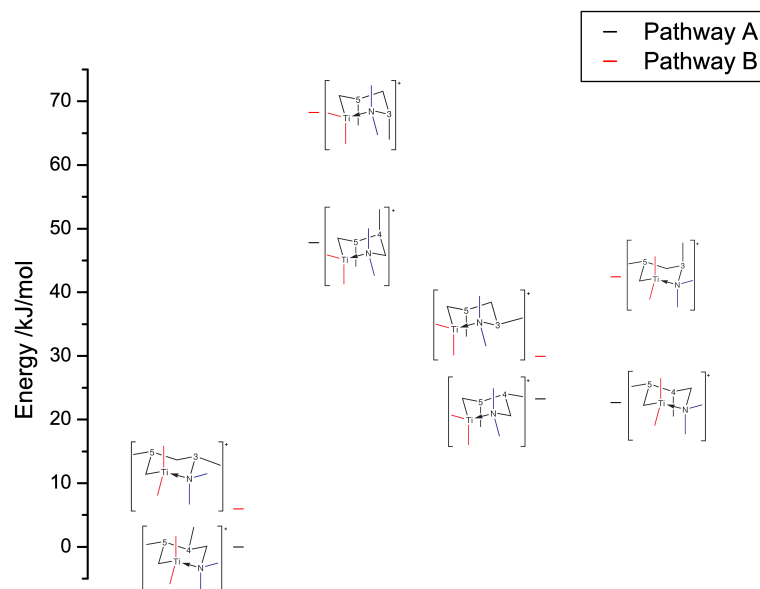


Figure 4.19: Relative energy for six-membered rings

4.3 Pathways involving five-membered rings

Pathways that involve five-membered rings are also a possibility and expected if the propylene molecule approaches the adduct from direction 3 seen in Figure 4.2. This type of addition goes through a pseudo 3 + 2 cycloaddition reaction as shown in Figure 4.20 where, like in Figure 4.3, only the alkene portion of the incoming monomer is shown in the expected intermediate.

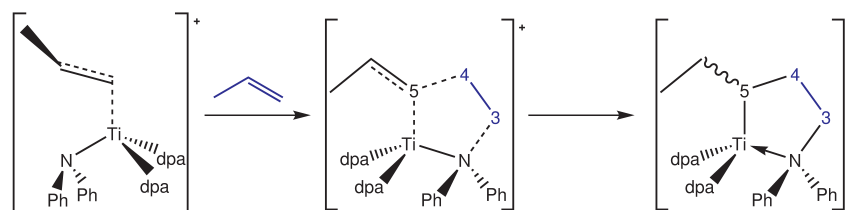


Figure 4.20: pseudo 3 + 2 cycloaddition

Two pathways are available to give five-membered rings, each having an ethyl substituent on the carbon closest to the titanium atom, C_5 . The ethyl group along with C_5 make up the originally bound propylene found in the adduct. Pathway **C** places the methyl substituent of the incoming propylene molecule on C_4 while Pathway **D** has the methyl substituent closer to the nitrogen atom on C_3 . As with the six-membered rings, each of these two pathways gives rise to the possibility of four stereo-isomers, namely *SS*, *RS*, *RR* and *SR*.

The most stable conformation of a five-membered ring has been shown to be either the envelope structure, Figure 4.21(a), or a half-chair, Figure 4.21(b), or often something in-between the two.^[127,129,130] For unsubstituted cyclopentane all carbon atoms are equivalent and a fast pseudorotation occurs so that each atom in turn assumes the apex or flap position of the envelope conformation. For rings containing at least one hetero atom or substituent, one particular form of the envelope conformation is often more stable.

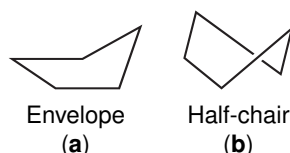


Figure 4.21: Possible conformations of five-membered rings

Each of the potential stereo-isomers has a large number of possible conformations. It should be noted that although the apex atom in Figure 4.21(a) is shown as lying above the plane, it could also lie below the plane and due to the presence of substituents produces another conformer. This results in a total of ten potential envelope conformations for each stereo-isomer, five apex-up and five apex-down. Fortunately, as with the six-membered rings, enantiomeric pairs are available. As illustrated in Figure 4.22, the five **C-SS** apex-up envelope conformations and the five **C-RR** apex-down sets are enantiomers. The same is seen for the *RS/SR* sets. Due to this, only the five apex-up conformations were considered.

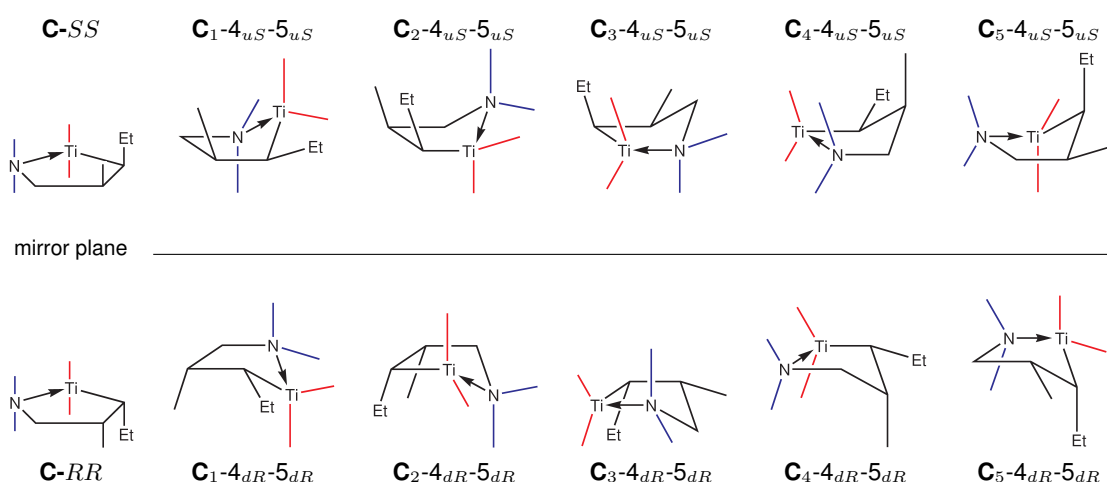


Figure 4.22: Enantiomeric examples of the envelope conformations of the apex-up **C-SS** and apex-down **C-RR**

For each stereo-isomer, these five different envelope conformations were used as the starting points for the optimisations which took place without restraining any coordinates. Unfortunately,

stable structures for some conformers were unable to be found; for example, the conformer where C_5 , which has the ethyl substituent, is the apex atom was not found for any of the eight possible stereo-isomers. The planarity of the the four non-apex atoms in the optimised structures vary greatly from nearly planar to a torsional angle of over 30° giving rise, in some cases, to a half-chair conformation.

For each structure the five possible torsional distortions within the ring, i.e. $(N-C_3-C_4-C_5)$, $(C_3-C_4-C_5-Ti)$, (C_4-C_5-Ti-N) , $(C_5-Ti-N-C_3)$ and $(Ti-N-C_3-C_4)$, were measured and the atom not included in the angle with the smallest magnitude is taken as the apex atom. For example, the five torsional distortions for the conformer labelled $C_3-4_{uS}-5_{uS}$ are listed in Table 4.3. The distortion that has the smallest magnitude is that for (C_4-C_5-Ti-N) making C_3 the apex atom.

$(N-C_3-C_4-C_5)$	$(C_3-C_4-C_5-Ti)$	(C_4-C_5-Ti-N)	$(C_5-Ti-N-C_3)$	$(Ti-N-C_3-C_4)$
66.83°	-41.31°	11.53°	17.77°	-45.43°

Table 4.3: Torsional distortions in $C_3-4_{uS}-5_{uS}$

4.3.1 Pathway C

Pathway **C** involves the formation of a five-membered ring where the methyl group of the propylene molecule is on C_4 , closer to the previously bound propyl group than the nitrogen atom. The general reaction can be seen in Figure 4.23. Both the methyl and ethyl groups are stereo-specific giving four distinct stereo-isomers.

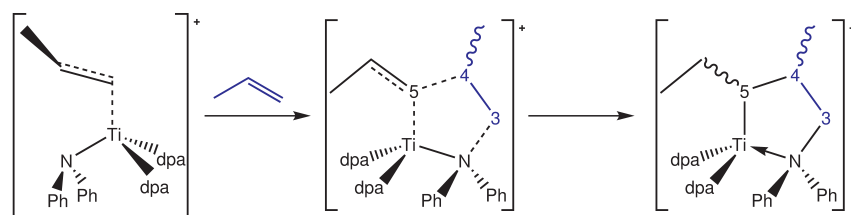


Figure 4.23: Pathway C

C-SS

The reaction for the formation of the **C-SS** isomer can be seen in Figure 4.24 and the five envelope type conformers are shown in Figure 4.25 along with their labels. Minimum energy structures for four out of the five conformations were found. These four structures span an energy difference of

over 16 kJ mol^{-1} with the lowest energy structure being that of the $\mathbf{C}_3\text{-}4_{uS}\text{-}5_{uS}$ conformer while the highest energy conformer is $\mathbf{C}_4\text{-}4_{uS}\text{-}5_{uS}$.

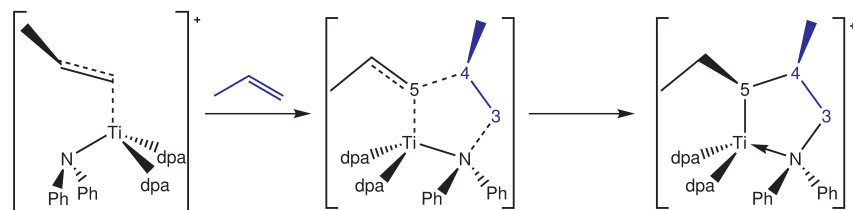


Figure 4.24: Pathway for the formation of $\mathbf{C}\text{-}SS$

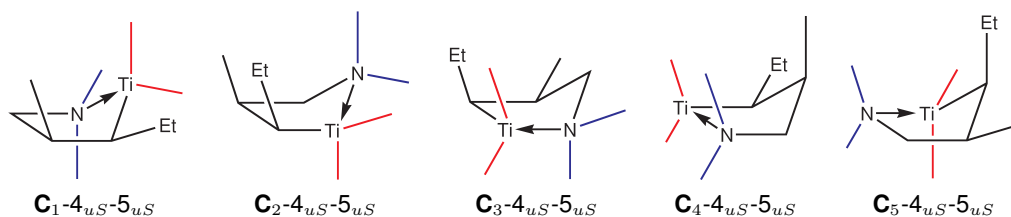
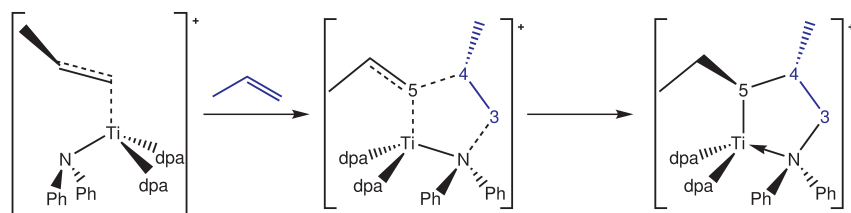


Figure 4.25: Possible envelope conformations of $\mathbf{C}\text{-}SS$

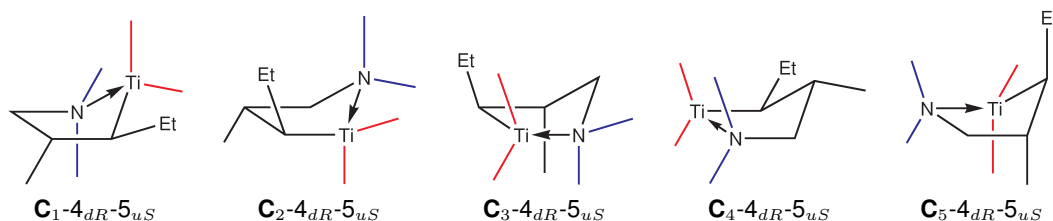
The highest energy isomer, $\mathbf{C}_4\text{-}4_{uS}\text{-}5_{uS}$, has the methyl substituent in the flagpole position and contains the largest N–Ti distance of the four conformers. The next highest in energy is the $\mathbf{C}_1\text{-}4_{uS}\text{-}5_{uS}$ conformer which has a diphenylamido ligand in the flagpole position and has the largest torsional distortion with a (N–C₃–C₄–C₅) angle of -21.74° and is only 2.18 kJ mol^{-1} lower in energy. The $\mathbf{C}_2\text{-}4_{uS}\text{-}5_{uS}$ conformer is closest to the envelope conformation with a (C₃–C₄–C₅–Ti) torsional angle of -1.51° and 4.26 kJ mol^{-1} lower than the $\mathbf{C}_1\text{-}4_{uS}\text{-}5_{uS}$ conformer on the potential energy surface. The lowest energy conformer, $\mathbf{C}_3\text{-}4_{uS}\text{-}5_{uS}$, is close to a half-chair type structure with a (C₄–C₅–Ti–N) torsional distortion of 11.53° , has the longest Ti–C₅ bond length, 2.085 \AA , and second longest Ti–N interaction, 2.277 \AA , of the conformations found. It is 9.57 kJ mol^{-1} lower than the $\mathbf{C}_2\text{-}4_{uS}\text{-}5_{uS}$ and $28.04 \text{ kJ mol}^{-1}$ higher in energy than the lowest energy six-membered ring isomer.

$\mathbf{C}\text{-}RS$

Suitable minimum energy structures close to the $\mathbf{C}_3\text{-}4_{dR}\text{-}5_{uS}$ and $\mathbf{C}_5\text{-}4_{dR}\text{-}5_{uS}$ conformations of the $\mathbf{C}\text{-}RS$ set could not be found. Therefore, only three of the conformers of the $\mathbf{C}\text{-}RS$ isomer were located. These three conformations all have a half-chair type conformation with the torsional angle of the atoms that would be expected to be planar in the envelope structure varying from

Figure 4.26: Pathway for the formation of **C-RS**

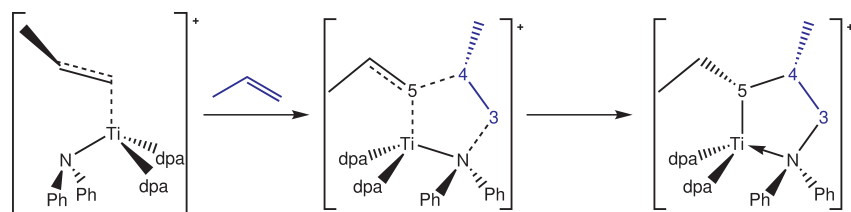
10.36° in **C**₂-4_{dR}-5_{uS}, -10.91° in **C**₁-4_{dR}-5_{uS} and -14.29° in **C**₄-4_{dR}-5_{uS}.

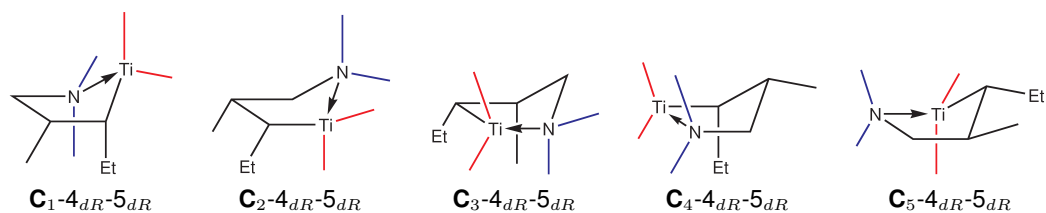
Figure 4.27: Possible envelope conformations of **C-RS**

The energy difference spanned by these three conformations is over 19 kJ mol⁻¹ with the highest energy structure being the **C**₄-4_{dR}-5_{uS} conformer, while the **C**₁-4_{dR}-5_{uS} conformation is less than 4 kJ mol⁻¹ higher on the potential energy surface than the most stable conformation. **C**₂-4_{dR}-5_{uS} is the lowest in energy and is the lowest energy conformation of all those found for Pathway **C**, lying 12.59 kJ mol⁻¹ higher in energy than the lowest energy six-membered ring isomer.

C-RR

Only three conformations of the **C-RR** isomer were found. Stable minima for the **C**₁-4_{dR}-5_{dR} and **C**₅-4_{dR}-5_{dR} conformations were not able to be located. The three conformations that were found are all very close in energy only spanning a difference of 3.33 kJ mol⁻¹. The located conformations of the **C-RR** isomer are all fairly close to the envelope conformation with the largest distortion being less than 12°.

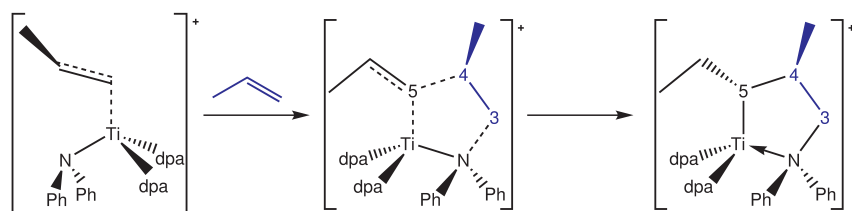
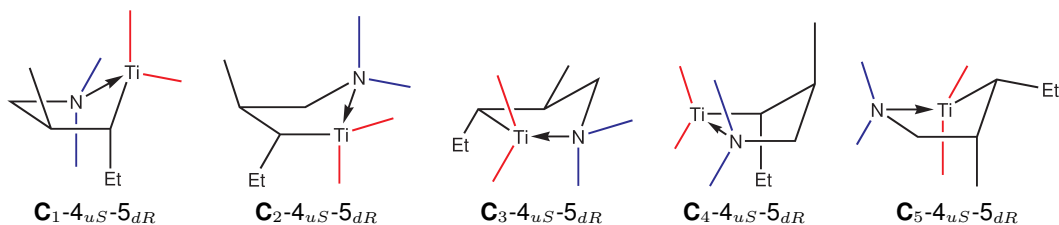
Figure 4.28: Pathway for the formation of **C-RR**

Figure 4.29: Possible envelope conformations of **C-RR**

The highest energy conformer, **C₄-4_{dR}-5_{dR}** has a ($C_5-Ti-N-C_3$) torsion of 8.92° while **C₂-4_{dR}-5_{dR}** which is less than 1 kJ mol^{-1} lower in energy has the largest torsion with an 11.43° angle for ($C_3-C_4-C_5-Ti$). The lowest energy conformation is the **C₃-4_{dR}-5_{dR}** which is very close to the envelope type structure with a (C_4-C_5-Ti-N) torsional angle of only -2.025° . The **C₃-4_{dR}-5_{dR}** conformer is $17.52 \text{ kJ mol}^{-1}$ higher in energy relative to the lowest energy six-membered ring.

C-SR

Much like the **C-RR** set, within the **C-SR** set minima for conformations where the apex atom is titanium atom or C_5 were not found; however the torsional angles of the expected planar atoms are again quite small, the largest again being less than 12° . Unlike the **C-RR** set, the energy difference exhibited is quite large with an energy difference of over 31 kJ mol^{-1} between the highest and lowest energy conformations.

Figure 4.30: Pathway for the formation of **C-SR**Figure 4.31: Possible envelope conformations of **C-SR**

The highest energy conformation is that of **C₄-4_{uS}-5_{dR}** which, like the the **C₄-4_{uS}-5_{uS}** conformation, has the methyl substituent in the flagpole position. **C₄-4_{uS}-5_{dR}** lies closest to the envelope

conformation with a ($C_5-Ti-N-C_3$) torsion of 1.79° and is the highest in energy of the conformations within Pathway **C**. The $C_2-4_{uS}-5_{dR}$ lies nearly 21 kJ mol^{-1} lower in energy and has the largest distortion with ($C_3-C_4-C_5-Ti$) = 11.59° . The lowest energy conformation, $C_3-4_{uS}-5_{dR}$, is the second lowest energy structure within Pathway **C** lying less than 3 kJ mol^{-1} higher in energy than the $C_2-4_{dR}-5_{uS}$ structure. The distortion of the (C_4-C_5-Ti-N) plane is -8.49° .

4.3.2 Pathway D

Pathway **D** consists of the formation of a five-membered ring where the methyl group of the propylene molecule is situated so that it lies closer to the nitrogen atom as the propylene moiety approaches the catalyst. This is shown pictorially in Figure 4.32. As with Pathway **C**, no conformations where C_5 , which has the ethyl substituent, was the apex atom were located. The four possible stereo-isomers are shown below.

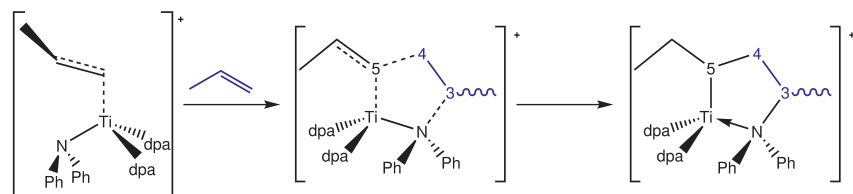


Figure 4.32: Pathway **D**

D-SS

Within the **D-SS** isomer, three conformation $D_1-4_{dS}-5_{uS}$, $D_3-4_{dS}-5_{uS}$ and $D_4-4_{dS}-5_{uS}$ were located while $D_2-4_{dS}-5_{uS}$ and $D_5-4_{dS}-5_{uS}$ were not.

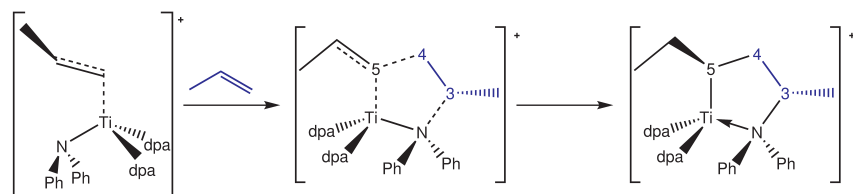
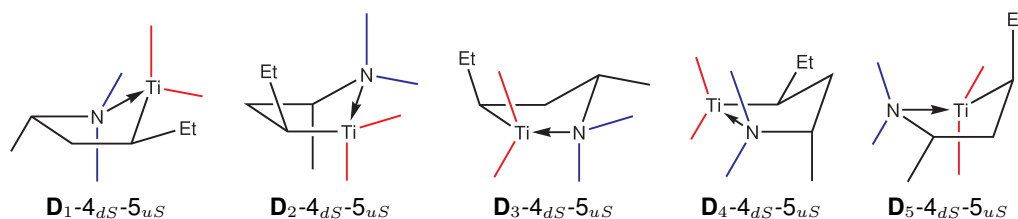


Figure 4.33: Pathway for the formation of **D-SS**

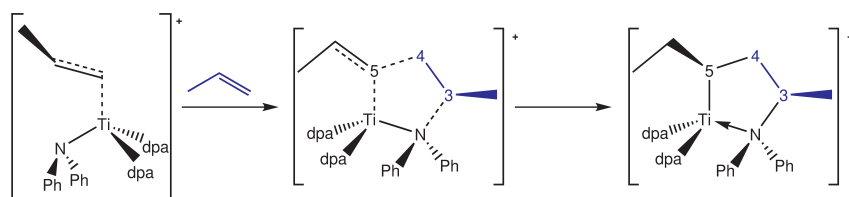
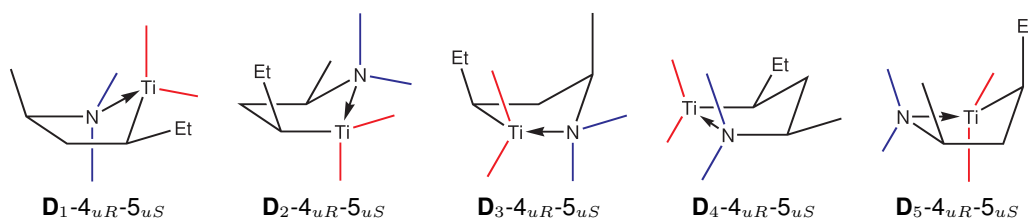
The conformations for $D_3-4_{dS}-5_{uS}$ and $D_4-4_{dS}-5_{uS}$ are nearly degenerate and are much closer to the envelope conformation with torsional angles of (C_4-C_5-Ti-N) and ($C_5-Ti-N-C_3$) as 5.24° and -9.71° respectively, than the $D_1-4_{dS}-5_{uS}$ conformer which is roughly 17 kJ mol^{-1} lower

Figure 4.34: Possible envelope conformations of **D-SS**

in energy with a much larger torsional distortion shown by the (N–C₃–C₄–C₅) torsional angle of 18.91°. The **D**₁-4_{dS}-5_{uS} conformation is 15.66 kJ mol⁻¹ higher in energy than the lowest six-membered ring conformation.

D-RS

Four conformations of the **D-RS** isomer were found. All four conformations lie close to the envelope type structure with the largest torsional distortion being -8.23° for conformer **D**₂-4_{uR}-5_{uS}. The energy difference is considerable with the highest energy conformation 29 kJ mol⁻¹ higher than the lowest.

Figure 4.35: Pathway for the formation of **D-RS**Figure 4.36: Possible envelope conformations of **D-RS**

The highest energy conformation is the **D**₃-4_{uR}-5_{uS} which forces the methyl substituent on C₃ into a flagpole position. and has a (C₄–C₅–Ti–N) torsional angle of 3.25°. The second highest energy conformation is the **D**₂-4_{uR}-5_{uS} conformer which has the largest deviation from the envelope type conformation with a (C₃–C₄–C₅–Ti) of -8.23° and is 13 kJ mol⁻¹ lower in energy. The **D**₁-4_{uR}-5_{uS} conformer is a further 11 kJ mol⁻¹ lower with a (N–C₃–C₄–C₅) torsion

of -1.49° . The lowest energy conformer, $\mathbf{D}_4\text{-}4_{uR}\text{-}5_{uS}$ is the closest to the envelope structure with a $\text{C}_5\text{-Ti-N-C}_3$ of only -0.39° .

D-RR

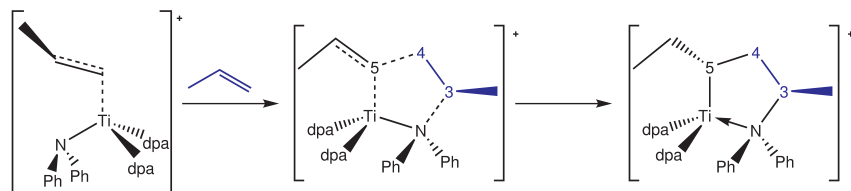


Figure 4.37: Pathway for the formation of **D-RR**

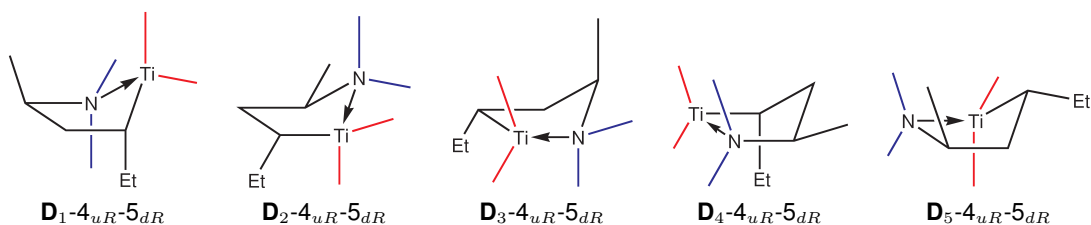


Figure 4.38: Possible envelope conformations of **D-RR**

The four conformations of the **D-RR** isomer that were located follow a similar energetic pattern to those of the **D-RS** isomer. The highest energy conformation is that of $\mathbf{D}_3\text{-}4_{uR}\text{-}5_{dR}$ again where the methyl substituent on C_3 is in a flagpole position. This conformer is the highest energy of all conformations found for pathway **D**. Conformer $\mathbf{D}_1\text{-}4_{uR}\text{-}5_{dR}$ is 20 kJ mol^{-1} lower in energy followed by the $\mathbf{D}_2\text{-}4_{uR}\text{-}5_{dR}$ and $\mathbf{D}_4\text{-}4_{uR}\text{-}5_{dR}$ conformers which approximately 17 kJ mol^{-1} lower in energy and only differ by 1 kJ mol^{-1} from each other.

D-SR

Unfortunately only two conformations of the **D-RS** pathway were able to be located.

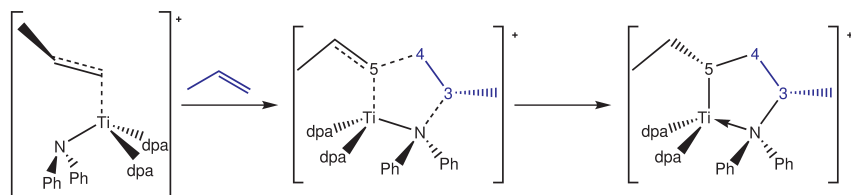
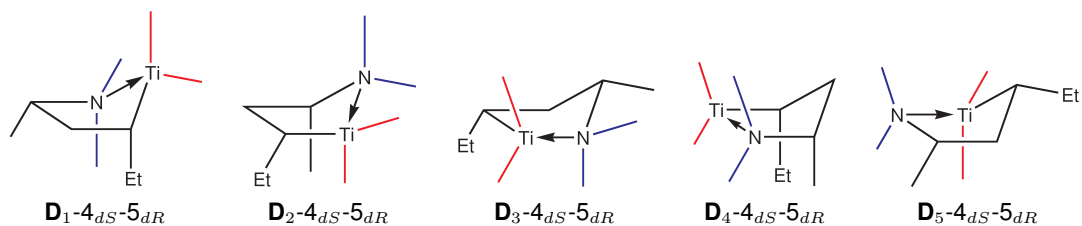


Figure 4.39: Pathway for the formation of **D-SR**

Conformations $\mathbf{D}_1\text{-}4_{dS}\text{-}5_{dR}$ and $\mathbf{D}_2\text{-}4_{dS}\text{-}5_{dR}$ along with the $\mathbf{D}_4\text{-}4_{dS}\text{-}5_{dR}$ conformer were not

Figure 4.40: Possible envelope conformations of **D-SR**

located, however conformation **D₃-4_{dS}-5_{dR}** is the lowest energy structure found in pathway **D** and only has an observed energy difference to conformation **C₂-4_{dR}-5_{uS}**, the lowest energy conformer of pathway **C**, of less than 1 kJ mol⁻¹. The **D₄-4_{dS}-5_{dR}** conformation is 32 kJ mol⁻¹ higher in energy and has a torsional (C₅–Ti–N–C₃) angle of 14.53°.

4.3.3 Summary of intermediates involving five-membered rings

Tables 4.4 and 4.5 give the relative energies of all five-membered ring intermediates with respect to the lowest energy six-membered ring conformer, **A-4_{eR}-5_{eR}**.

C-SS	C₁-4_{uS}-5_{uS} 41.87	C₂-4_{uS}-5_{uS} 37.61	C₃-4_{uS}-5_{uS} 28.04	C₄-4_{uS}-5_{uS} 44.05
C-RS	C₁-4_{dR}-5_{uS} 16.11	C₂-4_{dR}-5_{uS} 12.59	C₃-4_{dR}-5_{uS} –	C₄-4_{dR}-5_{uS} 32.26
C-RR	C₁-4_{dR}-5_{dR} –	C₂-4_{dR}-5_{dR} 20.00	C₃-4_{dR}-5_{dR} 17.52	C₄-4_{dR}-5_{dR} 20.85
C-SR	C₁-4_{uS}-5_{dR} –	C₂-4_{uS}-5_{dR} 26.36	C₃-4_{uS}-5_{dR} 15.51	C₄-4_{uS}-5_{dR} 47.20

Table 4.4: Relative Energy (/kJ mol⁻¹) of Pathway **C**, five-membered ring intermediates with respect to the lowest energy six-membered ring intermediate

The energy difference between the lowest energy conformers from pathways **C** and **D**, **C**₂-4_{dR}-5_{uS} and **D**₃-4_{dS}-5_{dR} respectively, is less than 1 kJ mol⁻¹ and is only 12 kJ mol⁻¹ above that of the **A**-4_{eR}-5_{eR} conformer.

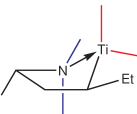
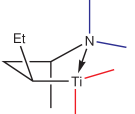
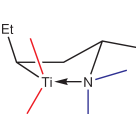
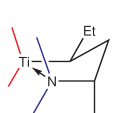
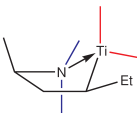

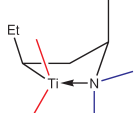
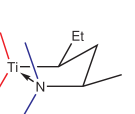
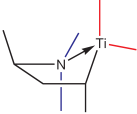
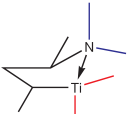
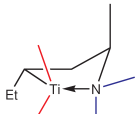
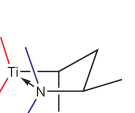
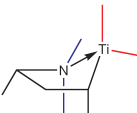
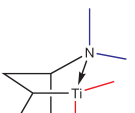
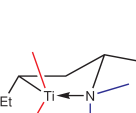
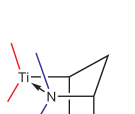
D-SS	D₁-4_{dS}-5_{uS}  15.66	D₂-4_{dS}-5_{uS}  —	D₃-4_{dS}-5_{uS}  32.50	D₄-4_{dS}-5_{uS}  32.78
D-RS	D₁-4_{uR}-5_{uS}  34.54	D₂-4_{uR}-5_{uS}  45.66	D₃-4_{uR}-5_{uS}  58.64	D₄-4_{uR}-5_{uS}  29.49
D-RR	D₁-4_{uR}-5_{dR}  51.10	D₂-4_{uR}-5_{dR}  33.95	D₃-4_{uR}-5_{dR}  71.71	D₄-4_{uR}-5_{dR}  32.87
D-SR	D₁-4_{dS}-5_{dR}  —	D₂-4_{dS}-5_{dR}  —	D₃-4_{dS}-5_{dR}  12.08	D₄-4_{dS}-5_{dR}  44.10

Table 4.5: Relative Energy (kJ mol⁻¹) of Pathway **D**, five-membered ring intermediates with respect to the lowest energy six-membered intermediate

4.4 Pathways involving geometry rearrangement at the metal centre

The intermediates suggested in this section were not calculated but are presented here for completeness. Calculations were not undertaken as the activation energy for the discussed rearrangement is expected to be prohibitively large due to the bulky nature of the ligand set, therefore, making them kinetically unlikely. Additionally, as seen in Chapter 3, polymerisation does not occur when the (dpa)₃TiCH₃ (**5**) system is used alone, which would require a similar geometry rearrangement.

As they were not calculated, the addition of an ethylene moiety to the propylene-adduct, **2**, instead of a propylene is used for the pathways presented in this section. For each case, a number of structural and stereo-isomers analogous to those in the pathways discussed above would be available with the addition of propylene as opposed to ethylene.

Two potential pathways where the geometry about the titanium centre changes from pseudo-tetrahedral to trigonal bipyramidal can be envisioned and are presented here. In each case one of the diphenylamido ligands would rotate to an axial position leaving the 'active site' in the equatorial plane, *cis*- to the α -C of the adduct.

4.4.1 Pathway E

The first of these pathways to be examined, Pathway **E** seen in Figure 4.41, begins with the re-arrangement of the adduct from tetrahedral to trigonal bipyramidal and the originally added propylene as syn-periplanar to the two ligands in the equatorial plane. The incoming olefin then approaches the active site and forms a metallocyclobutane intermediate analogous to that seen in the Cossée-Arlman and modified Green-Rooney mechanisms.

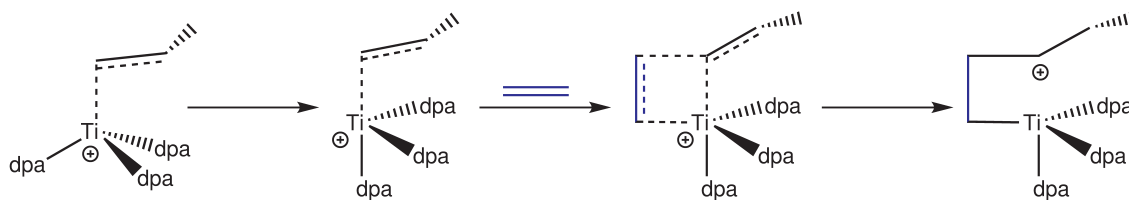


Figure 4.41: Pathway **E**

The electron count for the resultant intermediate is expected to be ML_3X_4 , a 14-electron system. The positive charge of the system is expected to transfer to the polymer chain. This is because if the positive charge remained associated with the four-coordinate titanium centre it would result in a non-physical Ti^V species having a CBC classification of $ML_3X_4^+$ or ML_2X_5 .

The geometry at the titanium centre would then be expected to return to pseudo-tetrahedral and the polymerisation would no longer be directed by the metal centre but by the carbocation. This pathway also does not explain the suspected structural change of the catalyst as noted by the experimental data and is therefore excluded.

4.4.2 Pathway F

In the second pathway, Pathway **F** seen in Figure 4.42, the incoming olefin approaches the active site and forms a five-membered ring through a 3 + 2 cycloaddition.

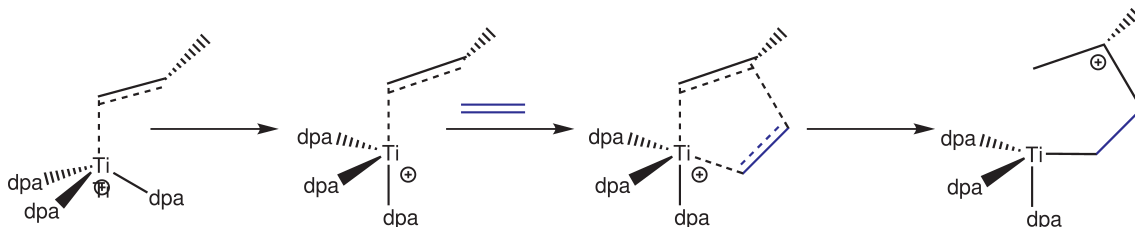


Figure 4.42: Pathway **F**

As in Pathway **E**, the charge is expected to transfer to polymer chain forming, in this case, a tertiary carbocation on the γ -C. This would be due to a 1,2-hydrogen rearrangement as tertiary carbocations are considerably more stable than primary carbocation.^[127]

Again the geometry at the titanium centre is expected to return to tetrahedral.

Although not expected for this system, these pathways have been shown for completeness. If, however, a less electron deficient metal centre were used, the relevance of these pathways may be realized.

4.5 Conclusions

Of the structural and stereo-isomers calculated, the lowest energy structure was found to be that of **A-4_{eR}-5_{eR}** which contains a six-membered ring without 1,3 diaxial interactions. The second lowest, **B-3_{eS}-5_{eR}**, is less than 6 kJ mol⁻¹ higher in energy and also contains a six-membered ring, while the remainder of the structures formed by these pathways are more than 20 kJ mol⁻¹ higher in energy. The two lowest energy five-membered ring conformations, **C₂-4_{dR}-5_{uS}** and **D₃-4_{dS}-5_{dR}**, were slightly more than 12 kJ mol⁻¹ higher in energy than the lowest energy structure. These four conformers are shown in Figure 4.43

The lowest energy structure, **A-4_{eR}-5_{eR}**, was used as the chosen intermediate in Chapter 3. However, due to the small energy difference seen, all of structures shown in Figure 4.43 might be expected to be energetically accessible and the lowest energy structure can not conclusively be said to be the only intermediate. To further differentiate the possibilities, a study of the poten-

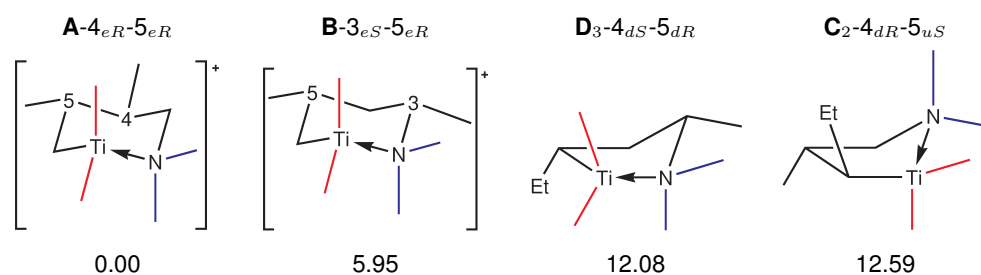


Figure 4.43: Lowest energy conformers and relative energies kJ mol^{-1}

tial energy surface for the formation of each of the conformers could be undertaken in order to determine the expected energy barrier. A study for the addition of the second propylene moiety and subsequent insertion would also be helpful in order to find the lowest energy pathway. These results could then be compared with structural data taken from experimental studies to confirm the mechanism.

Chapter 5

Generalizations of Trigonal Group

IV Metal Centres

5.1 Introduction

In this chapter, a series of simple transition metal complexes that contain the essential feature of π -acid-base chemistry in the coordination sphere in a manner consistent with the covalent bond classification (CBC) electron counting method will be calculated and analysed.^[71]

The main focus will be on the complexes $[(R_2N)_3M]^+$, $(R_2N)_3MH$ and $(R_2N)_3MF$, where R = methyl and M = Ti. The analysis of the cationic species yields the basic orbital framework at the metal centre; the hydride yields a pure σ -interaction with the basic frame, which will be consistent in principle for any axial ligand, while the fluoride represents a strong π -base in the axial position. This set of relatively simple complexes have been studied in order to give greater light to the more complicated species discussed in Chapter 2.

5.2 Importance of amido transition metal complexes

Transition metal amide systems are employed in a diverse set of chemical contexts which range from organic synthesis^[131] to olefin polymerisation^[131,132] and small molecule activation.^[133,134] This ubiquitous presence in nearly all areas of chemistry has resulted in over 600 structurally char-

acterised non-chelating transition metal amido compounds within the past 30 years.^[135] Furthermore, a search of the Cambridge Crystallographic Structural Database (CCSD) for the M–NR₂ moiety, where M is a transition metal, nitrogen is restricted to be three-coordinate and R = C, H, or Si, produces over 18,000 hits.^[111,112] A large number of these compounds include an early transition metal, presumably due to the Lewis acidic metal centre combined with the potential Lewis basic nature of the amido ligand as discussed in Section 5.2.2. Moreover, the amido ligand is robust, can act as a spectator ligand in many systems and, especially when polydentate, can support a high oxidation state, for example in complexes of the form (tren)M where tren = [N((CH₂CH₂)N(TMS)₂)₃]^{3–}.

5.2.1 Notable compounds

The first reported transition metal amide was Ti(NPh₂)₄,^[136] an important compound with respect to the discussion found in Chapter 2. Other compounds of great consequence are trigonal amido complexes. The first low-coordinate transition metal amides, where low-coordinate is defined by a coordination number of two or three, were prepared by Bürger and Wannagat in the 1960s^[137,138] where the N(SiMe₃)₂ ligand was employed. The scope of this ligand was then expanded slightly by the work of Bradley^[139] who had also used N(ⁱPr)₂.^[140] Lappert also expanded the field by investigating transition metals as well as germanium, tin and lead compounds with both the N(SiMe₃)₂ and the isoelectric CH(SiMe₃)₂ ligands.^[141–146]

Further interest in amido complexes sparked in the early-1990s and evolved quickly after Verkade,^[147–149] Schrock^[150–158] and others explored the chemistry of early transition metals with the polydentate tren ligand, N(C₂H₄NR)₃^{3–}, where the R group varies widely including H, methyl, phenyl and silyl among many others. The use of this ligand typically gives a trigonal-monopyramidal geometry about the metal centre with the axial nitrogen often forming a dative bond to the metal. The R substituents form a pocket or active site and in conjunction with the stability provided by the electron rich nature of the ligand enables the metal centre to form stable complexes that exhibit multiple bonding to main group elements such as C, N, P, As, O, S and Se when a further ligand is bound in the second axial position.^[156]

Seminal contributions were made soon after by Cummins who was able to cleave the N–N

bond in N_2 ^[133] and N_2O ^[134] at ambient temperatures using a molybdenum complex with a 'two-sided' ligand system, $\text{Mo}(\text{N}(\text{R})\text{Ar})_3$ where $\text{R} = \text{C}(\text{CD}_3)_2\text{CH}_3$ $\text{Ar} = 3,5\text{-C}_6\text{H}_3\text{Me}_2$, shown in Figure 5.1. Other variations of these two-sided ligands include $\text{R} = t\text{Bu}$, 1-adamantyl, 2-adamantyl and $\text{Ar} = \text{Ph}$, 4- $\text{C}_6\text{H}_4\text{F}$ and offered the first examples of homoleptic, three-coordinate, amido complexes involving the second or third row transition elements.^[159] As can be seen in Figure 5.1, the coordination of these compounds involves a trigonal-planar MoN_3 system with the aryl groups on one side of the plane and the alkyl groups on the other with the more rigid aryl groups leaving an open site for further reaction with small molecules. Since this time electronic structure and bonding investigations with focus on trigonal systems have been made by Alvarez.^[160,161] treating the amido ligand as a 'single-faced,'^[162] or LX-type,^[71] π -donor.

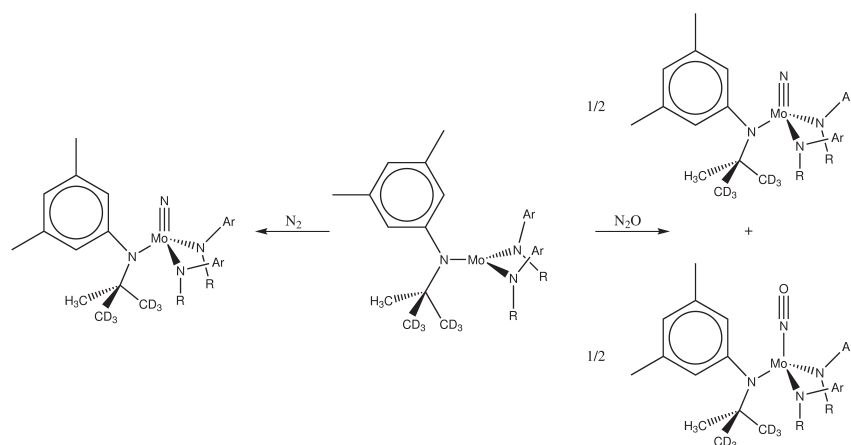


Figure 5.1: Reaction of Mo complex with a 'two-sided' ligand set with N_2 ^[133] and N_2O ^[134]

The amido ligand displays several bonding motifs, included both bridging and terminal motifs, while polydentate bonding is also possible with ligands such as $\text{tren N}(\text{C}_2\text{H}_4\text{NR})_3^{3-}$. To illustrate this diversity an example can be seen in Figure 5.2 showing the difference in structure between the gas^[163] and solid state^[164] phases of $\text{Zr}(\text{NMe}_2)_4$.

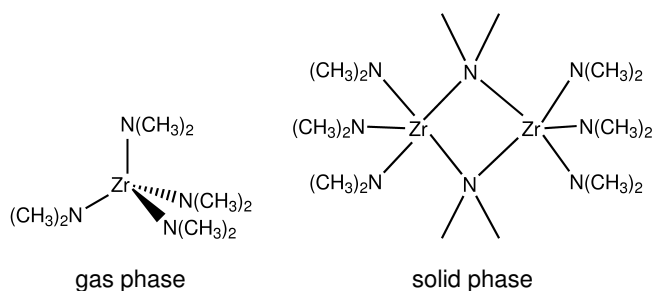


Figure 5.2: Gas^[163] vs. solid^[164] phase $\text{Zr}(\text{NMe}_2)_4$ illustrating the terminal and bridging bonding motifs in the amido ligand.

5.2.2 Group theoretical analysis

The following analyses will be limited to monodentate, terminally bound amido ligands as it is the general platform for the compounds found in Chapter 2. The terminal di-alkylamido ligand can exhibit two different bonding motifs falling under either the X or LX classification of the covalent bond classification scheme. The LX arrangement is by far the most common; however, the X classification with a pyramidal geometry about the nitrogen atom, which diminishes the π -orbital overlap, is possible in principle. Both bonding motifs are shown in Figure 5.3.

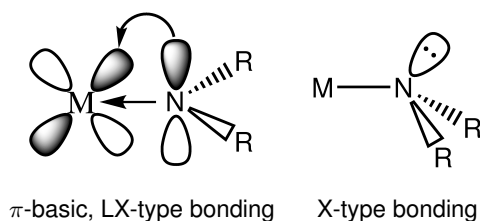


Figure 5.3: Bonding motifs of the di-alkylamido ligand

Although the majority of amido-containing complexes contain planar, trigonal nitrogen atoms, there are examples where a terminal amido is observed to be pyramidal. *tris*(dimethylamido) (μ -pentamethylborazinylamido)zirconium(IV) dimer, shown in Figure 5.4, exhibits this rare ligand geometry. In this compound, the four black dimethylamido ligands exhibit typical trigonal-planar geometry about the nitrogen atom with the sum of the bond angles very near to 360° in each case, while the two amido units outlined in blue are pyramidal with combined bond angles of 333.1° and 333.7° around each nitrogen. The Zr–N bond lengths of the latter type are elongated (2.529\AA) and are the longest lengths recorded for any terminal $(\text{CH}_3)_2\text{N}$ –Zr complex found within the CSD.^[111,112]

The planar amido groups have an average Zr–N bond length of 2.053\AA which is very close to the average length (2.057\AA) for terminal $(\text{CH}_3)_2\text{N}$ –Zr containing compounds. No notable variation in the N–C bond lengths was observed. The authors note that

"It is interesting that these bridging amido groups have a planar heavy atom geometry with sums of bond angles, 359.2° and 359.4° ."

No electronic investigation into the reason for the differences in bonding was included^[165] and to date, no theoretical studies of this compound have been published. Given the geometry, it is

tempting to count each Zr centre as ML_3X_4 for $14e^-$ Zr^{IV} , although involvement of the π -base function on N in an unorthodox manner would only give rise to a ML_4X_4 $16e^-$ centre and so the electron count is not decisive in this case.

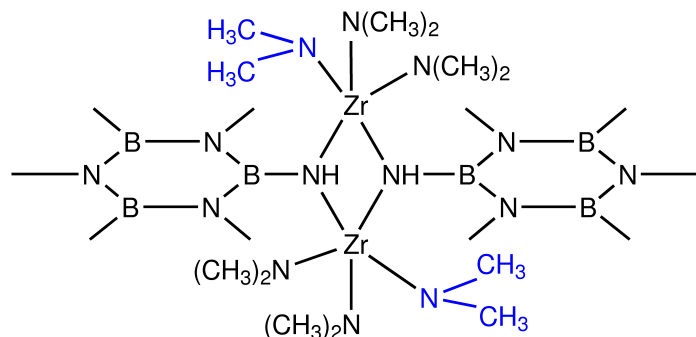


Figure 5.4: $[(CH_3)_2N]_3Zr[\mu-N(H)B_3(CH_3)_2N_3(CH_3)_3]_2$ ^[165]

Although a small number of examples such as the one discussed above can be found, the preponderance of structurally characterised terminal amido ligands demonstrate trigonal-planar geometry at nitrogen. The expected sum of the covalent radii of M and N in these complexes is also typically longer than the observed bond lengths which is often taken as evidence of M–N π -bonding. Another factor that could also contribute to the shortening of the M–N bond include polarization of the bond.^[166] It is generally accepted that at least some π -bonding occurs resulting in the formal classification of the ligand as LX. Further support of π donation has been provided through the use of core electron binding energies,^[167] even so the quantification of the π -bonding interaction is difficult.^[135,160,168]

Only the LX classification of the amido ligand will be used in the following analyses. The CBC classifications for the three classes of complex discussed in this chapter are given in Table 5.1.

Species	charged class	neutral class	Electron count at M
$[(R_2N)_3M]^+$	$L_3X_3^+$	L_2X_4	12
$(R_2N)_3MH$	-	L_3X_4	14
$(R_2N)_3MF$	-	L_3X_4	14

Table 5.1: CBC classifications for $[(R_2N)_3M]^+$, $(R_2N)_3MH$ and $(R_2N)_3MF$

In calculating the neutral CBC class for $[(R_2N)_3M]^+$, the formalism $L^+ = X$ has been used.

Basis functions

The ligand bases for these calculations follow the formal dissection of the coordination sphere using the CBC counting scheme. The ligand-based L function on N can be approximated by a $2p$ -type function of essentially atomic character and will have molecular π -symmetry with respect to the M–N vector. The ligand-based X function is of σ -symmetry with respect to the M–N vector and will be composed of a mixture of atomic $2p$ and $2s$ functions. The basis functions are shown in Figure 5.5.

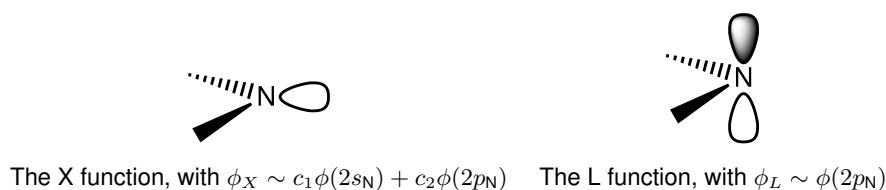


Figure 5.5: Ligand bases for the $(R_2N)_3M$ fragment

The basis functions on the metal centre are taken to be derived from the atomic nd , $(n+1)s$ and $(n+1)p$ wavefunctions, from which only the angular portions will be considered.

Point groups

The available point groups for this analysis all contain C_3 as the rotational subgroup, which gives the fundamental symmetries of the atom-atom interactions in the system.

In order of dimension, the available groups are C_3 , D_3 , C_{3v} and D_{3h} . The fundamental feature of the group theoretical analysis is the threefold rotational axis; symmetrical elaborations beyond this rotational axis change the state labels, but do not change the degeneracies of the fundamental scheme.

The irreducible representations for the metal-centred orbital bases are given in Table 5.2 and are taken from standard character tables.^[169]

	C_3	D_3	C_{3v}	D_{3h}
$(n+1)p$	$a + e$	$a_2 + e$	$a_1 + e$	$a_2'' + e'$
$(n+1)s$	a	a_1	a_1	a_1'
nd	$a + 2e$	$a_1 + 2e$	$a_1 + 2e$	$a_1' + e' + e''$

Table 5.2: Irreducible representations for the metal-centred orbitals

While D_{3h} is the most symmetric point group available for the cationic species, a minimum

structure fitting this description was not found and is assumed to be very high in energy. Instead, all structures calculated in this chapter are of C_3 symmetry, a result that can be attributed to a second-order Jahn-Teller distortion involving the overlap of ligand orbitals with a d_{z^2} type orbital of the metal centre resulting in lowering of energy through the reduction in symmetry.

In the pure rotational group for a trigonal metal centre, the reducible representations for ϕ_X and ϕ_L both span $A + E$. The C_3 character table, the reducible representations and the results of the projection operators of these functions are given in Table 5.3.

$h = 3$	E	C_3	C_3^2	$\varepsilon = \exp\left(\frac{2\pi i}{3}\right)$	
A	1	1	1	z, R_z	$x^2 + y^2, z^2$
E	$\begin{cases} 1 \\ 1 \end{cases}$	$\begin{cases} \varepsilon \\ \varepsilon^* \end{cases}$	$\begin{cases} \varepsilon^* \\ \varepsilon \end{cases}$	$\begin{pmatrix} (x, y), \\ (R_x, R_y) \end{pmatrix}$	$\begin{pmatrix} (xz, yz), \\ (x^2 - y^2, xy) \end{pmatrix}$
$\Gamma(\phi_X)$	3	0	0		
$\Gamma(\phi_L)$	3	0	0		
$\hat{P}_{(\phi_X)}(r_1)$	r_{1rad}	r_{2rad}	r_{3rad}		
$\hat{P}_{(\phi_L)}(t_1)$	t_{1tan}	t_{2tan}	t_{3tan}		

Table 5.3: Group table for C_3 together with $\Gamma(p)$ and the projection operator for the C p_z orbital

Formation of the Symmetry Adapted Linear Combinations (SALCs)

The projection operator is used to form the Symmetry Adapted Linear Combinations (SALCs) by applying it to the irreducible representations that are contained in each basis, namely $a + e$ for both the radial ϕ_X function and the tangential ϕ_L function.

When the projection operator for the radial function is applied to the irreducible representation A , the following result is found.

$$\begin{aligned}
 \varphi_{A_{rad}} &= \hat{P}_{(\phi_X)}(r) \cdot A \\
 &= r_1(1) + r_2(1) + r_3(1) \\
 \varphi_{A_{rad}} &\simeq r_1 + r_2 + r_3
 \end{aligned} \tag{5.2.1}$$

The application of the projection operator on the degenerate E set is made more difficult due to the inclusion of imaginary characters within the E representation. However, this obstacle is

simplified by the use of Euler's formula^[169]:

$$\exp(i\alpha) = \cos(\alpha) + i \sin(\alpha) \quad (5.2.2)$$

From equation (5.2.2), the E irreducible representation becomes

$$E \quad \begin{cases} 1 & \cos\left(\frac{2\pi}{3}\right) + i \sin\left(\frac{2\pi}{3}\right) & \cos\left(\frac{2\pi}{3}\right) - i \sin\left(\frac{2\pi}{3}\right) \\ 1 & \cos\left(\frac{2\pi}{3}\right) - i \sin\left(\frac{2\pi}{3}\right) & \cos\left(\frac{2\pi}{3}\right) + i \sin\left(\frac{2\pi}{3}\right) \end{cases}$$

The projection operator can now easily be applied to form the appropriate SALCs. Since the E set is degenerate, two functions must result from the projection. This is achieved by taking the linear combination of two rows within the irreducible representation.

$$\begin{aligned} \varphi_{E_{rad}(\pm)} &= \hat{P}_{(\phi_X)}(p) \cdot E \\ &= \left(r_1(1) + r_2 \left\{ \cos\left(\frac{2\pi}{3}\right) + i \sin\left(\frac{2\pi}{3}\right) \right\} + r_3 \left\{ \cos\left(\frac{2\pi}{3}\right) - i \sin\left(\frac{2\pi}{3}\right) \right\} \right) \\ &\quad \pm \left(r_1(1) + r_2 \left\{ \cos\left(\frac{2\pi}{3}\right) - i \sin\left(\frac{2\pi}{3}\right) \right\} + r_3 \left\{ \cos\left(\frac{2\pi}{3}\right) + i \sin\left(\frac{2\pi}{3}\right) \right\} \right) \\ \varphi_{E_{rad}(+)} &\simeq 2r_1 - r_2 - r_3 \\ \varphi_{E_{rad}(-)} &= i\sqrt{3}r_2 - i\sqrt{3}r_3 \simeq r_2 - r_3 \end{aligned} \quad (5.2.3)$$

As both the radial ϕ_X and the tangential ϕ_L functions result in the same reducible representation, spanning $a + e$, and give the same projection operator, the resultant SALCs calculated for the tangential function are equivalent to those in Equations (5.2.1) and (5.2.3) but will have a different orientation with respect to the centre of the molecule. Application of the projection operator onto the ϕ_L functions can be seen in Appendix .1 Visual representations of these functions can be seen in Figure 5.6.

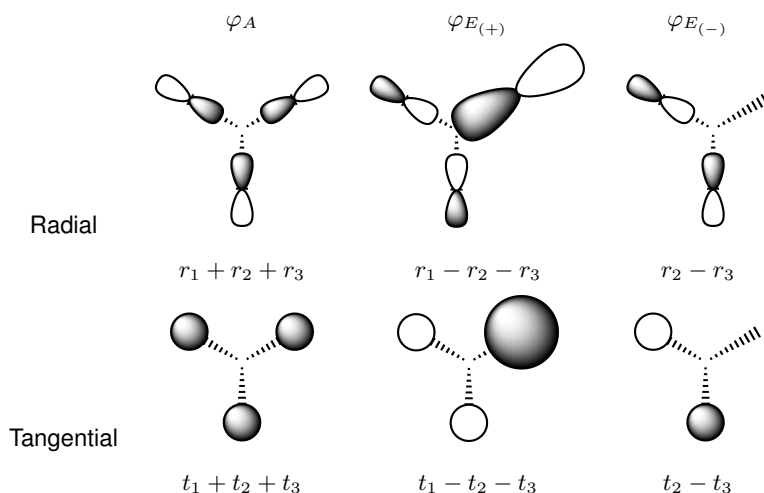


Figure 5.6: Calculated SALCs for the radial, ϕ_X , and tangential, ϕ_L , functions in C_3

Normalization of SALCs

For the basis functions calculated within the SALCs to be a valid wavefunction they must be normalized and orthogonal. This orthonormality requirement is achieved by the application of $\int \psi_i \psi_j d\mathbf{r} = \delta_{ij}$ where

$$\delta_{ij} = \begin{cases} 1 & \text{for } i = j \\ 0 & \text{for } i \neq j \end{cases}$$

The resulting normalized radial A wavefunction is

$$\varphi_{A_{rad}} = \frac{\sqrt{3}}{3} (r_1 + r_2 + r_3) \quad (5.2.4)$$

with the two E wavefunctions resulting as

$$\varphi_{E_{rad}(+)} = \frac{\sqrt{6}}{6} (2r_1 - r_2 - r_3) \quad (5.2.5a)$$

$$\varphi_{E_{rad}(-)} = \frac{\sqrt{2}}{2} (r_2 - r_3) \quad (5.2.5b)$$

Again, the same results will be obtained for both the radial and tangential functions. Full evaluation for the normalization of both the radial and tangential ligand functions can be found in Appendix .2

When the ligands overlap with the metal centre a new molecular wavefunction results which includes both the basis function for the ligands and the metal. The molecular wavefunction is written as

$$\Psi_{mol} = N(\lambda\varphi_{ligand} + \phi_M) \quad (5.2.6)$$

where φ_{ligand} is the normalized ligand SALCs listed in equations (5.2.4) and (5.2.5) and ϕ_M is the orbital on the metal centre. λ is the mixing coefficient and the normalizing constant, N , is defined by

$$N^2(1 + \lambda^2 + 2\lambda G) = 1 \quad (5.2.7)$$

where G is the total overlap of the metal orbital with the ligands and is defined by

$$G = \int \phi_M \varphi_{ligand} d\tau \quad (5.2.8)$$

and is generally expressed through the use of the two-atom overlap integral, S .^[170] The overlap integral is the standard constructive interactions expected from molecular orbital theory.

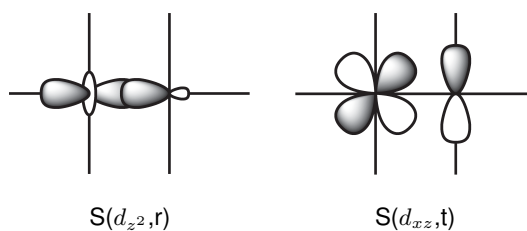


Figure 5.7: Overlap

5.2.3 Calculational results

If the mixing coefficient is taken as one and the molecular wavefunction is normalized in the usual way, the contributions of each of the basis functions should be able to be determined. The normalization of the molecular wavefunction where the ligand set are taken as the radial A function found in equation (5.2.4) results in:

$$\Psi_{mol,A} = \frac{\sqrt{6}}{6}r_1 + \frac{\sqrt{6}}{6}r_2 + \frac{\sqrt{6}}{6}r_3 + \frac{\sqrt{2}}{2}\phi_M \quad (5.2.9)$$

meaning that the contribution of the ligand is expected to be $3\left(\frac{\sqrt{6}}{6}\right)$ and that of the metal to be $\frac{\sqrt{2}}{2}$ giving the following ratio

$$\frac{3\left(\frac{\sqrt{6}}{6}\right)}{\left(3\left(\frac{\sqrt{6}}{6}\right) + \frac{\sqrt{2}}{2}\right)} : \frac{\frac{\sqrt{2}}{2}}{\left(3\left(\frac{\sqrt{6}}{6}\right) + \frac{\sqrt{2}}{2}\right)} \quad (5.2.10)$$

63%Ligand : 37%Metal

The same is done for the radical E functions in equations (5.2.5). When the $\varphi_{Erad(+)}$ function is used for the ligand set, the following molecular wavefunction is found

$$\Psi_{mol,E(+)} = \frac{\sqrt{3}}{3}r_1 - \frac{\sqrt{3}}{6}r_2 - \frac{\sqrt{3}}{6}r_3 + \frac{\sqrt{2}}{2}\phi_M \quad (5.2.11)$$

and the expected percentage contribution is

$$\frac{\left(\frac{\sqrt{3}}{3} + \frac{\sqrt{3}}{6} + \frac{\sqrt{3}}{6}\right)}{\left(\frac{\sqrt{3}}{3} + \frac{\sqrt{3}}{6} + \frac{\sqrt{3}}{6} + \frac{\sqrt{2}}{2}\right)} : \frac{\frac{\sqrt{2}}{2}}{\left(\frac{\sqrt{3}}{3} + \frac{\sqrt{3}}{6} + \frac{\sqrt{3}}{6} + \frac{\sqrt{2}}{2}\right)} \quad (5.2.12)$$

62%Ligand : 38%Metal

When the $\varphi_{Erad(-)}$ function is used for the ligand set, the molecular wavefunction is

$$\Psi_{mol,E(-)} = \frac{1}{2}r_2 - \frac{1}{2}r_3 + \frac{\sqrt{2}}{2}\phi_M \quad (5.2.13)$$

giving a slightly different percentage contribution of

$$\frac{\left(\frac{1}{2} + \frac{1}{2}\right)}{\left(\frac{1}{2} + \frac{1}{2} + \frac{\sqrt{2}}{2}\right)} : \frac{\frac{\sqrt{2}}{2}}{\left(\frac{1}{2} + \frac{1}{2} + \frac{\sqrt{2}}{2}\right)} \quad (5.2.14)$$

59%Ligand : 41%Metal

The basis for the ligand orbitals given in equations (5.2.4) and (5.2.5) assumes that no ligand-ligand overlap occurs. In real systems these orbitals are expected to overlap to some extent and the overlap of $r_1 r_2$, for example can be described as the two-atom overlap integral $S(r, r)$.^[170] The full calculations for the normalization of the ligand functions to include this overlap resulting in the new ligand basis, $\sigma_r(a)$, $\sigma_r(e_{(+)})$ and $\sigma_r(e_{(-)})$ can be found in Appendix .4 while the results are given below.

$$\sigma_r(a) = \frac{\sqrt{3}(r_1 + r_2 + r_3)}{3[1 + 2S(r, r)]^{1/2}} \quad (5.2.15)$$

$$\sigma_r(e_{(+)}) = \frac{\sqrt{6}(2r_1 - r_2 - r_3)}{6[1 - S(r, r)]^{1/2}} \quad (5.2.16)$$

$$\sigma_r(e_{(-)}) = \frac{\sqrt{2}(r_2 - r_3)}{2[1 - S(r, r)]^{1/2}} \quad (5.2.17)$$

The total group overlap integral for the overlap of the ligand and metal, $G = \int \Phi_M \sigma_{ligand} d\tau$, can now be evaluated for each basis, Appendix .5, and are given by

$$G_A(d_{z^2}, \sigma_r) = \frac{\sqrt{3}[S(d_{z^2}, r)]}{[1 + 2S(r, r)]^{1/2}} \quad (5.2.18)$$

$$G_{E_{(+)}}(d_{(xz/yz), (x^2-y^2/xy)}, \sigma_r) = \frac{2\sqrt{6}[S(d_{(xz/yz), (x^2-y^2/xy)}, r)]}{3[1 - S(r, r)]^{1/2}} \quad (5.2.19)$$

$$G_{E_{(-)}}(d_{(xz/yz), (x^2-y^2/xy)}, \sigma_r) = \frac{2[S(d_{(xz/yz), (x^2-y^2/xy)}, r)]}{[1 - S(r, r)]^{1/2}} \quad (5.2.20)$$

5.3 Experimental

The polymerisation of propylene at the unconventional catalyst $[(dpa)_3Ti]^+$ prompted an interest into the π -acid-base chemistry of the complex. To further investigate this a series of simplified complexes consisting of $[(dma)_3Ti]^+$, $(dma)_3TiH$ and $(dma)_3TiF$, where dma is the dimethylamido ligand were calculated. The analysis of the cationic species yields the basic orbital framework

at the metal centre; the hydride yields a pure σ -interaction with the basic frame, which will be consistent in principle for any axial ligand, while the fluoride represents a strong π -base in the axial position.

5.3.1 Computational Methods

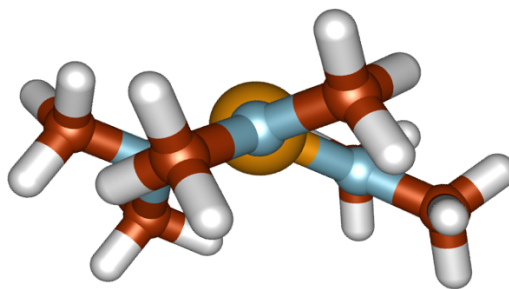
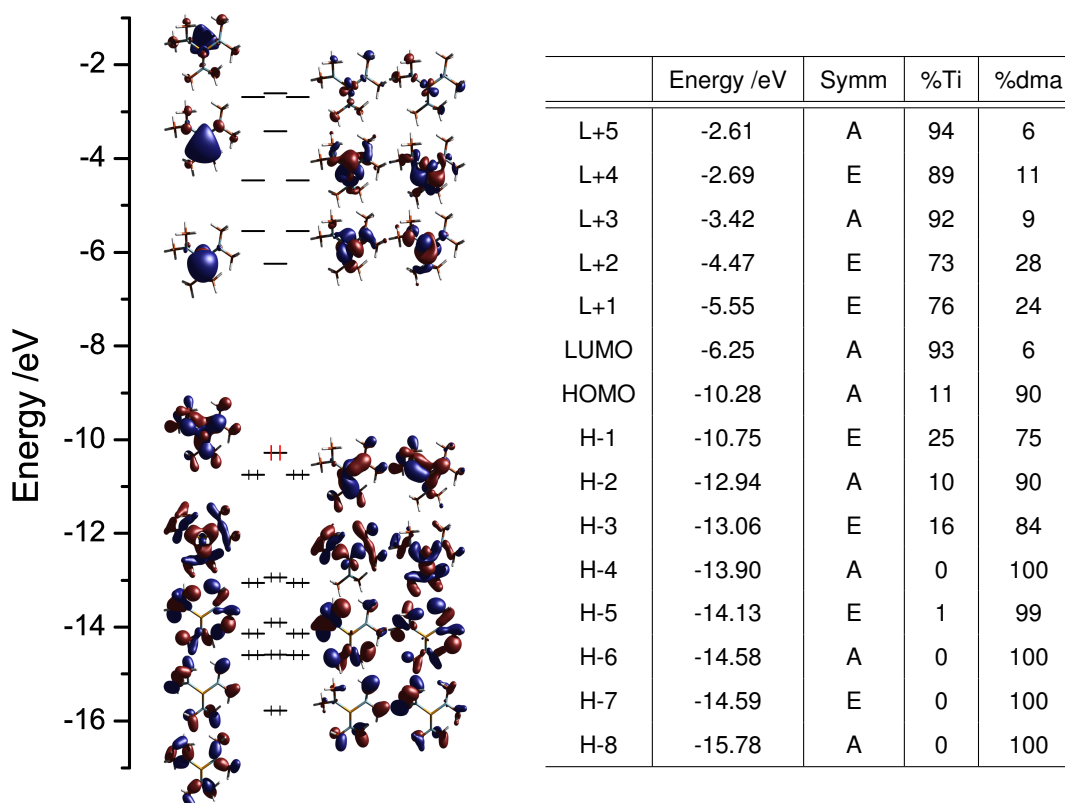
All gas phase calculations were carried out within the G03 suit^[104] using the B3LYP^[30,103] level of Density Functional Theory (DFT) with C_3 symmetry imposed. The basis set employed was LanL2DZ,^[38,40] the same as for the calculations in Chapters 2 and 4. Each stationary structure was confirmed as a local minimum *via* a frequency calculation which yielded no negative eigenvalues.

Orbital composition data were acquired through the use of the GaussSum 2.2^[106] software package. For each calculation, the molecule was divided into groups consisting of the metal centre, three dimethylamine groups and, where applicable, the hydrogen or fluorine atom. For simplicity, only the sum of the three dimethylamine groups is listed and not the individual compositions.

5.3.2 [(dma)₃Ti]⁺ (7)

The calculated structure of **7** as viewed down one of the N–Ti bonds is shown in Figure 5.8. A similar overall structure to **1** is noted although differences in both bond lengths and angles are seen. As in **1**, the alkyl groups on the nitrogen are canted into a propeller-wheel type arrangement and the bisection of the sum of the angles about nitrogen is not equivalent. No interaction between the titanium and the methyl substituent that is above the N₃ plane is seen for the dma ligand; however, the angle between the titanium, nitrogen and this carbon is considerably less than the Ti–N–C for the carbon lying below the N₃ plane having values of 115.85° and 131.80°, respectively.

The [(dma)₃Ti]⁺ system exhibits a large amount of mixing of the *s*, *p* and *d* metal basis orbitals as well as mixing of the *s* and *p* orbitals on the nitrogen atoms for all molecular orbitals. A portion of the calculated molecular orbital diagram is shown within Table 5.9 along with the percentage contributions from each of the groups to the total molecular orbital.

Figure 5.8: Calculated structure of $[(\text{dma})_3\text{Ti}]^+$, **7**Figure 5.9: $(\text{dma})_3\text{Ti}^+$ in C_3 symmetry

The LUMO which lies along the C_3 axis and is available for bonding to a fourth substituent is primarily metal based with 50% of the contribution from the metal due to the d_{z^2} orbital. The p_z orbital contributes 18%, while the s orbital makes up the remaining 32%.

The HOMO is primarily based on the nitrogen p_z orbitals while a smaller metal contribution, 11%, is made up of a nearly even mix of the d_{z^2} and p_z orbitals with a minimal contribution from the s orbital. The HOMO-1 and HOMO-3 E sets are both consistent with the $\text{N} \rightarrow \text{Ti}$ π or L type donation from the nitrogen p orbitals to the metal. The HOMO-1 orbital contains an interaction between the N p_z and Ti d_{xz} and d_{yz} orbitals, while the HOMO-2 consists of the interaction between N p_x/p_y and the Ti $d_{xy}/d_{x^2-y^2}$ orbitals. The HOMO-2 molecular orbital contains the N–Ti

σ interaction.

5.3.3 (dma)₃TiH (**8**)

The hydride species, (dma)₃TiH **8**, gives a model of a σ -only donor in the axial position of **7**. The calculated structure can be seen in Figure 5.10 with the molecular orbital diagram and orbital compositions given in Table 5.11.

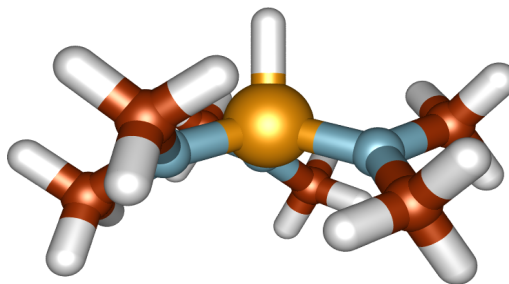


Figure 5.10: Calculated structure of (dma)₃TiH, **8**

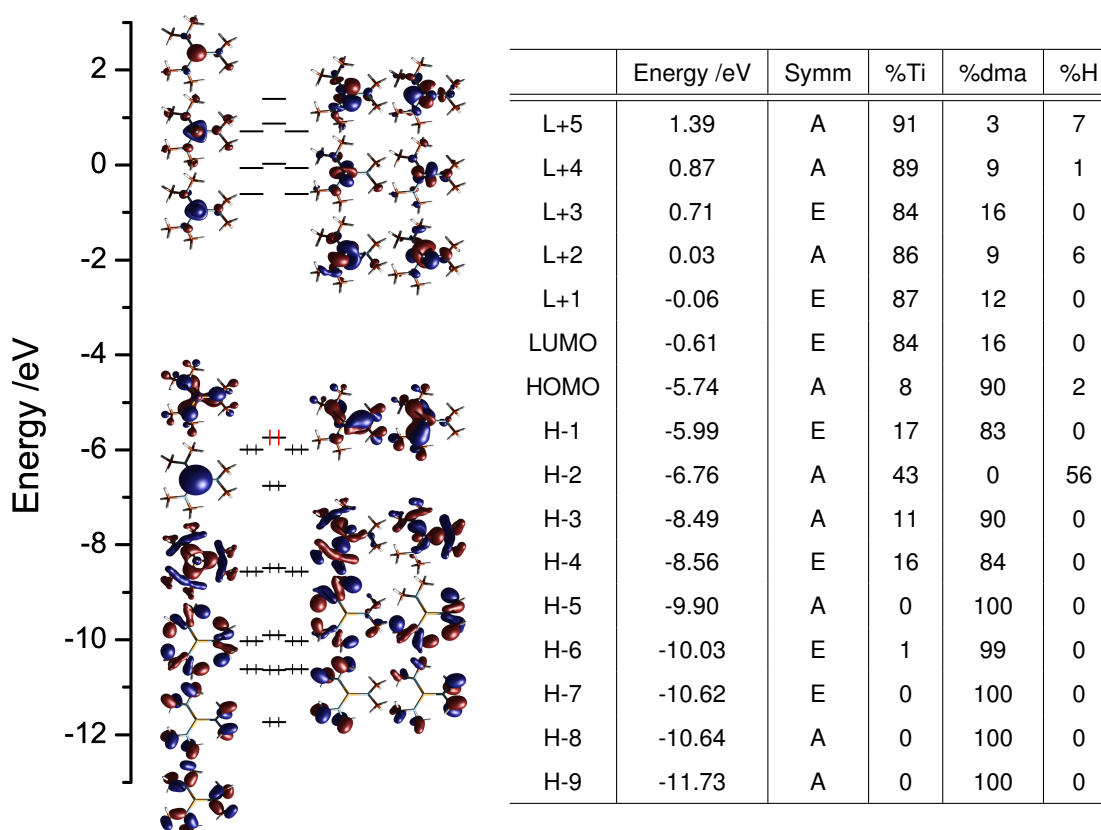


Figure 5.11: (dma)₃TiH in *C*₃ symmetry

The general structure and composition of the molecular orbitals for **8** are the same as those for **7** with the exception of the newly formed Ti–H σ bond. This bond is found in the new HOMO-

2 orbital where the hydrogen s orbital makes up 56% of the total composition. The remaining contribution from titanium has a make-up of 45% d_{z^2} , 31% s and 24% p_z . The HOMO and HOMO-1 are unchanged and the HOMO-2 and HOMO-3 orbitals of $[(dma)_3Ti]^+$ become the HOMO-3 and HOMO-4 orbitals respectively in $(dma)_3TiH$.

5.3.4 $(dma)_3TiF$ (**9**)

The axial ligand was also modelled as a fluorine atom which represents a strongly π -basic ligand. The resulting structure is shown in Figure 5.12 and the molecular orbital diagram with the orbital contributions found in Table 5.13.

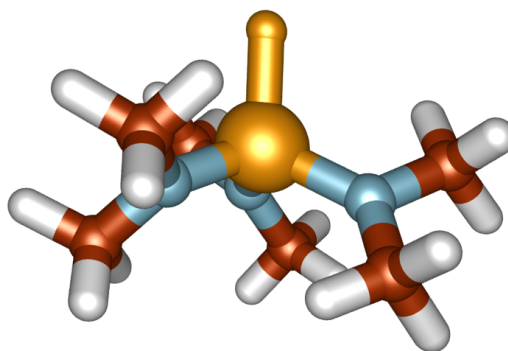
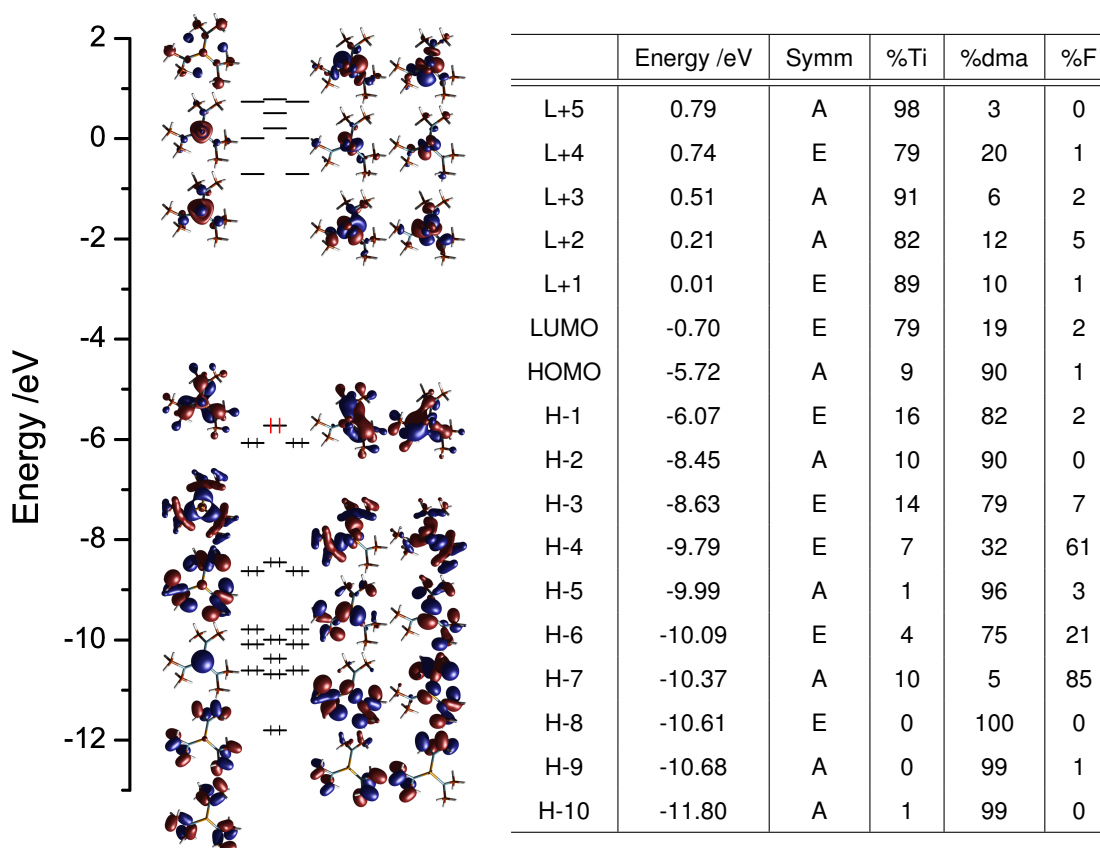


Figure 5.12: Calculated structure of $(dma)_3TiF$, **9**

The HOMO and HOMO-1 orbitals remain the same as in **8**. However a large drop is seen for the Ti–F σ interaction which is found at the new HOMO-7 level with the filled π orbitals of fluorine lying higher at the HOMO-4.

5.3.5 Trends

A distortion of the molecule is seen when either hydrogen or fluorine is added in the axial position effectively pushing back the dimethylamido ligands resulting in the contraction of the N–Ti–N bond angles and the displacement of titanium atom from the N_3 plane to increase. This displacement is only 0.795 Å in **7**, but is increased to 0.862 Å in **8**, and 1.144 Å in **9**. An increase in the Ti–N bond is also seen when a fourth substituent is added to **7**. This is to be expected for a formally cationic species and little difference in the Ti–N bond length can be seen between the hydride and fluoride complexes. The dimethylamido ligand shows no significant change in structure and remains planar for all three complexes with the sum of the angles around nitrogen

Figure 5.13: (dma)₃TiF in *C*₃ symmetry

remaining very close to 360°. Structural parameters are given in Table 5.4

	Ti–N /Å	N–Ti–N /°	Σ (N–Ti–N) /°	Ti displacement /Å	Σ (X–N–X) ^a /°
(dma) ₃ Ti ⁺	1.856	114.84	344.53	0.795	360.00
(dma) ₃ TiH	1.889	114.05	342.14	0.862	359.92
(dma) ₃ TiF	1.887	108.04	324.11	1.144	359.87

^a Sum of the three angles about nitrogen.

Table 5.4: Selected structural data for complexes **7**, **8** and **9**

For all three complexes only a small amount of the electron density in the filled molecular orbitals lies on the metal centre. The majority contribution of the calculated virtual orbitals however is attributed to the metal, further exhibiting its electron deficiency and resulting high π -acidity. The general make up of the metal orbital contribution consists of significant $s-p-d$ mixing for orbitals with *A* symmetry as well as $p-d$ mixing in *E* symmetry orbitals.

The calculated molecular orbital diagrams for all three species are given in Figure 5.14 and tracks the movement of the orbitals. A general destabilisation for nearly all the filled molecular orbitals is seen when moving from the cationic species, **7**, to the hydride, **8**, and no significant

change is observed in the HOMO or other previously occupied orbitals of the cation for the replacement of the hydrogen with a π -basic fluorine atom.

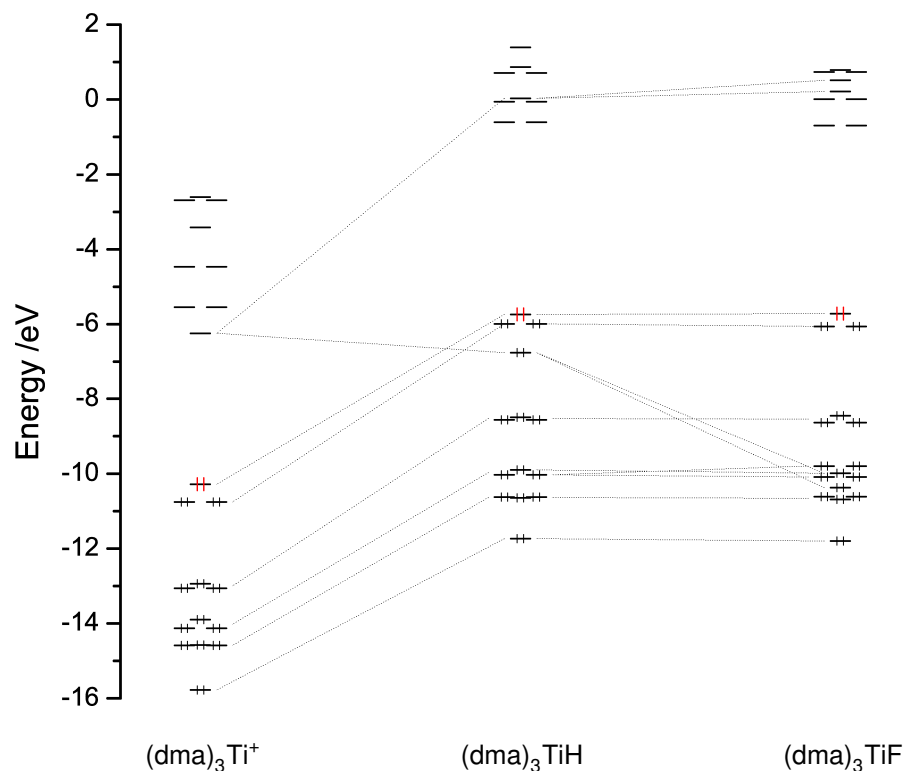


Figure 5.14: Molecular Orbital diagram for $(\text{dma})_3\text{TiX}$ where $X = +, \text{H}, \text{F}$

At the same time, the bonding interaction that is formed between the LUMO of **7** and the s orbital of hydrogen in the hydride is stabilized by 0.51 eV resulting in the new HOMO-2 orbital where the orbital contribution from the hydrogen is 56%. The σ interaction is further stabilized by 3.61 eV when the hydrogen is replaced by a fluorine atom resulting in the HOMO-7 orbital which has a 85% contribution from the fluorine atom. This drastic stabilization and change in composition can be explained by the relative electronegativity of the atoms involved in the bonding interaction and shows a transition from covalent to an increase in ionic bonding character. The electronegativity values for titanium, hydrogen and fluorine are 1.54, 2.20 and 3.98, respectively for the Pauling scale.^[171,172] An analysis of the calculated Mulliken atomic charges shows a marked decrease in charge on the titanium atom in **8**, characteristic of covalent character, followed by an increased charge in **9**. This change is plotted in Figure 5.15 with values found in Table 5.5.

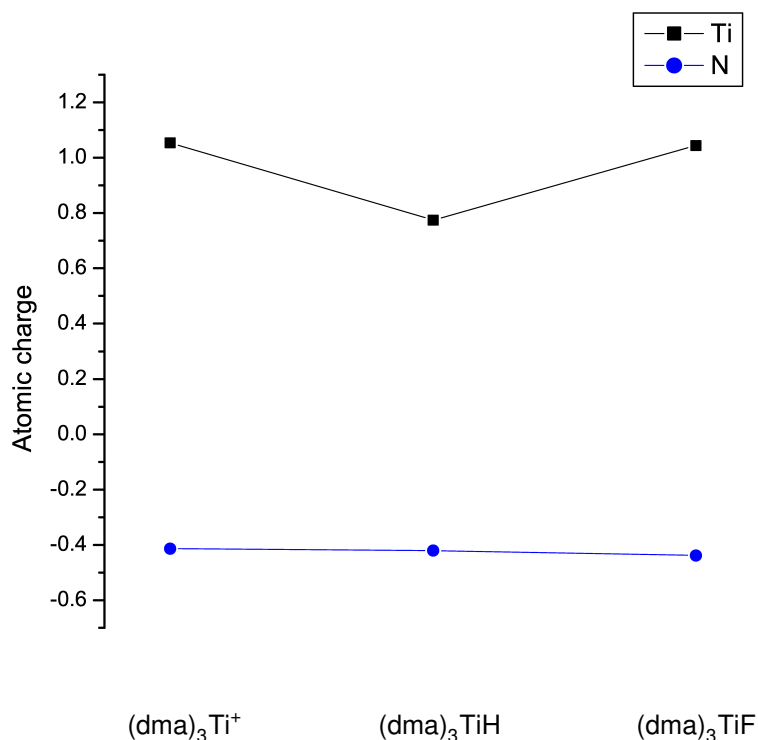


Figure 5.15: Change in the calculated Mulliken atomic charge for (dma)₃TiX where X = +, H, F

	Ti	N	X
(dma) ₃ Ti ⁺	1.0546	-0.4133	
(dma) ₃ TiH	0.7744	-0.4201	-0.1657
(dma) ₃ TiF	1.0444	-0.4382	-0.4459

Table 5.5: Calculated Mulliken atomic charges /|e|

5.4 Conclusions

The [(dma)₃Ti]⁺ complex is a simplified model of the highly Lewis acidic [(dpa)₃Ti]⁺ catalyst investigated in Chapter 3. The series including the cation, hydride and fluoride where the dimethylamido ligand was employed were calculated to see the effects of a σ donating ligand as well as an electron rich π -base. The σ interaction in the hydride complex was found to stabilise the LUMO of the cation which formed the bonding interaction by 0.51 eV while in the fluoride the total stabilisation of the bonding orbital was 4.12 eV. Along with the calculated Mulliken charges, this lowering in energy of the bonding interaction exemplifies the shift from the covalent nature of the Ti–H bond to the more ionic nature of the Ti–F bond.

Chapter 6

Conclusions and Suggestions for Future Work

6.1 Conclusions

Traditional Group IV Ziegler-Natta catalysts generally have the features of being cationic, 14-electron, d^0 metal centres with a metal-alkyl bond as well as a vacant orbital to accommodate the incoming olefin. The archetype for this type of catalyst is $[\text{Cp}_2\text{ZrCH}_3]^+$ which has a CBC classification of ML_4X_3^+ or ML_3X_4 neutral class. The currently accepted mechanisms for this type of polymerisation are the Cossée-Arlman and modified Green-Rooney mechanisms, which can be seen in Section 2.2 of Chapter 2.

A set of systems of type $[(\text{R}_2\text{N})_3\text{Ti}]^+$, have a CBC classification of ML_3X_3^+ or ML_2X_4 neutral class giving d^0 , 12-electron species that contain both the necessary positive charge as well as a vacant site. Systems of type $(\text{R}_2\text{N})_3\text{TiCH}_3$ are also d^0 , with a CBC classification of ML_3X_4 and are 14-electron systems, which contain a metal-alkyl bond. While a positively charged species and the structural features needed for conventional Ziegler-Natta catalysis are present within the total *trisamido* titanium platform, they occur in two separate species. The former of these two contains an even more electron deficient metal centre than the archetype and a vacant site for complexation of monomer but lacks the metal-alkyl bond traditionally necessary for insertion. The latter exhibits a metal-alkyl bond and the expected CBC classification without the positive charge or vacant site

although a rearrangement changing the geometry at the metal centre from pseudo-tetrahedral to pseudo-trigonal bipyramidal could be theorized in order to provide such a site.

Experimental studies^[62,63] have shown that systems of type $[(R_2N)_3Ti]^+[B(C_6F_5)_4]^-$ polymerise propylene *via* a pseudo-first order reaction. Similarly, polymerisation occurs when $(R_2N)_3TiCH_3$ is aided by a co-catalyst; however, no reaction occurs when the $(R_2N)_3TiCH_3$ system is used without an activation catalyst present. This lack of polymerisation suggests that the geometry rearrangement as suggested above does not occur.

A possible mechanism for the non-traditional Ziegler-Natta catalyst $[(dpa)_3Ti]^+$ (**1**) was presented in Chapter 3 and is shown pictorially in Figure 6.1.

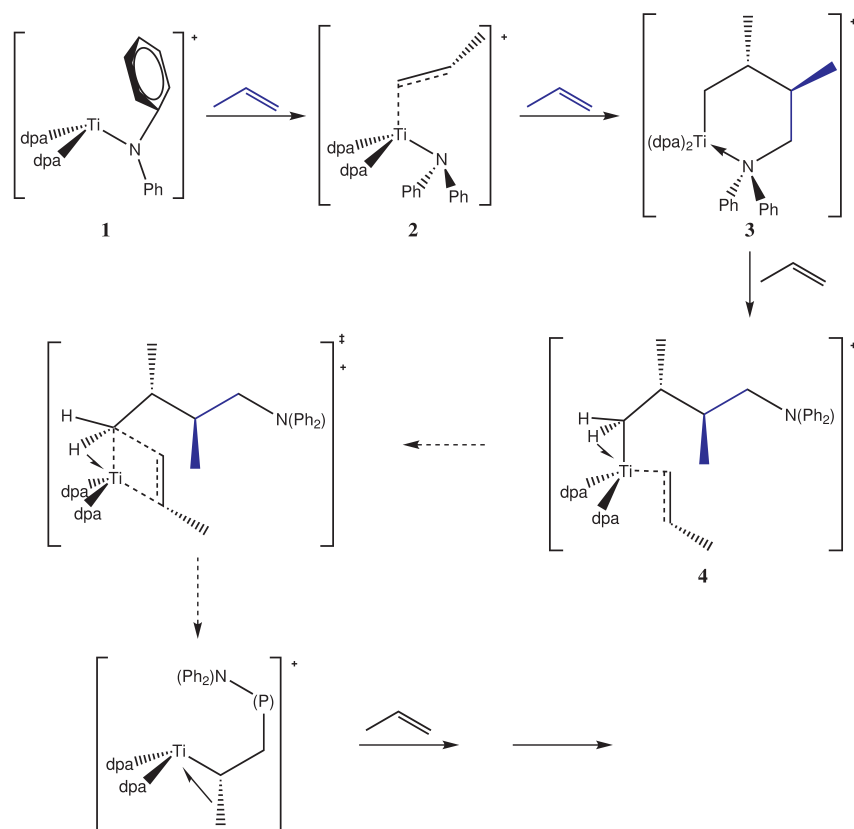


Figure 6.1: Expected mechanism for the polymerisation of propylene at **1**

The adduct of propylene with **1**, $[(dpa)_3Ti-C_3H_6]^+$ (**2**), and other selected species were calculated to elucidate the mechanism of this unconventional, yet catalytically active complex. An unusual intermediate was found to form when a second propylene group was calculated with the adduct. The intermediate consists of a hetero-metallo-cyclo made up of the titanium centre, the nitrogen of one of the ligands, and at least one of carbons from the propylene moiety of the adduct along with two carbons from the incoming propylene. This intermediate was the focus of Chapter

4 where a variety of possible conformations resulting from several different pathways were explored. The lowest energy structure which was chosen as the model and is labelled **3** in Figure 6.1. However, it should be noted that the study in Chapter 4 was not able to conclusively rule out several other potential isomers for the intermediate and further work regarding this is suggested below.

When a third propylene was added to model the continued propagation of the polymerisation reaction, a similar adduct to that found for the first addition was found although one of the amido ligands has now been replaced with an alkyl group thus giving the expected structural requirements of conventional Ziegler-Natta catalysis although with an unconventional, more Lewis acidic metal centre. The continued insertion and propagation steps are expected to conform to the generally accepted modified Green-Rooney mechanism as outlined in Figure 6.1 where (P) in the last structure denotes the growing polymer chain.

Chapter 5 then probed the π -acid-base chemistry of $[(\text{dma})_3\text{Ti}]^+$, where R = dimethylamido, which is a simplified model of **1**. Along with the cation which represents the basic orbital framework for the metal complex, the hydride, $(\text{dma})_3\text{TiH}$, and fluoride, $(\text{dma})_3\text{TiF}$, were also calculated to simulate a pure σ -interaction and a strong π -base, respectively. The σ interaction in the hydride complex was found to stabilise the LUMO of the cation when forming the bonding interaction by 0.51 eV while in the fluoride the total stabilisation of the bonding orbital was 4.12 eV. Along with the calculated Mulliken charges, this lowering in energy of the bonding interaction exemplifies the shift from the covalent nature of the Ti–H bond to the more ionic nature of the Ti–F bond.

6.2 Suggestions for Further Work

It would be interesting to further study the possible intermediates of the polymerisation reaction. Due to a small energy difference, several of the structures found in Chapter 4 might be expected to be energetically accessible and the lowest energy structure can not conclusively be said to be the only intermediate occurring in the mechanism. To further differentiate the possibilities, a study of the potential energy surface for the formation of each of the conformers could be undertaken in order to determine the expected energy barrier. A study for the addition of the second propylene moiety and subsequent insertion would also be helpful in order to find the lowest energy pathway.

It is also possible that a number of competing pathways may be taking place at the same time which would result in a mixture of products experimentally. Once several pathways are calculated, the results could then be compared with structural data taken from experimental studies to confirm the mechanism. Experimental checks could be achieved through the use of Nuclear Magnetic Resonance Spectroscopy, Mass Spectrometry and Gel Permeation Chromatography to identify the group at the end of the polymer chain, tacticity as well as other physical properties of the resultant polymer.

A further suggestion for future work is the reaction with ethylene. While **1** polymerises propylene, experimental studies have shown that an analogous reaction with ethylene does not occur.^[62,63] It would be interesting to calculate similar species with ethylene for comparison as well as to find a reason for the selected activity of the catalyst.

Bibliography

- [1] *Year Million: Science at the Far Edge of Knowledge*; Broderick, D., Ed.; ATLAS and CO, 2008.
- [2] Atkins, P.; de Paula, J. *Physical Chemistry*, Seventh ed.; W. H. Freeman and Company, 2002.
- [3] House, J. *Fundamentals of Quantum Chemistry*, 2nd ed.; Elsevier Academic Press, 2004.
- [4] Levine, I. N. *Quantum Chemistry*, 4th ed.; Prentice Hall, 1991.
- [5] Rayleigh, *Philosophical Magazine Series 5* **1900**, 539–540.
- [6] Chang, R. *Physical Chemistry for the Chemical and Biological Sciences*, 3rd ed.; University Science Books, 2000.
- [7] Martinson, I.; Curtis, L. *Nuclear Instruments and Methods in Physics Research Section B: Beam Interactions with Materials and Atoms* **2005**, 235, 17 – 22, The Physics of Highly Charged Ions.
- [8] Mohr, P. J.; Taylor, B. N. *Revs. Mod. Phys.* **2000**, 351.
- [9] Thomson, J. J. *Philosophical Magazine Series 5* **1897**, 44, 293–316.
- [10] Rutherford, E. *Philosophical Magazine Series 6* **1911**, 21, 669–688.
- [11] Bohr, N. *Philosophical Magazine Series 6* **1913**, 25, 10–31.
- [12] Simons, J. *An Introduction to Theoretical Chemistry*; Cambridge University Press, 2003.
- [13] Davisson, C.; Germer, L. H. *Phys. Rev.* **1927**, 30, 705–740.

- [14] Atkins, P. W. *Molecular Qunatum Mechanics*, 2nd ed.; Oxford University Press, 1983.
- [15] Cramer, C. J. *Essentials of Computational Chemistry, Theories and Models*; Wiley, 2004.
- [16] Foresman, J. B.; Frisch, A. E. *Exploring Chemistry with Electronic Structure Methods*, 2nd ed.; Gaussian Inc, 1996.
- [17] Szabo, A.; Ostlund, N. S. *Modern Quantum Chemistry, Introduction to Advanced Electronic Structure Theory*; Dover, 1996.
- [18] IUPAC. *Compendium of Chemical Terminology*; McNaught, A. D.; Wilkinson, A., Eds.; Blackwell Scientific Publications, Oxford, 1997.
- [19] Pauli, W. *Phys. Rev.* **1940**, *58*, 716–722.
- [20] Nesbet, R. K. *Proceedings of the Royal Society of London. Series A, Mathematical and Physical Sciences* **1955**, *230*, pp. 312–321.
- [21] Inc., G. *G03 Manual*, 2003.
- [22] Pople, J. A.; Head-Gordon, M.; Raghavachari, K. *The Journal of Chemical Physics* **1987**, *87*, 5968–5975.
- [23] Møller, C.; Plesset, M. S. *Physical Review* **1934**, *46*, 618–622.
- [24] Teller, E. *Rev. Mod. Phys.* **1962**, *34*, 627–631.
- [25] Koch, W.; Holthausen, M. C. *A Chemist's Guide to Density Functional Theory*, 2nd ed.; Wiley-VCH, 2000.
- [26] Slater, J. C. *Phys. Rev.* **1951**, *81*, 385–390.
- [27] Hohenberg, P.; Kohn, W. *Phys. Rev.* **1964**, *136*, B864–B871.
- [28] Kohn, W.; Sham, L. J. *Phys. Rev.* **1965**, *140*, A1133–A1138.
- [29] Vosko, S. H.; Wilk, L.; Nusair, M. *Canadian Journal of Physics* **1980**, *58*, 1200–1211.
- [30] Lee, C.; Yang, W.; Parr, R. G. *Phys. Rev. B* **1988**, *37*, 785–789.
- [31] McLean, A. D.; Chandler, G. S. *The Journal of Chemical Physics* **1980**, *72*, 5639–5648.

- [32] Krishnan, R.; Binkley, J. S.; Seeger, R.; Pople, J. A. *The Journal of Chemical Physics* **1980**, 72, 650–654.
- [33] Treitel, N.; Shenhar, R.; Aprahamian, I.; Sheradsky, T.; Rabinovitz, M. *Phys. Chem. Chem. Phys.* **2004**, 6, 1113–1121.
- [34] Chandrasekhar, J.; Andrade, J. G.; Schleyer, P. v. R. *Journal of the American Chemical Society* **1981**, 103, 5609–5612.
- [35] Kollmar, H. *Journal of the American Chemical Society* **1978**, 100, 2665–2669.
- [36] Clark, T.; Chandrasekhar, J.; Psitznagel, G. W.; von Ragué Schleyer, P. *Journal of Computational Chemistry* **1983**, 4, 294–301.
- [37] Check, C. E.; Faust, T. O.; Bailey, J. M.; Wright, B. J.; Gilbert, T. M.; Sunderlin, L. S. *J. Phys. Chem. A* **2001**, 105, 8111–8116.
- [38] Hay, P. J.; Wadt, W. R. *The Journal of Chemical Physics* **1985**, 82, 299–310.
- [39] Hay, P. J.; Wadt, W. R. *The Journal of Chemical Physics* **1985**, 82, 270–283.
- [40] Wadt, W. R.; Hay, P. J. *The Journal of Chemical Physics* **1985**, 82, 284–298.
- [41] Friedrich, M. E. P.; Marvel, C. S. *Journal of the American Chemical Society* **1930**, 52, 376–384.
- [42] Boor, J. *Ziegler-Natta Catalysts and Polymerizations*; Academic Press, 1979.
- [43] Natta, G. *Journal of Inorganic and Nuclear Chemistry* **1958**, 8, 589 – 611, Proceedings International Symposium on the Chemistry of the Co-ordination Compounds.
- [44] Natta, G.; P.Pino.; G.Mazzanti.; U.Giannini, *Journal of the American Chemical Society* **1957**, 79, 2975–2976.
- [45] Elschenbroich, C.; Salzer, A. *Organometallics*, 2nd ed.; VCH Publishers, 1992.
- [46] Shelden, R. A.; Fueno, T.; Tsunetsugu, T.; Furukawa, J. *Journal of Polymer Science Part B: Polymer Letters* **1965**, 3, 23–26.
- [47] Bovey, F. A.; Tiers, G. V. D. *Journal of Polymer Science* **1960**, 44, 173–182.

- [48] <http://nobelprize.org>.
- [49] Kaminsky, W.; Külper, K.; Brintzinger, H. H.; Wild, F. R. W. P. *Angewandte Chemie International Edition in English* **1985**, *24*, 507–508.
- [50] Chen, E. Y.; Marks, T. J. *Chemical Reviews* **2000**, *100*, 1391–1434.
- [51] Mason, M. R.; Smith, J. M.; Bott, S. G.; Barron, A. R. *Journal of the American Chemical Society* **1993**, *115*, 4971–4984.
- [52] Apblett, A.; Warren, A.; Barron, A. R. *Chemical Materials* **1992**, *4*, 167.
- [53] Zurek, E.; Ziegler, T. *Progress in Polymer Science* **2004**, *29*, 107 – 148.
- [54] Yang, X.; Stern, C. L.; Marks, T. J. *Journal of the American Chemical Society* **1991**, *113*, 3623–3625.
- [55] Yang, X.; Stern, C. L.; Marks, T. J. *Journal of the American Chemical Society* **1994**, *116*, 10015–10031.
- [56] Ewen, J.; Elder, M. *European Patent*, 1991, 0427697.
- [57] Ewen, J.; Elder, M. *European Patent*, 1996, 5561092.
- [58] Li, L.; Marks, T. J. *Organometallics* **1998**, *17*, 3996–4003.
- [59] Chen, Y.-X.; Stern, C. L.; Yang, S.; Marks, T. J. *Journal of the American Chemical Society* **1996**, *118*, 12451–12452.
- [60] Li, L.; Stern, C. L.; Marks, T. J. *Organometallics* **2000**, *19*, 3332–3337.
- [61] Jia, L.; Yang, X.; Stern, C. L.; Marks, T. J. *Organometallics* **1997**, *16*, 842–857.
- [62] Williams, T. N. Ph.D. thesis, University of Sussex, 2010.
- [63] Blanchard, M. Ph.D. thesis, University of Tennessee, 2007.
- [64] Cossee, P. *Journal of Catalysis* **1964**, *3*, 80 – 88.
- [65] Arlman, E. J. *Journal of Catalysis* **1964**, *3*, 89 – 98.
- [66] Arlman, E. J.; Cossee, P. *Journal of Catalysis* **1964**, *3*, 99 – 104.

- [67] Ivin, K. J.; Rooney, J. J.; Stewart, C. D.; Green, M. L. H.; Mahtab, R. *J. Chem. Soc., Chem. Commun.* **1978**, 604–606.
- [68] Brookhart, M.; Green, M. L. *Journal of Organometallic Chemistry* **1983**, *250*, 395 – 408.
- [69] Piers, W. E.; Bercaw, J. E. *Journal of the American Chemical Society* **1990**, *112*, 9406–9407.
- [70] C. Green, *J. Chem. Soc. Rev.* **1998**, *27*, 263–272.
- [71] Green, M. L. H. *Journal of Organometallic Chemistry* **1995**, *500*, 127 – 148.
- [72] Woo, T. K.; Margl, P. M.; Lohrenz, J. C. W.; Blöchl, P. E.; Ziegler, T. *Journal of the American Chemical Society* **1996**, *118*, 13021–13030.
- [73] Lohrenz, J. C. W.; Woo, T. K.; Ziegler, T. *Journal of the American Chemical Society* **1995**, *117*, 12793–12800.
- [74] Resconi, L.; Cavallo, L.; Fait, A.; Piemontesi, F. *Chemical Reviews* **2000**, *100*, 1253–1346.
- [75] Woo, T. K.; Fan, L.; Ziegler, T. *Organometallics* **1994**, *13*, 2252–2261.
- [76] Margl, P.; Deng, L.; Ziegler, T. *Topics in Catalysis* **1999**, *7*, 187–208, 10.1023/A:1019176119849.
- [77] Armstrong, D. R.; Perkins, P. G.; Stewart, J. J. P. *J. Chem. Soc., Dalton Trans.* **1972**, 1972–1980.
- [78] Novaro, O.; Blaisten-Barojas, E.; Clementi, E.; Giunchi, G.; Ruiz-Vizcaya, M. E. *The Journal of Chemical Physics* **1978**, *68*, 2337–2351.
- [79] Kawamura-Kuribayashi, H.; Koga, N.; Morokuma, K. *Journal of the American Chemical Society* **1992**, *114*, 2359–2366.
- [80] Woo, T. K.; Margl, P. M.; Ziegler, T.; Blöchl, P. E. *Organometallics* **1997**, *16*, 3454–3468.
- [81] Margl, P.; Lohrenz, J. C. W.; Ziegler, T.; Blöchl, P. E. *Journal of the American Chemical Society* **1996**, *118*, 4434–4441.
- [82] Fan, L.; Harrison, D.; Woo, T. K.; Ziegler, T. *Organometallics* **1995**, *14*, 2018–2026.

- [83] Margl, P.; Deng, L.; Ziegler, T. *Journal of the American Chemical Society* **1998**, *120*, 5517–5525.
- [84] Tobisch, S.; Ziegler, T. *Journal of the American Chemical Society* **2004**, *126*, 9059–9071, PMID: 15264839.
- [85] Fan, L.; Harrison, D.; Deng, L.; Woo, T. K.; Swerhone, D.; Ziegler, T. *Canadian Journal of Chemistry* **1995**, *73*, 989–998.
- [86] Woo, T. K.; Fan, L.; Ziegler, T. *Organometallics* **1994**, *13*, 432–433.
- [87] Meier, R. J.; van Doremaele, G. H. J.; Iarlori, S.; Buda, F. *Journal of the American Chemical Society* **1994**, *116*, 7274–7281.
- [88] Yoshida, T.; Koga, N.; Morokuma, K. *Organometallics* **1995**, *14*, 746–758.
- [89] Weiss, H.; Ehrig, M.; Ahlrichs, R. *Journal of the American Chemical Society* **1994**, *116*, 4919–4928.
- [90] Bierwagen, E. P.; Bercaw, J. E.; Goddard, W. A. *Journal of the American Chemical Society* **1994**, *116*, 1481–1489.
- [91] Graf, M.; Angermund, K.; Fink, G.; Thiel, W.; Jensen, V. R. *Journal of Organometallic Chemistry* **2006**, *691*, 4367 – 4378, <ce:title>Theory and Mechanistic Studies</ce:title>.
- [92] SaB mannshausen, J.; Track, A.; Dias, T. A. D. S. *European Journal of Inorganic Chemistry* **2007**, *2007*, 2327–2333.
- [93] Chan, M. S. W.; Vanka, K.; Pye, C. C.; Ziegler, T. *Organometallics* **1999**, *18*, 4624–4636.
- [94] Vanka, K.; Xu, Z.; Seth, M.; Ziegler, T. *Topics in Catalysis* **2005**, *34*, 143–164, 10.1007/s11244-005-3807-3.
- [95] Vanka, K.; Chan, M. S. W.; Pye, C. C.; Ziegler, T. *Organometallics* **2000**, *19*, 1841–1849.
- [96] Lanza, G.; FragaIÃ , I. L.; Marks, T. J. *Organometallics* **2002**, *21*, 5594–5612.
- [97] Fusco, R.; Longo, L.; Proto, A.; Masi, F.; Garbassi, F. *Macromolecular Rapid Communications* **1998**, *19*, 257–262.

- [98] Bernardi, F.; Bottoni, A.; Miscione, G. P. *Organometallics* **1998**, *17*, 16–24.
- [99] Vanka, K.; Ziegler, T. *Organometallics* **2001**, *20*, 905–913.
- [100] Vanka, K.; Xu, Z.; Ziegler, T. *Macromolecular Symposia* **2004**, *213*, 275–286.
- [101] Xu, Z.; Vanka, K.; Ziegler, T. *Macromolecular Symposia* **2004**, *206*, 457–470.
- [102] Yang, S.-Y.; Ziegler, T. *Organometallics* **2006**, *25*, 887–900.
- [103] Becke, A. D. *The Journal of Chemical Physics* **1993**, *98*, 5648–5652.
- [104] Frisch, M. J. et al. *Gaussian 03, Revision D.01*, Gaussian, Inc., Wallingford, CT, 2004.
- [105] Frisch, M. J. et al. *Gaussian 09 Revision B.1*, Gaussian Inc. Wallingford CT 2010.
- [106] O'Boyle, N. M.; Tenderholt, A. L.; Langner, K. M. *Journal of Computational Chemistry* **2008**, *29*, 839–845.
- [107] *Comprehensive Organometallic Chemistry III*; Parkin, G., Ed.; Elsevier, 2006.
- [108] Sauriol, F.; Wong, E.; Leung, A.; Donaghue, I.; Baird, M.; Wondimagegn, T.; Ziegler, T. *Angewandte Chemie International Edition* **2009**, *48*, 3342–3345.
- [109] Bassi, I. W.; Allegra, G.; Scordamaglia, R.; Chioccola, G. *Journal of the American Chemical Society* **1971**, *93*, 3787–3788.
- [110] Davies, G.; Jarvis, J. A. J.; Kilbourn, B. T. *Chemical Communications* **1971**, 1511–1512.
- [111] Allen, F. H.; Motherwell, W. D. S. *Acta. Cryst* **2002**, *B58*, 407–422.
- [112] Bruno, I. J.; Cole, J. C.; Edgington, P. R.; Kessler, M.; Macrae, C. F.; McCabe, P.; Pearson, J.; Taylor, R. *Acta. Cryst* **2002**, *B58*, 389–397.
- [113] Putzer, M. A.; Neumüller, B.; Dehnicke, K. *Zeitschrift für anorganische und allgemeine Chemie* **1998**, *624*, 929–930.
- [114] Pellecchia, C.; Immirzi, A.; Pappalardo, D.; Peluso, A. *Organometallics* **1994**, *13*, 3773–3775.
- [115] David R. Lide, J.; Christensen, D. *The Journal of Chemical Physics* **1961**, *35*, 1374–1378.

- [116] Zimmerman, H. E.; Traxler, M. D. *Journal of the American Chemical Society* **1957**, *79*, 1920–1923.
- [117] Haaland, A.; Scherer, W.; Ruudand, K.; McGrady, G. S.; Downs, A. J.; Swang, O. *Journal of the American Chemical Society* **1998**, *120*, 3762–3772.
- [118] Bradley, D. C.; Chudzynska, H.; Backer-Dirks, J. D.; Hursthouse, M. B.; Ibrahim, A. A.; Motevalli, M.; Sullivan, A. C. *Polyhedron* **1990**, *9*, 1423 – 1427.
- [119] Guzei, I. A.; Stockland, R. A.; Jordan, R. F. *Acta Crystallographica Section C* **2000**, *56*, 635–636.
- [120] Liu, Z.; Landis, E. S. C. R. *Journal of the American Chemical Society* **2001**, *123*, 2915–2916.
- [121] Kilgore, U. J.; Basuli, F.; Huffman, J. C.; Mindiola, D. J. *Inorganic Chemistry* **2006**, *45*, 487–489, PMID: 16411677.
- [122] Cahn, R. S.; Ingold, C.; Prelog, V. *Angewandte Chemie International Edition in English* **1966**, *5*, 385–415.
- [123] Prelog, V.; Helmchen, G. *Angewandte Chemie International Edition in English* **1982**, *21*, 567–583.
- [124] Booth, H.; Everett, J. R. *J. Chem. Soc., Chem. Commun.* **1976**, 278–279.
- [125] Squillacote, M. E.; Neth, J. M. *Journal of the American Chemical Society* **1987**, *109*, 198–202.
- [126] Buchanan, G.; Webb, V. *Tetrahedron Letters* **1983**, *24*, 4519 – 4520.
- [127] March, J. *Advanced Organic Chemistry: Reactions, Mechanisms and Structure*, 4th ed.; John Wiley & Sons, 1992; and references therein.
- [128] L. G. Wade, J. *Organic Chemistry*, Fifth Edition ed.; Pearson Education, Inc, 2003.
- [129] Willy, W. E.; Binsch, G.; Eliel, E. L. *Journal of the American Chemical Society* **1970**, *92*, 5394–5402.

- [130] Lipnick, R. L. *Journal of Molecular Structure* **1974**, *21*, 423 – 436.
- [131] McKnight, A. L.; Waymouth, R. M. *Chemical Reviews* **1998**, *98*, 2587–2598, PMID: 11848972.
- [132] Gibson, V. C.; Spitzmesser, S. K. *Chemical Reviews* **2003**, *103*, 283–316.
- [133] Laplaza, C. E.; Cummins, C. C. *Science* **1995**, *268*, 861.
- [134] Laplaza, C. E.; Odom, A. L.; Davis, W. M.; Cummins, C. C.; Protasiewicz, J. D. *Journal of the American Chemical Society* **1995**, *117*, 4999–5000.
- [135] Lappert, M.; Power, P.; Protchenko, A.; Seeber, A. *Metal Amide Chemistry*; Wiley, 2009.
- [136] Dermer, O. C.; Ferneliuss, W. C. *Zeitschrift für anorganische und allgemeine Chemie* **1934**, *221*, 83–96.
- [137] Bürger, H.; Wannagat, U. *Monatshefte für Chemie / Chemical Monthly* **1963**, *94*, 1007–1012.
- [138] Bürger, H.; Wannagat, U. *Monatshefte für Chemie / Chemical Monthly* **1964**, *95*, 1099–1102.
- [139] Bradley, D. C.; Chisholm, M. H. *Accounts of Chemical Research* **1976**, *9*, 273–280.
- [140] Eller, P. G.; Bradley, D. C.; Hursthouse, M. B.; Meek, D. W. *Coordination Chemistry Reviews* **1977**, *24*, 1 – 95.
- [141] Davidson, P. J.; Lappert, M. F.; Pearce, R. *Accounts of Chemical Research* **1974**, *7*, 209–217.
- [142] Barker, G.; Lappert, M. *Journal of Organometallic Chemistry* **1974**, *76*, C45 – C46.
- [143] Davidson, P. J.; Harris, D. H.; Lappert, M. F. *J. Chem. Soc., Dalton Trans.* **1976**, 2268–2274.
- [144] Cotton, J. D.; Davidson, P. J.; Lappert, M. F. *J. Chem. Soc., Dalton Trans.* **1976**, 2275–2286.
- [145] Cotton, J. D.; Davidson, P. J.; Lappert, M. F.; Donaldson, J. D.; Silvet, J. *J. Chem. Soc., Dalton Trans.* **1976**, 2286–2290.
- [146] Barker, G. K.; Lappert, M. F.; Howard, J. A. K. *J. Chem. Soc., Dalton Trans.* **1978**, 734–740.

- [147] Gudat, D.; Verkade, J. G. *Organometallics* **1989**, *8*, 2772–2779.
- [148] Naiini, A. A.; Menge, W. M. P. B.; Verkade, J. G. *Inorganic Chemistry* **1991**, *30*, 5009–5012.
- [149] Plass, W.; Verkade, J. G. *Journal of the American Chemical Society* **1992**, *114*, 2275–2276.
- [150] Cummins, C. C.; Lee, J.; Schrock, R. R.; Davis, W. D. *Angewandte Chemie International Edition in English* **1992**, *31*, 1501–1503.
- [151] Cummins, C. C.; Schrock, R. R.; Davis, W. M. *Angewandte Chemie International Edition in English* **1993**, *32*, 756–759.
- [152] Cummins, C. C.; Schrock, R. R.; Davis, W. M. *Inorganic Chemistry* **1994**, *33*, 1448–1457.
- [153] Freundlich, J. S.; Schrock, R. R.; Cummins, C. C.; Davis, W. M. *Journal of the American Chemical Society* **1994**, *116*, 6476–6477.
- [154] Kol, M.; Schrock, R. R.; Kempe, R.; Davis, W. M. *Journal of the American Chemical Society* **1994**, *116*, 4382–4390.
- [155] Zanetti, N. C.; Schrock, R. R.; Davis, W. M. *Angewandte Chemie International Edition in English* **1995**, *34*, 2044–2046.
- [156] Schrock, R. R. *Accounts of Chemical Research* **1997**, *30*, 9–16.
- [157] O'Donoghue, M. B.; Davis, W. M.; Schrock, R. R. *Inorganic Chemistry* **1998**, *37*, 5149–5158.
- [158] Yandulov, D. V.; Schrock, R. R. *Science* **2003**, *301*, 76.
- [159] C. Cummins, C. *Chem. Commun.* **1998**, 1777–1786.
- [160] Palacios, A. A.; Alemany, P.; Alvarez, S. *Inorganic Chemistry* **1999**, *38*, 707–715.
- [161] Alvarez, S. *Coordination Chemistry Reviews* **1999**, *193-195*, 13 – 41.
- [162] Rossi, A. R.; Hoffmann, R. *Inorganic Chemistry* **1975**, *14*, 365–374.
- [163] Hagen, K.; Holwill, C. J.; Rice, D. A.; Runnacles, J. D. *Inorganic Chemistry* **1988**, *27*, 2032–2035.

- [164] Chisholm, M. H.; Hammond, C. E.; Huffman, J. C. *Polyhedron* **1988**, 7, 2515 – 2520.
- [165] Fan, M.; Duesler, E.; Janik, J.; Paine, R. *Journal of Inorganic and Organometallic Polymers and Materials* **2007**, 17, 423–437, 10.1007/s10904-007-9125-4.
- [166] Schomaker, V.; Stevenson, D. P. *Journal of the American Chemical Society* **1941**, 63, 37–40.
- [167] Andersen, R. A.; Beach, D. B.; Jolly, W. L. *Inorganic Chemistry* **1985**, 24, 4741–4743.
- [168] Green, J. C.; Payne, M.; Seddon, E. A.; Andersen, R. A. *J. Chem. Soc., Dalton Trans.* **1982**, 887–892.
- [169] Harris, D. C.; Bertolucci, M. D. *Symmetry and Spectroscopy: An Introduction to Vibrational and Electronic Spectroscopy*; Dover Publications Inc., 1989.
- [170] Ballhausen, C. J.; Gray, H. B. *Molecular Orbital Theory: An Introductory Lecture Note and Reprint volume*; W. A. Benjamin, Inc, 1965.
- [171] Pauling, L. *The Nature of the Chemical Bond*, 3rd ed.; Cornell Univ., 1960.
- [172] A.L.; Allred, *Journal of Inorganic and Nuclear Chemistry* **1961**, 17, 215 – 221.

Appendices

Appendix A

.1 Projection operators

Application of the projection operator of the radial function onto A

$$\begin{aligned}
 \varphi_{A_{rad}} &= \hat{P}_{(\phi_X)}(r) \cdot A \\
 &= r_1(1) + r_2(1) + r_3(1) \\
 \varphi_{A_{rad}} &\simeq r_1 + r_2 + r_3
 \end{aligned} \tag{.1.1}$$

Application of the projection operator of the radial function onto E

$$\begin{aligned}
 \varphi_{E_{rad}(\pm)} &= \hat{P}_{(\phi_X)}(p) \cdot E \\
 &= \left(r_1(1) + r_2 \left\{ \cos\left(\frac{2\pi}{3}\right) + i \sin\left(\frac{2\pi}{3}\right) \right\} + r_3 \left\{ \cos\left(\frac{2\pi}{3}\right) - i \sin\left(\frac{2\pi}{3}\right) \right\} \right) \\
 &\quad \pm \left(r_1(1) + r_2 \left\{ \cos\left(\frac{2\pi}{3}\right) - i \sin\left(\frac{2\pi}{3}\right) \right\} + r_3 \left\{ \cos\left(\frac{2\pi}{3}\right) + i \sin\left(\frac{2\pi}{3}\right) \right\} \right) \\
 \varphi_{E_{rad}(+)} &\simeq 2r_1 - r_2 - r_3 \\
 \varphi_{E_{rad}(-)} &= i\sqrt{3}r_2 - i\sqrt{3}r_3 \simeq r_2 - r_3
 \end{aligned} \tag{.1.2}$$

Application of the projection operator of the tangential function onto A

$$\begin{aligned}
 \varphi_{A_{tan}} &= \hat{P}_{(\phi_L)}(t) \cdot A \\
 &= t_1(1) + t_2(1) + t_3(1) \\
 \varphi_{A_{tan}} &\simeq t_1 + t_2 + t_3
 \end{aligned} \tag{.1.3}$$

Application of the projection operator of the tangential function onto E

$$\begin{aligned}
 \varphi_{E_{tan}(\pm)} &= \hat{P}_{(\phi_L)}(t) \cdot E \\
 &= \left(t_1(1) + t_2 \left\{ \cos\left(\frac{2\pi}{3}\right) + i \sin\left(\frac{2\pi}{3}\right) \right\} + t_3 \left\{ \cos\left(\frac{2\pi}{3}\right) - i \sin\left(\frac{2\pi}{3}\right) \right\} \right) \\
 &\quad \pm \left(t_1(1) + t_2 \left\{ \cos\left(\frac{2\pi}{3}\right) - i \sin\left(\frac{2\pi}{3}\right) \right\} + t_3 \left\{ \cos\left(\frac{2\pi}{3}\right) + i \sin\left(\frac{2\pi}{3}\right) \right\} \right) \\
 \varphi_{E_{tan}(+)} &\simeq 2t_1 - t_2 - t_3 \\
 \varphi_{E_{tan}(-)} &= i\sqrt{3}t_2 - i\sqrt{3}t_3 \simeq t_2 - t_3
 \end{aligned} \tag{.1.4}$$

.2 Normalization of SALCs

Normalization of (5.2.1)

$$\begin{aligned}
 \varphi_{A_{rad}} &\simeq r_1 + r_2 + r_3 \\
 N_{A_{rad}}^2 (\varphi_{A_{rad}})^2 &= 1 \\
 N_{A_{rad}}^2 (r_1 + r_2 + r_3)(r_1 + r_2 + r_3) &= 1 \\
 N_{A_{rad}}^2 (r_1^2 + r_2^2 + r_3^2 + 2r_1r_2 + 2r_1r_3 + 2r_2r_3) &= 1 \\
 N_{A_{rad}}^2 (1 + 1 + 1 + 2(0) + 2(0) + 2(0)) &= 1 \\
 3N_{A_{rad}}^2 &= 1 \\
 N_{A_{rad}} &= \frac{\sqrt{3}}{3} \\
 \varphi_{A_{rad}} &= \frac{\sqrt{3}}{3} (r_1 + r_2 + r_3)
 \end{aligned} \tag{.2.1}$$

Normalization of (5.2.3)

$$\begin{aligned}
\varphi_{E_{rad}(+)} &\simeq 2r_1 - r_2 - r_3 \\
N_{E_{rad}(+)}^2 (\varphi_{E_{rad}(+)})^2 &= 1 \\
N_{E_{rad}(+)}^2 (2r_1 - r_2 - r_3)(2r_1 - r_2 - r_3) &= 1 \\
N_{E_{rad}(+)}^2 (4r_1^2 + r_2^2 + r_3^2 - 4r_1r_2 - 4r_1r_3 + 2r_2r_3) &= 1 \\
N_{E_{rad}(+)}^2 (4 + 1 + 1 - 4(0) - 4(0) + 2(0)) &= 1 \\
6N_{E_{rad}(+)}^2 &= 1 \\
N_{E_{rad}(+)} &= \frac{\sqrt{6}}{6} \\
\varphi_{E_{rad}(+)} &= \frac{\sqrt{6}}{6} (2r_1 - r_2 - r_3)
\end{aligned} \tag{.2.2}$$

$$\begin{aligned}
\varphi_{E_{rad}(-)} &\simeq r_2 - r_3 \\
N_{E_{rad}(-)}^2 (\varphi_{E_{rad}(-)})^2 &= 1 \\
N_{E_{rad}(-)}^2 (r_2 - r_3)(r_2 - r_3) &= 1 \\
N_{E_{rad}(-)}^2 (r_2^2 + r_3^2 - 2r_2r_3) &= 1 \\
N_{E_{rad}(-)}^2 (1 + 1 - 2(0)) &= 1 \\
2N_{E_{rad}(-)}^2 &= 1 \\
N_{E_{rad}(-)} &= \frac{\sqrt{2}}{2} \\
\varphi_{E_{rad}(-)} &= \frac{\sqrt{2}}{2} (r_2 - r_3)
\end{aligned} \tag{.2.3}$$

Normalization of (.1)

$$\begin{aligned}
\varphi_{A_{tan}} &\simeq t_1 + t_2 + t_3 \\
N_{A_{tan}}^2 (\varphi_{A_{tan}})^2 &= 1 \\
N_{A_{tan}}^2 (t_1 + t_2 + t_3)(t_1 + t_2 + t_3) &= 1 \\
N_{A_{tan}}^2 (t_1^2 + t_2^2 + t_3^2 + 2t_1t_2 + 2t_1t_3 + 2t_2t_3) &= 1 \\
N_{A_{tan}}^2 (1 + 1 + 1 + 2(0) + 2(0) + 2(0)) &= 1 \\
3N_{A_{tan}}^2 &= 1 \\
N_{A_{tan}} &= \frac{\sqrt{3}}{3} \\
\varphi_{A_{rad}} &= \frac{\sqrt{3}}{3} (t_1 + t_2 + t_3)
\end{aligned} \tag{.2.4}$$

Normalization of (.1)

$$\begin{aligned}
\varphi_{E_{tan(+)}} &\simeq 2t_1 - t_2 - t_3 \\
N_{E_{tan(+)}}^2 (\varphi_{E_{tan(+)}})^2 &= 1 \\
N_{E_{tan(+)}}^2 (2t_1 - t_2 - t_3)(2t_1 - t_2 - t_3) &= 1 \\
N_{E_{tan(+)}}^2 (4t_1^2 + t_2^2 + t_3^2 - 4t_1t_2 - 4t_1t_3 + 2t_2t_3) &= 1 \\
N_{E_{tan(+)}}^2 (4 + 1 + 1 - 4(0) - 4(0) + 2(0)) &= 1 \\
6N_{E_{tan(+)}}^2 &= 1 \\
N_{E_{tan(+)}} &= \frac{\sqrt{6}}{6} \\
\varphi_{E_{tan(+)}} &= \frac{\sqrt{6}}{6} (2t_1 - t_2 - t_3)
\end{aligned} \tag{.2.5}$$

$$\begin{aligned}
\varphi_{E_{tan}(-)} &\simeq t_2 - t_3 \\
N_{E_{tan}(-)}^2 (\varphi_{E_{rad}(-)})^2 &= 1 \\
N_{E_{tan}(-)}^2 (t_2 - t_3)(t_2 - t_3) &= 1 \\
N_{E_{tan}(-)}^2 (t_2^2 + t_3^2 - 2t_2t_3) &= 1 \\
N_{E_{tan}(-)}^2 (1 + 1 - 2(0)) &= 1 \\
2N_{E_{tan}(-)}^2 &= 1 \\
N_{E_{tan}(-)} &= \frac{\sqrt{2}}{2} \\
\varphi_{E_{tan}(-)} &= \frac{\sqrt{2}}{2} (t_2 - t_3)
\end{aligned} \tag{.2.6}$$

.3 Normalization of molecular wave functions

For the inclusion of ligand set $\varphi_{A_{rad}}$

$$\begin{aligned}
N_{mol,A}^2 \psi_{mol,A}^2 &= N^2 \left(\frac{\sqrt{3}}{3} r_1 + \frac{\sqrt{3}}{3} r_2 + \frac{\sqrt{3}}{3} r_3 + \phi_M \right)^2 = 1 \\
N_{mol,A}^2 \left(\frac{1}{3} + \frac{1}{3} + \frac{1}{3} + 1 \right) &= 1 \\
2N_{mol,A}^2 &= 1 \\
N_{mol,A} &= \frac{\sqrt{2}}{2}
\end{aligned} \tag{.3.1}$$

$$\begin{aligned}
\Psi_{mol,A} &= \frac{\sqrt{2}}{2} \left(\frac{\sqrt{3}}{3} r_1 + \frac{\sqrt{3}}{3} r_2 + \frac{\sqrt{3}}{3} r_3 + \phi_M \right) \\
\Psi_{mol,A} &= \frac{\sqrt{6}}{6} r_1 + \frac{\sqrt{6}}{6} r_2 + \frac{\sqrt{6}}{6} r_3 + \frac{\sqrt{2}}{2} \phi_M
\end{aligned} \tag{.3.2}$$

For the inclusion of ligand set $\varphi_{E_{rad}(+)}$

$$\begin{aligned}
 N_{mol,E(+)}^2 \psi_{mol,E}^2 &= N^2 \left(\frac{\sqrt{6}}{3} r_1 - \frac{\sqrt{6}}{3} r_2 - \frac{\sqrt{6}}{3} r_3 + \phi_M \right)^2 = 1 \\
 N_{mol,E(+)}^2 \left(\frac{2}{3} + \frac{1}{6} + \frac{1}{6} + 1 \right) &= 1 \\
 2N_{mol,E(+)}^2 &= 1 \\
 N_{mol,E(+)} &= \frac{\sqrt{2}}{2}
 \end{aligned} \tag{.3.3}$$

$$\begin{aligned}
 \Psi_{mol,E(+)} &= \frac{\sqrt{2}}{2} \left(\frac{\sqrt{6}}{3} r_1 - \frac{\sqrt{6}}{6} r_2 - \frac{\sqrt{6}}{6} r_3 + \phi_M \right) \\
 \Psi_{mol,E(+)} &= \frac{\sqrt{3}}{3} r_1 - \frac{\sqrt{3}}{6} r_2 - \frac{\sqrt{3}}{6} r_3 + \frac{\sqrt{2}}{2} \phi_M
 \end{aligned} \tag{.3.4}$$

For the inclusion of ligand set $\varphi_{E_{rad}(-)}$

$$\begin{aligned}
 N_{mol,E(-)}^2 \psi_{mol,E'}^2 &= N^2 \left(\frac{\sqrt{2}}{2} r_2 - \frac{\sqrt{2}}{2} r_3 + \phi_M \right)^2 = 1 \\
 N_{mol,E(-)}^2 \left(\frac{1}{2} + \frac{1}{2} + 1 \right) &= 1 \\
 2N_{mol,E(-)}^2 &= 1 \\
 N_{mol,E(-)} &= \frac{\sqrt{2}}{2}
 \end{aligned} \tag{.3.5}$$

$$\begin{aligned}
 \Psi_{mol,E(-)} &= \frac{\sqrt{2}}{2} \left(\frac{\sqrt{2}}{2} r_2 - \frac{\sqrt{2}}{2} r_3 + \phi_M \right) \\
 \Psi_{mol,E(-)} &= \frac{1}{2} r_2 - \frac{1}{2} r_3 + \frac{\sqrt{2}}{2} \phi_M
 \end{aligned} \tag{.3.6}$$

.4 Normalization including ligand-ligand overlap

For the new ligand set $\sigma_r(a)$ where $\sigma_r(a) = N_{S(r,r)} \varphi_{A_{rad}}$

$$\begin{aligned}
1 &= N_{S(r,r)}^2 \frac{1}{3} \int (r_1 + r_2 + r_3) (r_1 + r_2 + r_3) d\tau \\
1 &= N_{S(r,r)}^2 \frac{1}{3} \int (r_1^2 + r_2^2 + r_3^2 + 2r_1r_2 + 2r_1r_3 + 2r_2r_3) d\tau \\
1 &= N_{S(r,r)}^2 \frac{1}{3} [3 + 6S(r, r)] = N_{S(r,r)}^2 [1 + 2S(r, r)] \\
\sigma_r(a) &= \frac{\sqrt{3}(r_1 + r_2 + r_3)}{3[1 + 2S(r, r)]^{1/2}}
\end{aligned} \tag{.4.1}$$

For the new ligand set $\sigma_r(e_{(+)})$ where $\sigma_r(e_{(+)}) = N_{S(r,r)} \varphi_{E_{rad}(+)}$

$$\begin{aligned}
1 &= N_{S(r,r)}^2 \frac{1}{6} \int (2r_1 - r_2 - r_3) (2r_1 - r_2 - r_3) d\tau \\
1 &= N_{S(r,r)}^2 \frac{1}{6} \int (4r_1^2 + r_2^2 + r_3^2 - 4r_1r_2 - 4r_1r_3 + 2r_2r_3) d\tau \\
1 &= N_{S(r,r)}^2 \frac{1}{6} [6 - 6S(r, r)] = N_{S(r,r)}^2 [1 - S(r, r)] \\
\sigma_r(e_{(+)}) &= \frac{\sqrt{6}(2r_1 - r_2 - r_3)}{6[1 - S(r, r)]^{1/2}}
\end{aligned} \tag{.4.2}$$

For the new ligand set $\sigma_r(e_{(-)})$ where $\sigma_r(e_{(-)}) = N_{S(r,r)} \varphi_{E_{rad}(-)}$

$$\begin{aligned}
1 &= N_{S(r,r)}^2 \frac{1}{2} \int (r_2 - r_3) (r_2 - r_3) d\tau \\
1 &= N_{S(r,r)}^2 \frac{1}{2} \int (r_2^2 + r_3^2 + 2r_2r_3) d\tau \\
1 &= N_{S(r,r)}^2 \frac{1}{2} [2 - 2S(r, r)] = N_{S(r,r)}^2 [1 - S(r, r)] \\
\sigma_r(e_{(-)}) &= \frac{\sqrt{2}(r_2 - r_3)}{2[1 - S(r, r)]^{1/2}}
\end{aligned} \tag{.4.3}$$

.5 Group overlap of metal and ligand orbitals

$$G = \int \Phi_M \sigma_{ligand} d\tau \tag{.5.1}$$

For ligand set $\sigma_r (a)$

$$\begin{aligned}
 G_A (d_{z^2}, \sigma_r) &= \int d_{z^2} \left(\frac{\sqrt{3}(r_1 + r_2 + r_3)}{3[1 + 2S(r, r)]^{1/2}} \right) d\tau \\
 G_A (d_{z^2}, \sigma_r) &= \frac{\sqrt{3}}{3[1 + 2S(r, r)]^{1/2}} [S(d_{z^2}, r_1) + S(d_{z^2}, r_2) + S(d_{z^2}, r_3)] \\
 G_A (d_{z^2}, \sigma_r) &= \frac{\sqrt{3}[S(d_{z^2}, r)]}{[1 + 2S(r, r)]^{1/2}}
 \end{aligned} \tag{.5.2}$$

For ligand set $\sigma_r (e_{(+)})$

$$\begin{aligned}
 G_{E_{(+)}} (d_{(xz/yz), (x^2-y^2/xy)}, \sigma_r) &= \int d_{(xz/yz), (x^2-y^2/xy)} \left(\frac{\sqrt{6}(2r_1 - r_2 - r_3)}{6[1 - S(r, r)]^{1/2}} \right) d\tau \\
 G_{E_{(+)}} (d_{(xz/yz), (x^2-y^2/xy)}, \sigma_r) &= \frac{\sqrt{6}}{6[1 + 2S(r, r)]^{1/2}} [2S(d_{(xz/yz), (x^2-y^2/xy)}, r_1) \\
 &\quad - S(d_{(xz/yz), (x^2-y^2/xy)}, r_2) \\
 &\quad - S(d_{(xz/yz), (x^2-y^2/xy)}, r_3)] \\
 G_{E_{(+)}} (d_{(xz/yz), (x^2-y^2/xy)}, \sigma_r) &= \frac{2\sqrt{6}[S(d_{(xz/yz), (x^2-y^2/xy)}, r)]}{3[1 - S(r, r)]^{1/2}}
 \end{aligned} \tag{.5.3}$$

For ligand set $\sigma_r (e_{(-)})$

$$\begin{aligned}
 G_{E_{(-)}} (d_{(xz/yz), (x^2-y^2/xy)}, \sigma_r) &= \int d_{(xz/yz), (x^2-y^2/xy)} \left(\frac{\sqrt{2}(r_2 - r_3)}{2[1 - S(r, r)]^{1/2}} \right) d\tau \\
 G_{E_{(-)}} (d_{(xz/yz), (x^2-y^2/xy)}, \sigma_r) &= \frac{\sqrt{2}}{2[1 + 2S(r, r)]^{1/2}} [S(d_{(xz/yz), (x^2-y^2/xy)}, r_2) \\
 &\quad - S(d_{(xz/yz), (x^2-y^2/xy)}, r_3)] \\
 G_{E_{(-)}} (d_{(xz/yz), (x^2-y^2/xy)}, \sigma_r) &= \frac{2[S(d_{(xz/yz), (x^2-y^2/xy)}, r)]}{[1 - S(r, r)]^{1/2}}
 \end{aligned} \tag{.5.4}$$